

Contents — H through K

Reconciling the MOLA, TES, and Neutron Observations of the North Polar CO ₂ Mass Budget on Mars <i>R. M. Haberle, B. Mattingly, and T. N. Titus</i>	8035
Obliquity Driven Climate Change in Mars' Recent Past <i>R. M. Haberle, F. Montmessin, F. Forget, A. Spiga, and A. Colaprete</i>	8060
Albedo Variation on the Martian Northern Polar Cap as Seen by MGS <i>A. S. Hale, D. S. Bass, and L. K. Tamppari</i>	8066
Detection and Localization of Mars Sub-Surface Ice by Surface Impedance Measurements from a Rover as Part of the WISDOM/PASTEUR and Other Rover Experiments <i>M. Hamelin, R. Grard, J.-J. Berthelier, R. Ney, R. Trautner, and F. Simoes</i>	8006
Evolution of Low-Emissivity Spots in the Martian Winter Polar Caps: Mobility of Dust Grains <i>G. B. Hansen</i>	8103
Upper Latitude Ice Flow, Gullies, and Long-Term Glacial History <i>W. K. Hartmann</i>	8110
Extensive Hesperian-aged South Circumpolar Ice Sheet on Mars: Dorsa Argentea Formation Synthesis <i>J. W. Head, G. J. Ghatan, and D. Marchant</i>	8067
Tropical Mountain Glaciers on Mars: Evidence for Amazonian Climate Change <i>J. W. Head, D. E. Shean, S. Milkovich, and D. Marchant</i>	8105
Speculations on Orbital Forcing of Sublimation from the Polar Caps <i>M. H. Hecht</i>	8092
CryoScout: A Descent Through the Mars Polar Cap <i>M. H. Hecht and R. S. Saunders</i>	8078
Stratigraphy and Structure of the South Polar Layered Deposits on Mars <i>K. E. Herkenhoff, L. A. Soderblom, and R. L. Kirk</i>	8030
The Mars Imager for Cloud and Aerosol (MICA) <i>V. J. Hipkin, J. R. Drummond, J. Hackett, R. Deschambault, J. Abbatt, G. Besla, C. T. McElroy, S. M. L. Melo, K. Strong, J. J. Caldwell, J. C. McConnell, D. V. Michelangeli, P. Bernath, J. Sloan, W. Ward, and B. Tolton</i>	8109
Accuracy of Mars' Polar Axis Determination by Earth-based RSDI <i>I. V. Holin</i>	8051
Echo Source Discrimination in Airborne Radar Sounding Data for Mars Analog Studies, Dry Valleys, Antarctica <i>J. W. Holt, D. D. Blankenship, M. E. Peters, S. D. Kempf, D. L. Morse, and B. J. Williams</i>	8104
Modeling Martian Fog Formation in the Northern High Latitudes During the Retreat of the Seasonal North Polar Cap <i>A. Inada, M. I. Richardson, and A. D. Toigo</i>	8077

Analysis of Properties of the North and South Polar Layered Deposits <i>A. B. Ivanov, S. Byrne, M. I. Richardson, A. R. Vasavada, T. N. Titus, J. F. Bell, T. H. McConnochie, P. R. Christensen, and THEMIS Science Team</i>	8084
Prospecting for Martian Ice from Orbit <i>L. C. Kanner, M. S. Bell, and C. C. Allen</i>	8113
ASTER Imagery and Interpretation of Glaciers in Jasper National Park and Elsewhere in the Cordillera <i>J. S. Kargel and B. Molnia</i>	8127
Martian Polar Ice Sheets and Mid-Latitude Debris-rich Glaciers, and Terrestrial Analogs <i>J. S. Kargel, B. Molnia, and K. L. Tanaka</i>	8112
Recent Detection of Winter Polar Warming in the Mars Upper Atmosphere <i>G. M. Keating, M. E. Theriot Jr., R. H. Tolson, S. W. Bougher, F. Forget, M. Angelats i Coll, and J. M. Forbes</i>	8033
Behavior of Solid CO ₂ on Mars: Still a Zoo <i>H. H. Kieffer</i>	8083
Detailed Geologic Analysis of Part of the South Polar Layered Deposits, Planum Australe, Mars <i>E. J. Kolb and K. L. Tanaka</i>	8116
Intercrystalline Swelling of Stratified Silicates Exposed to Negative Temperatures <i>I. A. Komarov</i>	8015
Properties of Disperse Frost Rock in the Range of Low Negative Temperatures <i>I. A. Komarov and V. S. Issaev</i>	8016
Seasonal Melting of Surface Water Ice Condensing in Martian Gullies <i>K. J. Kossacki and W. J. Markiewicz</i>	8031
Surface Features of the South Polar Layered Deposits of Mars and Possible Terrestrial Analogues <i>M. R. Koutnik, S. Byrne, and B. C. Murray</i>	8074
Polar Wander in the Geological History of Mars: Constraints from Topography Statistics <i>M. A. Kreslavsky and J. W. Head</i>	8085
Determining Structural and Mechanical Properties of Snow with a High-Resolution Penetrometer <i>K. Kronholm, J. B. Johnson, and M. Schneebeli</i>	8048
Preliminary Characterization of a Microbial Community of Rock Varnish from Death Valley, California <i>K. R. Kuhlman, M. T. La Duc, G. M. Kuhlman, R. C. Anderson, D. A. Newcombe, W. Fusco, T. Steucker, L. Allenbach, C. Ball, and R. L. Crawford</i>	8057

RECONCILING THE MOLA, TES, AND NEUTRON OBSERVATIONS OF THE NORTH POLAR CO₂ MASS BUDGET ON MARS. R.M. Haberle¹, B. Mattingly², and T.N. Titus³. ¹Space Science Division, MS 245-3, NASA/Ames Research Center, Moffett Field CA, 94035, Robert.M.Haberle@nasa.gov. ²Dept. Meteorology, San Jose State University, San Jose CA, 95192, bridgemat@yahoo.com. ³U.S. Geological Survey, 2255 North Gemini Drive, Flagstaff AZ, 86001, ttitus@usgs.gov.

Introduction: There are now three independent observations of the CO₂ polar cap mass budget of Mars' north polar cap. The first is based elevation changes detected by the Mars Orbiter Laser Altimeter (MOLA) on the Mars Global Surveyor (MGS) [1]. The second is based on MGS Thermal Emission Spectrometer (TES) broadband observations of the solar and infrared radiation fields at the top of the atmosphere [2,3]. The third is based on neutron counts measured by the neutron spectrometer (NS) on Odyssey [4]. If one assumes a cap density of 910 kg/m³ [1], then the peak mass loading poleward of 85°N inferred from the MOLA data is ~1090 kg/m², which compares to ~1150 kg/m² inferred from TES for the same region, and ~700 kg/m² from the NS data. TES and MOLA are in good agreement, but are about 60% higher than the NS data. Is there a way to reconcile these discrepancies?

Role of surface heat storage: The TES data are based on an energy balance. The net radiative loss (gain) in a column is balanced by latent heating due condensation (sublimation) of CO₂. In calculating the mass budget, the other main energy sources, atmospheric heat transport and subsurface conduction, were neglected [2,3]. At the pole, atmospheric heat transport is indeed a small term. However, subsurface heat conduction can be significant because at the North Pole water ice, which has a high thermal conductivity compared to bare soil, is a dominant component of the subsurface. Thus, heat conducted down into the ice during summer will slowly bleed back out during fall and winter reducing the amount of CO₂ that condenses on the pole.

We have taken a first cut at quantifying this effect by fitting a curve to Paige's [5] estimates of the conducted energy flux in his analysis of Viking IRTM data. For a thermal inertia of ~2100 (SI units) this curve shows a peak upward conducted heat flux of about 30 W/m² at L_s=180°, which is just after the time CO₂ begins condensing. This then gradually tapers off to less than several W/m² near the end of spring just before the CO₂ ice completely sublimates. We then added this term to the TES radiation fields and recalculated the CO₂ mass budget. We find that subsurface heat conduction at the North Pole can reduce the amount of CO₂ that condenses by about 400 kg/m²,

which brings the TES data in close agreement with the NS data.

CO₂ ice density: That leaves the MOLA data much higher than both TES and NS. However, the MOLA data are based on elevation changes and are not direct measurements of the mass loading. To relate the elevation changes to a mass loading requires knowledge of the ice density. The MOLA data can be reconciled with TES and NS if the CO₂ ice density is ~600 kg/m³. Feldman et al. [4] suggested that low ice densities could be a way to explain the difference between MOLA and NS.

The MOLA combined gravity/elevation measurements infer a mean cap density of 910 ± 230 kg/m² [1]. Thus, 600 kg/m³ is below the lower limit of the MOLA measurements. However, the MOLA-derived density is an average for the entire seasonal cap. It is possible that the density of the north polar deposits is less than the average of the entire seasonal cap. A good physical basis for this is the much more frequent occurrence of "cold spots" at the North Pole compared to lower latitudes [6]. Snowfall is a strong candidate for the origin of these cold spots. If true, it means that a much greater fraction of the north polar deposits originate from the atmosphere as snowfall rather than direct condensation onto the surface. Surface accumulations resulting from snowfall have lower densities than those originating from direct deposition.

Conclusion: Of the three measurements that bear on the north polar CO₂ mass budget, the NS provides the most direct measurement of the mass loading. Yet it shows much less CO₂ accumulating on the pole than initially predicted by either MOLA or TES. These differences can be reconciled by (a) including subsurface heat conduction in the TES calculations, and (b) using a lower ice density to convert MOLA elevation data to a mass loading.

References: [1] Smith D.E., Zuber M.T. and Neumann G.A. (2001) *Science*, 294, 2141-2148. [2] Kieffer, H.H. and Titus, T.N. (2001) *Icarus*, 154, 162-180. [3] Titus, T.N. (2003) *International workshop: Mars atmosphere modelling and observations*, Granada, Spain. [4] Feldman W.C., et al. (2003) *JGR*, submitted. [5] Paige, D.A. (1985) *Ph.D. Thesis*, UCLA, 206p. [6] Titus T.N. and Kieffer, H.H. (2003) *6th International Mars Conference*, Pasadena Ca.

OBLIQUITY DRIVEN CLIMATE CHANGE IN MARS' RECENT PAST. R.M. Haberle¹, F. Montmessin¹, F. Forget², A. Spiga³, and A. Colaprete⁴. ¹Space Science Division, MS 245-3, NASA/Ames Research Center, Moffett Field CA, 94035, Robert.M.Haberle@nasa.gov. ²Laboratoire de Météorologie Dynamique, Université Paris, 4 pl. Jussieu, 75252 Paris Cedex 05-FRANCE, forget@lmd.jussieu.fr. ³Ecole Polytechnique, 91128 Palaiseau, Cedex FRANCE, Aymeric.Spiga@polytechnique.org. ⁴SETI Institute, Space Science Division, MS 245-3, NASA/Ames Research Center, Moffett Field CA, 94035, tonyc@freeze.arc.nasa.gov.

Introduction: To explain the equatorial valley networks on Mars, Jakosky and Carr [1] suggested that water ice now stored in the north polar region would be mobilized at high obliquity and precipitate out at low latitudes. Extrapolating the present day latitudinal distribution of water vapor to high obliquity conditions, and noting that the low latitude atmosphere would be saturated, they predicted substantial surface ice deposits would accumulate in the tropics at such times.

The first general circulation model simulations to verify this prediction were reported by Haberle et al. [2] who found that while ice can accumulate at low latitudes at high obliquity, it is distributed regionally depending on orbital conditions. Forget [3], Richardson and Wilson [4], and Mischna et al. [5], subsequently obtained similar results with independent models. Thus, obliquity driven climate change may help explain the many tropical landforms thought to be sculpted by water in one form or another (see, for example, refs [6], [7], and [8]).

While low latitude ice accumulations at high obliquity appears to be a robust result, the major challenge now facing models is predicting ice accumulations in the same places where the geological evidence suggests it occurred. This will depend not only on orbital conditions, but also on what physical processes the models include in the hydrological cycle. For example, none of the models mentioned above include the radiative effects of water vapor or clouds, yet both are expected to be in abundance at high obliquity. And none of the models has a very realistic cloud microphysics scheme, which can have a significant effect on how clouds affect the planet's radiation balance.

Here we extend these early modeling results by including a more sophisticated cloud microphysics package, as well as the radiative effects of water vapor and clouds.

Model description: We use the NASA/Ames C-grid Mars general circulation model with an updated radiation code and cloud microphysics scheme. To speed up the simulations, we run the model at fairly coarse resolution (7.5° latitude x 22.5° longitude). Future efforts will examine the effect of resolution on the results.

Radiation Code Fluxes and heating rates are calculated from a radiation code based on the two-stream solution to radiative transfer that fully accounts for multiple scattering in the presence of gaseous absorption. The model has 12 spectral intervals. Dust and water ice scattering properties are included. For dust, we use the Ockert-Bell [9] values in the visible, and Forget [10] values in the infrared. For ice, we can either compute them online as the cloud evolves, or we can specify them. Gaseous opacities for water vapor and CO₂ are calculated from correlated k-distributions taken from full line-by-line models.

Cloud Microphysics Our cloud scheme is based on a moment/order scheme in which the mass mixing ratio and number density of the cloud ensemble are the advected species. From these we obtain a mean particle size and an estimate of the particle size distribution (assuming a variance) which we then divide into 8 bins. Cloud microphysics is performed in each of these bins and includes nucleation, condensation, and gravitational settling. Dust is treated as a tracer and serves as condensation nuclei. The altered size distribution is then converted back into a mean size, a mixing ratio, and a particle number density.

Results: We have conducted simulations for a variety of different obliquities, all at present solar luminosity. In each case the model is spun up from dry initial conditions with a residual ice cap at the north pole. After several years, depending on obliquity, the atmosphere equilibrates and repeats from year-to-year. A sample result for the 60° obliquity simulation, without the radiative effects of clouds or water vapor, is shown in Fig. 1. The top panel in Fig. 1 is the zonally averaged column water vapor as a function of time for 7 Mars years. The middle and bottom panels are similar, but for cloud mass and surface ice, respectively.

Water ice subliming from the north residual cap during summer is rapidly transported southward. Clouds form in low northern latitudes and ice precipitates to the surface. The remainder is transported into the southern hemisphere and condenses onto the south seasonal CO₂ ice cap which extends almost to the equator at the solstice. When the south cap retreats, water is released into the atmosphere where some precipitates back to the surface and the remainder is transported north. Again clouds form in the low latitudes

and ice precipitates to the surface. At equilibrium, thousands of precipitable microns of water vapor appear in the summer polar regions. There is more water in the south than the north because the south cap is a better trap for water, and because the Southern Hemisphere is warmer during summer than in the north. Cloud abundances also reach the thousand precipitable micron mark with model predicted particle sizes in the 20-30 micron range. These particles are much bigger, and subsequently fall out faster, than those for present obliquity.

Eventually, permanent deposits form (i.e., ice remains on the ground all year long) in the low latitudes of each hemisphere. These deposits are concentrated along the northern flanks of the Tharsis region and to the northeast of the Hellas basin. Topography plays a key role on where the deposits form through its influence on the circulation. The deposits do not necessarily form in locations where the mean annual surface temperatures are a minimum. They form where the saturation state of the atmosphere is highest. This, in turn, is influenced not only by the thermal structure of the atmosphere, but also by the transport characteristics of the atmosphere.

Simulations which include the radiative effects of water vapor show similar results, but with (a) an increase in the amount of surface ice, (b) a slight shift in the location of the deposits, (c) a cooler and cloudier atmosphere, and (d) slightly warmer surface temperatures. We are presently undertaking simulations with the radiative effects of clouds included and will report the results at the meeting. However, off line 1-D simulations using the predicted cloud abundances indicate they will have a much greater influence on the results than water vapor alone. Their abundances (~ 1000 pr- μm), particle sizes (20-30 μm), widespread occurrence, and impact on the solar and infrared radiation fluxes give clouds a much greater role in determining the climate at high obliquity than for present day conditions.

Conclusions: Mars has a natural mechanism for experiencing significant climate change and redistributing surface ice. Obliquity changes alone are quite capable of moving ice into low latitudes and may provide an explanation for the many geological landforms that strongly indicate recent climate change.

References: [1] Jakosky, B.M. and Carr, H.H. (1985) *Nature*, 315, 559-561. [2] Haberle, R.M., et al. (2000) *LPS XXXI*, Abstract #1509. [3] F. Forget (2001), personal communication. [4] Richardson, M.I., and Wilson R.J., *JGR*, 107, 5031-5049. [5] Mischna, et al. (2003) *JGR*, In press. [6] Cabrol, N.A. and Grin, E.A. (2001). *Icarus*, 149, 291-328. [7] Kargel, J. (2001) DPS Abstract # 48.12. [8] Head, J.W. and Mar-

chant, D.R. (2003) 6th International Mars Conference, Abstract #3807. [9] Ockert-Bell, M.E. et al. (1997). *JGR*, 102, 9039-9050. [10] Forget, F. (1998). *GRL*, 25, 1105-1108.

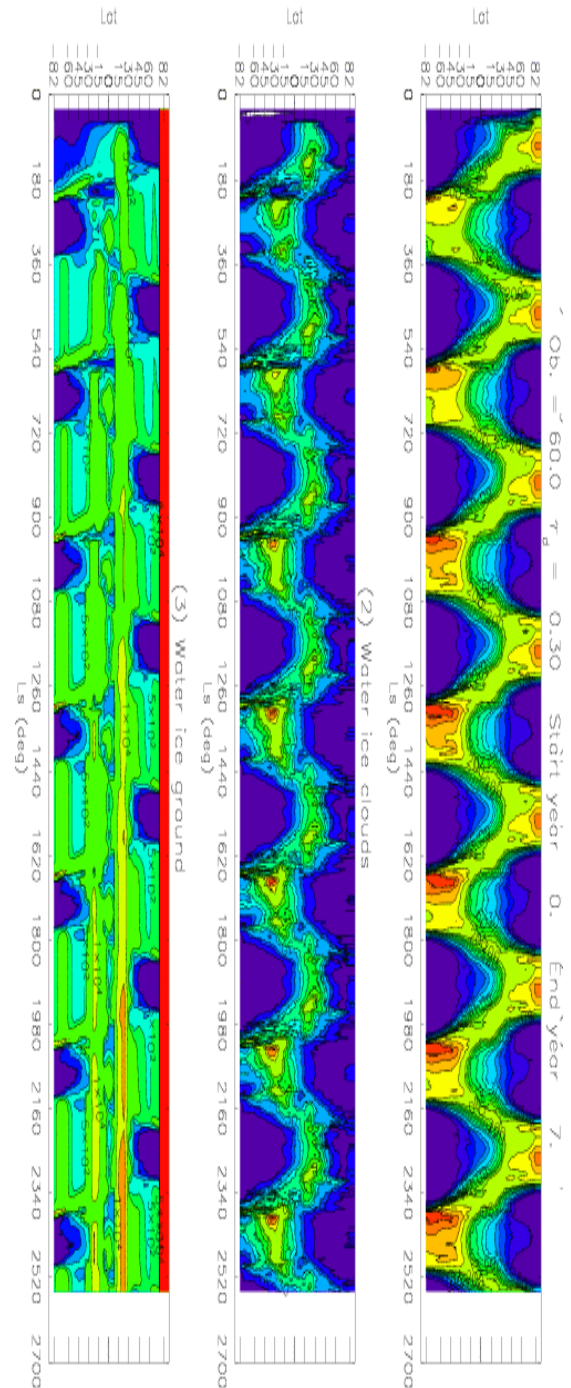


Figure 1

ALBEDO VARIATIONS ON THE MARTIAN NORTHERN POLAR CAP AS SEEN BY MGS. A.S. Hale D. S. Bass, and L. K. Tamppari³, ¹NASA Jet Propulsion Laboratory (MS 264-235, 4800 Oak Grove Drive, Pasadena, CA 91109 amy.s.hale@jpl.nasa.gov), ²NASA Jet Propulsion Laboratory (MS T1722, 4800 Oak Grove Drive, Pasadena, CA 91109 deborah.s.bass@jpl.nasa.gov), ³NASA Jet Propulsion Laboratory (MS 301-422, 4800 Oak Grove Drive, Pasadena, CA 91109 leslie.k.tamppari@jpl.nasa.gov)¹

Introduction The Viking Orbiters determined that the surface of Mars' northern residual cap is water ice. Many researchers have related observed atmospheric water vapor abundances to seasonal exchange between reservoirs such as the polar caps, but the extent to which the exchange between the surface and the atmosphere remains uncertain. Early studies of the ice coverage and albedo of the northern residual Martian polar cap using Mariner 9 and Viking images reported that there were substantial internannual differences in ice deposition on the polar cap [1], a result that suggested a highly variable Martian climate. However, some of the data used in these studies were obtained at differing values of heliocentric solar longitude (L_s). Reevaluation of this dataset in [2] indicated that the residual cap undergoes seasonal brightening throughout the summer, and indicated that this process repeats from year to year. In this study we continue this work with data acquired with Mars Global Surveyor's Mars Orbiter Camera (MOC) and Thermal Emission Spectrometer (TES) instruments.

We use MOC Wide Angel (WA) red filter images of the cap obtained at different values of L_s and different Martian years, and TES albedo data of the north polar region. Previous work in this study has concentrated on MOC images of the cap edge and frost covered outliers [3]; in this phase we systematically investigate images from the cap center (defined for our purposes to be the area northward of 80 degrees latitude) in order to assess any latitudinal trends in seasonal brightening. We have examined data from both instruments from mapping year 1 and 2, though we have ignored MOC data acquired between September 2000 and May 2001, as the MOC camera experienced a state change between those dates that make albedo comparisons with data taken at other times problematic (Cantor, private communication).

Result 1: MOC: Previous work [3] examined brightening of cap edge areas of approximately 40% throughout the northern summer, with the greatest increase occurring in early summer. This result is in agreement with that obtained by [1] for Viking and Mariner 9 data. The region shown in **Figure 1** shows this brightening [3].

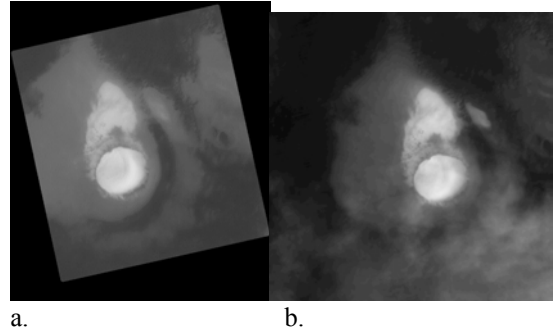


Figure 1: MOC images showing the crater at approx. 77 degrees north and 270 degrees west. The left image (a) shows $L_s = 108$; the image on the right (b) shows $L_s = 161$. An approximate 40% brightening is seen.

In contrast, examination of center cap images to date shows a different trend; center cap images appear to remain at the same albedo as the summer progresses. For example, the region shown in **Figure 2** shows a decrease in brightness of approximately 2.5% between $L_s = 121$ and $L_s = 155$. This change is not within the MOC detectability limits (Malin and Edgett 2001), and so we conclude that this region has experienced no detectable albedo change. This result is in disagreement with that obtained by [1] for Viking and Mariner 9 data that suggested cap edge albedo was controlled by cap center albedo; the reasons for discrepancy are still being explored and will be discussed in our presentation. In all comparisons, the DN values of same pixels of the calibrated processed ISIS level 2 cubes were compared in qview.

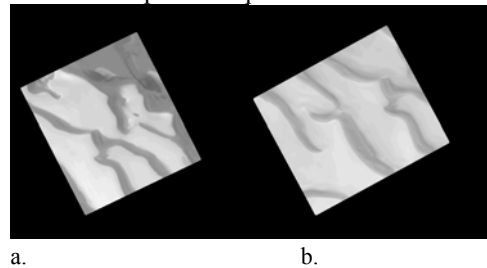


Figure 2: MOC images showing the area at approx. 86 degrees north and 141 degrees west. The left image (a) shows $L_s = 121$, the right one (b) $L_s = 155$. No brightening within reliable detection limits is seen for the same areas

Result 2: TES: The story of north polar water ice frost appears to be even more complex when other datasets are examined. We generated TES lambert albedo maps for the northern polar region; maps were binned in 2 by 2 degrees of latitude and longitude, and 10 degrees of L_s . The spatial resolution of the TES instrument is much less than that of MOC (approximately 3 km per pixel), but larger regional trends can still be seen (**Figure 3**).

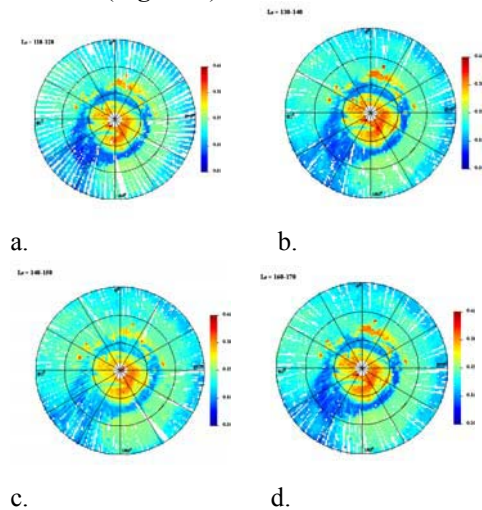


Figure 3: TES lambert albedo data showing the Martian north polar region. The plot on the top left (a) shows L_s 110-120; the plot on the top right (b.) L_s =120-130. The bottom left image (c) shows L_s 140-150, and image d shows L_s = 160-170 The latitude range shown is from 60 to 90 degrees north. All data from second mapping year.

The TES data show a complex picture, with the cap region appearing to brighten early in the summer, then decrease in albedo later in the season, and then brighten again as the summer ends. This is consistent with behavior documented previously [4]. Work is ongoing correlating TES pixels with areas observed by MOC, as is analysis of how the regional view of TES and the localized view of MOC agree and disagree, and we will present the results in our presentation.

Conclusions: The results reported here describe far more complexity in water ice albedo variability than had previously been appreciated. It is clear that the entire cap may not be treated as a monolithic body, but rather, individual locations show a variety of influences. One possibility is that topographic effects may have an effect; water cycle processes may also have a latitudinal dependence. In other research not presented here we are also investigating is the role of atmospheric effects on surface albedo. Clearly, whatever processes are affecting the cap albedo may have latitudinal dependence, and may have important implications for the Martian water cycle. We will present results regarding the full TES albedo data set, as well as other sites observed by MOC. Additionally we will present our interpretation of regional and local process interaction.

References: [1] Bass D. S et al. (2000) *Icarus*, 144, 382-396. [2] Cantor B. et al. (2002) *JGR.*, 107. [3] Hale et al. (2003) 34th LPSC Abstract # 1422. [4] Kieffer and Titus (2001) *Icarus*, 154, 162-180.

DETECTION AND LOCALIZATION OF MARS SUB-SURFACE ICE BY SURFACE IMPEDANCE MEASUREMENTS FROM A ROVER AS PART OF THE WISDOM/PASTEUR AND OTHER ROVER EXPERIMENTS. M. Hamelin¹, R. Grard², J.-J. Berthelier¹, R. Ney¹, R. Trautner² and F. Simoes², ¹CETP-IPSL, 4 avenue de Neptune, 94107, Saint Maur, France, michel.hamelin@cetp.ipsl.fr, ²ESA/RSSD, ESTEC, Postbus 299, NL-2200 AG NOORDWIJK ZH, THE NETHERLANDS, rejean.grard@esa.int.

Introduction: Water and ice on Mars are of great interest for geological, biological and engineering issues. The recent Mars Odyssey missions have shown the presence of water ice in the upper subsurface of Mars in polar regions. At lower latitudes or in particular basins ice should be found at larger depths of several meters. The WISDOM experiment (Water Ice and Subsurface Deposit Observations on Mars) is devoted to the exploration of the subsurface and the search for water and ice in medium latitudes where the subsurface ice could be found at even larger depths. For that purpose it combines a mutual impedance measurement to study the upper layers and a Ground Penetrating Radar that allows reaching larger depths down to a few hundred of meters. In the case of medium-high latitude missions where ice is believed to be at a depth of a few meters, the Mutual and Self Impedance techniques to measure the subsurface permittivity can be used as in the WISDOM project. The instrument is a surface electrode array (7 electrodes) deployed or trailed behind a rover. The multiple combinations between electrodes allow to detect ice embedded in the regolith under an upper layer of dry regolith, and to estimate the depth and ice concentration of the icy layer. It would be possible to follow the ice localization along the track of the rover. That would be very useful information to decide where to drill for a direct access to the ice layer.

Ice identification from permittivity measurements: The Permittivity Probe yields the complex permittivity of the ground over the low frequency range (e.g. 1Hz-10 kHz), by measuring the mutual impedance of two antennas, one operating as a transmitter, and the other one as a receiver. At low frequencies, the rotation of polarized molecules contributes the most significantly to the displacement current. Instruments working in the low frequency domain are therefore well suited to the characterization of the electrical properties of ice mixtures. The dielectric constant of water ice embedded in regolith, at temperatures around 200 K, displays indeed a strong dependence on frequency in the 1-100 Hz range. The Permittivity Probe therefore provides a sensitive measure of the water ice content in the sub-surface.

Subsurface ice detection with multiple electrode arrays: When the electrode array is lying on the surface, far away from the rover, the apparent measured permittivity is the mean of vacuum and ground permittivities. So, a flat system of electrodes is ideal to deduce directly the permittivity from self or mutual impedance measurements. For a single quadrupole, the measurement domain is commensurate with the size of the quadrupole. If the subsurface can be considered as layered horizontally, which is likely the case for subsurface icy layers, a multiple array combining several quadrupole sizes, allows determining the parameters of the layered model, layer permittivities and depths of the interfaces. With the system of 7 electrodes that we propose, it would be possible to estimate at least the characteristics of the upper layer and those of the underlying material where ice is expected. A synthetic model of the subsurface is used for this study.

Instrument design: We discuss the design of the instrument, estimate its main characteristics of size and mass that are relative to the desired depth range of the measurements and we point out the particular points to be addressed in an engineering feasibility study.

EVOLUTION OF LOW-EMISSIVITY SPOTS IN THE MARTIAN WINTER POLAR CAPS: MOBILITY OF DUST GRAINS. G. B. Hansen, Planetary Science Institute, Northwest Division, Department of Earth and Space Science, University of Washington, Seattle, WA 98195 (ghansen@rad.ess.washington.edu).

Introduction: Temporally and spatially variable regions of low 20- μm emissivity occur regularly on the winter polar caps of Mars, as first discovered in Viking orbiter observations [1], and subsequently in spectra returned by the Mars Global Surveyor Thermal Emission Spectrometer (TES) [2, 3, 4]. Although many disparate effects were originally offered to explain these features, the current consensus is that they are caused by regions of relatively fine-grained CO_2 frost, probably the result of snowfall [4, 5], and occurring often in regions of high topographic slopes, implying dynamic atmospheric processes [6]. The dynamic nature of these spots has been demonstrated by repeated TES observations of the same locations [7]. The apparent grain coarsening observed has been explained as a process of “continued condensation” [6] or a sintering process starting from micron-sized grains [7] based on theoretical study by Eluszkiewicz [8]. My mapping of the polar cap composition and properties [9] has suggested another possible process: the movement of dust condensation nuclei from the center of newly fallen snow grains (where they are largely optically hidden) to grain boundaries (where they are fully optically active). This process was suggested by the modeling of low-emissivity spots in which the CO_2 ice grain size is little different from, while the apparent dust content is much smaller than in the surrounding regions.

Observation Details and Calibration: The TES spectra shown here are from revolution 214, in the first science phasing orbit period (SPO-1). It took place in April 1998, with $L_S \approx 304^\circ$, roughly halfway between the winter solstice and the spring equinox. The historical polar cap size is near its maximum extent at this time and extends to $55\text{--}60^\circ\text{N}$. The limit of polar night is at $\sim 69^\circ\text{N}$, and the spacecraft ground track crosses into sunlight at $\sim 67^\circ\text{N}$. The data sequence starts on the night side at 59.5°N in western Utopia Planitia (70°W). The maximum latitude reached over the elevated residual polar cap is 86.2°N . The seasonal polar cap extends to $\sim 51.5^\circ\text{N}$ on the day side, in Tempe Terra (257°W).

The TES is a Michelson interferometer measuring from 1650 to 200 cm^{-1} ($\sim 6\text{--}50\ \mu\text{m}$) with a spectral resolution of either 6 or 12 cm^{-1} , and a two-channel bolometric radiometer measuring solar ($0.3\text{--}2.7\ \mu\text{m}$) and thermal ($5.5\text{--}100\ \mu\text{m}$) spectral regions [2, 10]. The finest spatial resolution of TES measurements is <3 km. Observations of the winter polar regions are useful only above $8\text{--}10\ \mu\text{m}$.

There are many artifacts in the polar spectra from the PDS supplied dataset. These were corrected by adjusting instrument sensitivity and darks. The sensitivity is set assuming that it does not change rapidly with time, and that later times in the sequence are better calibrated. The darks measured by pointing the mirror up differ from those when pointed to the side or down [10]. The offset is a very significant fraction of typical polar spectra [3]. The dark level can be estimated by inspecting limb scan sequences. They are adjusted at the short wavelength end from the data, since the radiance from a $\sim 150\text{ K}$ surface is essentially 0 for wavenumbers larger than 1300 cm^{-1} . There is an important high-frequency component to the darks as well, which also appears to vary slightly from revolution to revolution. These patterns are determined by assuming that the surface spectrum averaged over the whole polar cap, outside the atmospheric CO_2 band, is smooth. When these new darks are used, both individual spectra and small averages of spectra are much better behaved, in that the remaining variations have all the characteristics of random noise.

Previous Work: The seasonal polar caps of Mars are composed primarily of solid CO_2 , likely mixed with some micron-sized Martian dust and water ice. Many of these dust and water ice grains may be brought in as condensation nuclei for CO_2 snow grains. Each polar cap spectra from this revolution has been analyzed by fitting to model spectra of ternary $\text{CO}_2\text{-H}_2\text{O-dust}$ intimate mixtures, including partial spatial coverage, surface temperatures, and water ice clouds [9]. The dust optical properties are poorly known in the important $20\text{--}50\ \mu\text{m}$ region. Those used here are derived from analysis of airborne dust in Mariner 9 infrared spectra [11]. They fit a few low-dust observations, assuming that the surface spectrum is a blackbody. The dust study is continuing by looking at a wider variety of spectra and variable surface emissivity.

The results of this analysis show that the central polar cap is 100% covered by CO_2 deposits, and that the temperature varies as expected (as a function of altitude). The CO_2 grain radius varies between $200\ \mu\text{m}$ and 1 cm , averaging $\sim 1\text{ mm}$, while the dust mass mixing ratio varies from 100 ppm to 1% , averaging 0.1% , and the water ice mass mixing ratio varies from 0 to 0.1% , averaging $\sim 100\text{ ppm}$.

There are several low-emissivity regions in the central polar cap, normally indicated by a large brightness temperature difference between 25 and $18\ \mu\text{m}$. A detail

EVOLUTION OF LOW-EMISSIVITY SPOTS IN THE MARTIAN POLAR CAPS: G. B. Hansen

of the brightness temperature difference, CO₂ grain size, and dust mass mixing ratio over one of these regions as shown in Figure 1. The typical behavior shown here is that the large brightness temperature difference is reflected mostly in the dust mixing ratio, and not the CO₂ grain size, as has been assumed previously [4, 7].

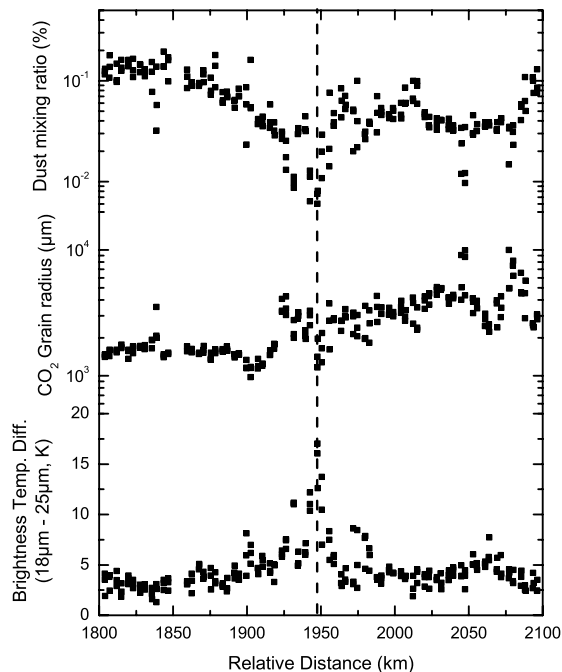
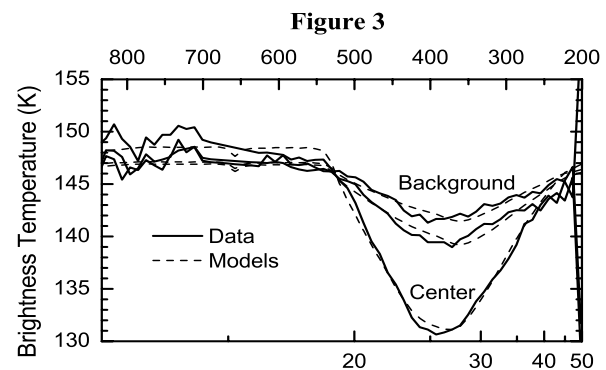
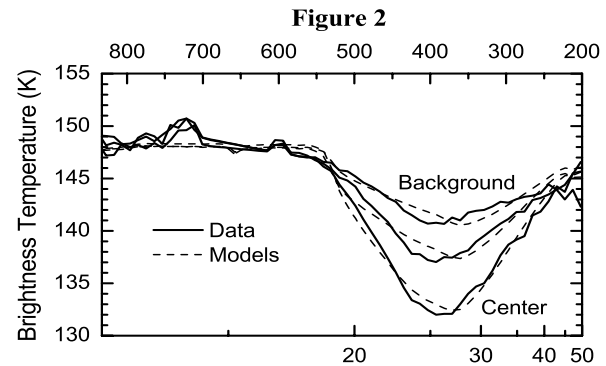


Figure 1

A New Theory: This observation suggests a different process for the temporal and spatial variation of low-emissivity regions. These regions are most likely initiated by fresh CO₂ snowfall from atmospheric dynamic interactions with topographic obstacles. If the CO₂ grains are formed around dust condensation nuclei, the optical properties of the dust are subdued or absent (depending on the ratio of grain size to nucleus size). We will investigate this using layered Mie calculations, but the hiding effect is well known. If the dust nuclei subsequently migrate to the grain boundaries as the deposit matures, the optical effect of the dust will approach the intimate mixing formulation of the models. The effective CO₂ grain size may not change significantly as it matures.

Average spectra from some typical cold spots are shown in Figures 2 and 3. In each case an average from the edges of the low-emissivity region are compared to an average from the center of the region, to show the spectral effect of increased dust at a similar grain size. The background grain sizes is 600 μm, and the dust content varies from 0.01% (center) to 0.1% (edge) in

Figure 2, and the background grain size is 2 mm, and the dust content varies from 0.008% (center) to 0.05% (edge) in Figure 3. The background dust mixing ratio is consistent with an original CO₂ grain size of 12–15 μm around a 2-μm dust nucleus.



References:

- [1] Kieffer *et al.* (1976) *Science*, 194, 1341–1344.
- [2] Christensen P. R. *et al.* (1992) *JGR*, 97, 7719–7734.
- [3] Kieffer *et al.* (2000) *JGR*, 105, 9653–9699.
- [4] Titus *et al.* (2001) *JGR*, 106, 23181–23196.
- [5] Hansen G. B. (1999) *JGR*, 104, 16471–16486.
- [6] Forget, F. *et al.* (1998) *Icarus*, 131, 302–316, 1998.
- [7] Eluszkiewicz, J., and T. N. Titus (2002) *BAAS*, 34, 866.
- [8] Eluszkiewicz, J. (1993) *Icarus*, 103, 43–48.
- [9] Hansen, G. B. (2001) *Eos Trans. AGU*, 82, Fall Meet. Suppl., Abstract P12E-09.
- [10] Christensen P. R. *et al.* (2001) *JGR*, 106, 23823–23871.
- [11] Hansen, G. B., *BAAS*, 34, 844.

UPPER LATITUDE ICE FLOW, GULLIES, AND LONG-TERM GLACIAL HISTORY. W. K. Hartmann, Planetary Science Institute, 620 N. 6th Ave., Tucson, AZ 85705; hartmann@psi.edu

Ice Flow Features: Varied ice-flow-like features have been found in Mars Global Surveyor (MGS) images of moderate to upper latitudes of Mars. Debris aprons give geomorphological suggestions of flow [1], and numerical modeling by Turtle et al. [2] indicates ice flow could deform ice-rich slopes on timescales of 10^3 - 10^4 y, reaching highly deformed, more steady-state configurations within 10^6 y. Crater counts by Berman [3] and the author (unpublished) suggest that the surface structures at scales of 10-60 m on debris apron surfaces are young, with ages as low as 10^6 - 10^7 y. Various aspects of terrain softening, observed in upper latitudes, may also involve ice flow [4]. MGS has shown possible ice-flow softening or viscous relaxation of craters as small as a few km [5].

A dramatic tongue shaped feature on a crater wall at $\sim 38^\circ$ S latitude is likely example of a recent ice flow down the wall [6]. As seen in Fig. 1, the lower crater wall below the tongue is dissected by gullies somewhat different from the classic Malin-Edgett hillside gullies; they may be result of erosion by runoff water from melting of ice in the observed flowing mass, or earlier such masses. Such tongue-like flow features are very rare, but Berman [3] has identified a few similar examples. The south wall of the same crater (unnamed, east of Hellas near Reull Vallis in a region known for debris aprons) also shows flow features, of different morphology. Here, the valleys are filled with chevron-striated deposits that suggest glacial or rock glacial masses.

Relation to Gullies: Hartmann et al. [6] pointed out that the tongue-like apparent flow feature in Figure 1 has a distal crescentic ridge, with a near-concentric, softer arc-like outer ridge further down slope, and that below many Martian hillside gullies similar crescentic ridges can be seen (Fig. 2). Arfstrom [7] gave examples of similar features formed as moraines in terrestrial glaciers, and proposed that these features are moraines formed as glaciers flowed down crater walls after ice mantling. Thus, some gullies may form underneath, or in association with, such ice masses deposited on crater walls. This is consistent with the hypotheses developed by Mustard [8] and Costard et al. [9] invoking deposition of ice-rich dust mantles during long periods of winter cold and dark, during high-obliquity phases of 10^7 y axial tilt cycles.

An explanation for the rarity of beautifully preserved ice flow features such as seen in Figure 1 may be that the flow is fast (as shown by Turtle et al. [2]), and Martian glaciers self-destruct because of high ice losses from the surface of the flowing mass, due to sublimation as the dusty ice mass flows and churns. They may last no more than a few My.

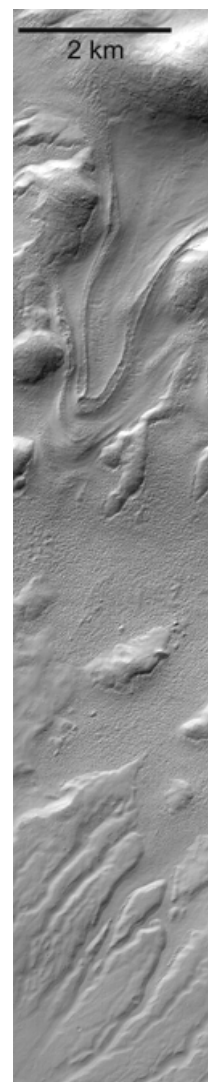


Figure 1. Lobate feature caused by apparent flow down north inner wall of an unnamed crater at 247W 38S. Downhill from the lobate flow, the lower crater wall deposits are dissected by gullying, possibly from runoff associated with ice in previous flows. MOC M18-00897.

UPPER LATITUDE ICE FLOW, GULLIES, AND LONG-TERM GLACIAL HISTORY: W. K. Hartmann

In this view, glaciation and gullying at upper latitudes may come in short-lived episodes launched primarily by ice deposition cycles (and less commonly by local water release, creating ice lenses), and even the moderate upper latitudes of Mars may be viewed geomorphologically as parts of the time-varying polar ice cap.

Long-Term Glacial and Polar History: Tanaka et al. [10] tabulated total areas resurfaced by various processes in different epochs. Using early estimates of Martian chronology based on crater counts, he found that resurfacing by periglacial and fluvial processes declined from high Noachian values. Hartmann and Neukum [11] refined the crater chronology, consistent with ages of Martian igneous meteorites from 170 to 1300 My. Using my own subsequent refinement of those data, I updated the estimates of the durations of the Martian epochs, and computed the rate of resurfacing [(Tanaka total km^2 resurfaced by a given process in a given epoch)/(duration of that epoch)]. The result (Fig. 3) confirms that Noachian/Hesperian periglacial resurfacing rates were an order of magnitude or more the modern rate. Fluvial and volcanic resurfacing also show enhanced Noachian/Hesperian rates relative to the present, indicating that early Mars was a more active and Earth-like environment.

References: [1] Pierce T. L. and Crown (2003) *Icarus*, 163, 46-65. [2] Turtle E. P. et al. (2003) 3rd Intl. Polar Sci. Conf. (this meeting). [3] Berman D. C. (2003) M. S. thesis, U. of AZ, in prep. [4] Squyres S. et al. (1992) In *Mars*, U. AZ Press, Tucson, 523-544. [5] Hartmann W. K. and Esquerdo G. (1999) *Meteor. Planet. Sci.*, 34, 167-177. [6] Hartmann W. K. et al. (2003) *Icarus*, 162, 259-277. [7] Arfstrom J. (2003) *LPS XXXIV*, Abstract #1174. [8] Mustard J. F. et al. (2001) *Nature*, 412, 411-413. [9] Costard F. et al. (2003) *Science*, 295, 110-113. [10] Tanaka et al. 1987. *Proc. Lunar Planet Sci Conf. 18th*, 665-678. [11] Hartmann W. K. and Neukum G. (2001) *Space Sci. Rev.*, 96, 165-194 with modest updated revisions by W. K. Hartmann, in preparation).

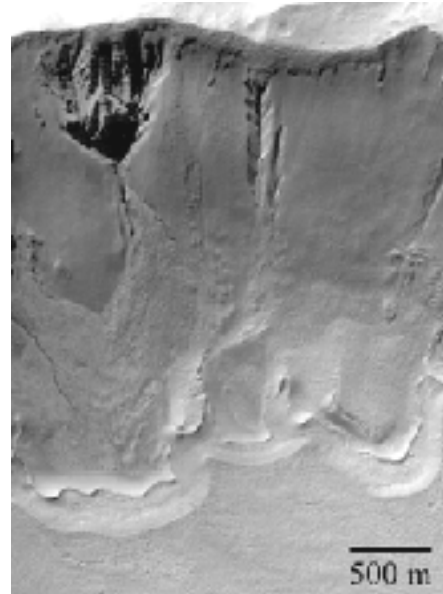


Figure 2. Typical Martian gully system showing sharp arcuate ridge bounded on outside by softer ridges, at the base of the gullied hillside. The arcuate forms, which may be moraines, are similar to those at the foot of the glacier-like mass in image A, suggesting that glacier-like ice rich masses may be associated with gully production. 166W39S MOC M18-00303.

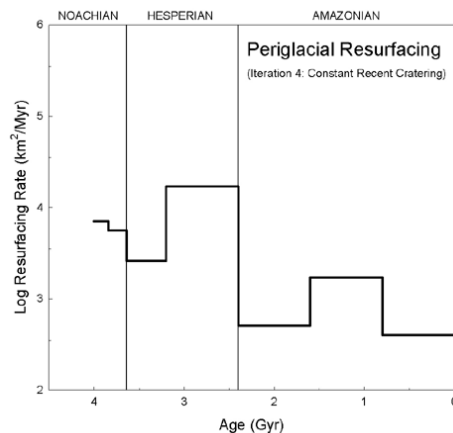


Figure 3. Plot of rate of resurfacing by periglacial processes as a function of time, derived by dividing total area of periglacial resurfacing in each epoch [10] by durations of the epoch [11]. Various timescale by Neukum and by Hartmann agree that Noachian-Hesperian periglacial resurfacing rates were an order of magnitude higher than present values.

EXTENSIVE HESPERIAN-AGED SOUTH CIRCUMPOLAR ICE SHEET ON MARS: DORSA ARGENTEA FORMATION SYNTHESIS: James W. Head¹, Gil J. Ghatan¹ and David Marchant², ¹Dept. Geol. Sci, Brown Univ., Providence, RI 02912 USA, ²Dept. Earth Sciences, Boston Univ., Boston, MA 02215 USA, james_head@brown.edu

Introduction and background: The nature of the climate in early Mars history, and whether pluvial conditions prevailed [e.g., 1] during the Noachian Period (~4.6-3.7 Ga) [2], or if an ocean existed then and/or during the Hesperian Period (~3.7-3.0 Ga) [3], are matters of major debate and investigation. The Dorsa Argentea Formation [4] (DAF) is a south circumpolar deposit of Hesperian age [2] and thus may record the aftermath of Noachian-aged climate and volatile evolution. Here we outline a synthesis of the characteristics of the DAF, and show that these are consistent with the presence of a major water-ice-rich circumpolar deposit during the Hesperian, and its partial melting, sublimation and retreat. We outline interpretations for the source and fate of these volatiles and their significance to polar and hydrological processes and history.

The Dorsa Argentea Formation: Underlying the present Amazonian-aged polar cap (Apl, residual ice and Apl, layered terrain) lies the Hesperian-aged Dorsa Argentea Formation, Hd, and related units [4] (Figure 1) (here collectively called the DAF). This deposit covers a surface area that could be as large as 2.94×10^6 km² (about 2% of the surface of Mars), over twice the area of the present Amazonian-aged deposits. Originally interpreted as largely volcanic in origin [4], this deposit has been reinterpreted on the basis of new MGS data as a volatile-rich ice-sheet-like unit that underwent melting and retreat [5] or, alternatively, a deposit caused by release and emplacement of subsurface volatiles and debris [6]. Here we synthesize the evidence for the DAF and related units representing an extensive south circumpolar glacial-like deposit that underwent significant melting, sublimation and retreat [5].

Sinuuous Channels Along the Eastern DAF Margin: Along the eastern margin of the continuous deposit of the DAF (Figure 1; 1) are located a series of sinuous channels that lead away from the margin of the deposit and enter nearby craters, exiting them from downslope margins, crossing intercrater terrain and entering other craters [7]. The channels connecting these craters provide evidence for extensive crater flooding, ponding (minimum volumes of $\sim 10^{12}$ m³), overtopping, downcutting, and continuous drainage of material through a series of craters and into the Prometheus Basin near the edge of the current polar cap. Topography data show that water filled some craters to depths of at least 200 m and possibly as much as 600 m. Water exiting from the edge drained over a lateral distance of ~600 km and a vertical height of ~800 m. These data provide evidence for the water-rich nature of the DAF, its subsequent melting and collapse, and the overland drainage of its meltwater effluent [7].

Concentric Ridges: Nearby these marginal channels but inward of the DAF margin (Figure 1, 2) lies a series of arcuate ridges that are convex-outward from the DAF margin. These have been interpreted to be push moraines derived from bulldozing of ice and sediment at the margins of the DAF [8].

Sisyphi Lobe and Broad Depression: One of two major lobes of the DAF is the Sisyphi Lobe that extends out from the south pole toward 0° (Figure 1). Largely surrounded by Noachian cratered terrain, the deposit in this area is shown by MOLA data to be a topographic low [9], and smooth at small scales, but containing a large-scale pitted texture and a number of unusual mountains.

Unusual Mountains: Located within the Sisyphi Lobe are a number of isolated mountains with average separation distances of ~175 km (Figure 1; 3); these are typically 30-40 km in diameter and ~1-1.5 km high, with their bases falling near an elevation of ~1200 m. The unusual shapes of these mountains as well as the alignment of many, and the sinuous channels emanating from the base of several, has led to the interpretation [10] that they are of volcanic origin, with their unusual morphology and morphometry being accounted for by their eruption under an ice-sheet. Assessment of edifice morphometry led to the conclusion that the overlying ice sheet had a minimum thickness of ~1.4 km [10].

Cavi Sisyphi: Located within the Sisyphi Lobe are a series of irregular and elongate depressions that are typically about 500 m deep and have relatively steep marginal slopes (~11°) (Figure 1; 4). Within several of these are sinuous ridges that have been interpreted to be eskers and are oriented in directions consistent with regional drainage from regions within the DAF that appear to have undergone melting (likely related to the features interpreted as subglacial volcanoes) and drainage toward the margins of the DAF where large channels emerge and wind toward the floor of Argyre [11].

Angusti Lobe: Oriented radially from the south pole toward 70° W is a broad lobe of positive topography which we describe as the Angusti Lobe (Figure 1).

Cavi Angusti: Within the Angusti Lobe lie Cavi Angusti (Figure 1; 5), a series of basins similar to Cavi Sisyphi in surface area and wall steepness, but differing in several important ways. These basins are typically deeper (~1000 m) and contain centrally located mountains or ridges, which have been interpreted to be volcanic edifices [12]. The terraced interiors and central mountains of many cavi have been interpreted to mean that the basins formed as a result of magmatic intrusion and extrusions causing heating and melting of a water-rich substrate (the overlying DAF) and drainage of the liquid water. Meltwater from basin formation appears to have drained laterally and may also have reentered the subsurface groundwater system [12].

Dorsa Argentea: A series of sinuous and overlapping ridges extend for several hundreds of km from the interior of the DAF toward the margins (Figure 1; 6). A range of different interpretations have been offered in the past [5] but recently terrestrial analogs and topography data have been used to develop detailed criteria for the recognition of eskers on Mars [13]. Application of these criteria has strengthened the interpretation that these ridges are eskers and that they represent the drainage of meltwater products from the interior of the DAF toward the margins, out into an adjacent lowlying region interpreted to be a lake [14].

Lowlands Around Schmidt Crater: Adjacent to the Angusti Lobe is a low-lying smooth area (Figure 1; 7) interpreted to be a region in which meltwater from the central DAF was delivered and which collected before ultimately draining through a channel in the surrounding topography and down into the Argyre Basin. Informally called Lake Schmidt, this region covers an area of ~270,000 km², five times the size of Lake Michigan and may have been in excess of 300 m deep [14]. Also observed is a series of pits in a narrow zone located along the boundary between the Angusti lobe and the adjacent

SOUTH CIRCUMPOLAR ICE SHEET: J. W. Head et al.

lowlands; this has been interpreted to be a contact zone between the ice sheet and the lake, in which the pits are comparable to kettle holes formed due to melting of residual ice blocks [15].

Pedestal Craters: Craters with extensive elevated ejecta deposits occur within the DAF with the most prominent one (Figure 1; 8) characterized by marginal ~500 m high scarps [5], suggesting that material removed from below this armor-ing deposit was at least 500 m thick.

Mountains near South Crater: A series of distinctive mountain peaks occur near South crater (Figure 1; 9) and their morphology suggests that their lower portions were buried by the DAF but that their upper portions were surrounded by the DAF. On the basis of their morphology and unusual structure, we have interpreted these to be nunataks, mountains which rise above surrounding ice sheets.

Hr relationships: Located along the eastern edge of the Sisyphi Lobe (Figure 1; 10), and defining the margin of the DAF is an extensive scarp between the DAF and Hr (ridged plains interpreted to be of volcanic origin). This unusual scarp faces inward toward the DAF and is interpreted to have formed by the emplacement of Hr lavas from sources in Malea Planum up against the DAF, forming a constructional ridge against the ice sheet. Subsequent to the decay of the ice sheet the scarp remains and is now facing inward toward the DAF. The presence of this scarp may help to explain why much of the meltwater appears to have drained into the Prometheus and Argyre Basins, and not out into Hellas.

Channels Marginal to the DAF: Inspection of the DAF along the western margins of the Sisyphi Lobe, as well as along the eastern margins of the Angusti Lobe, reveals the presence of channels that are arrayed radially away from the deposit (Figure 1, white lines). These several large channels begin at and near the margins of the DAF; some can be traced back into the deposit and are continuous with esker-like ridges and elongate cavi in the DAF [16]. These channels lead from the DAF margins northward, draining downslope for distances from 1000-1600 km onto the floor of the Argyre Basin, some

3.5-4.0 km below their origins. The channels do not exhibit tributaries and are sometimes discontinuous in flat regions where ponding may have taken place. Their characteristics suggest that a significant portion of the DAF meltwater entered a surface distribution system that transported it to the floor of Argyre [5].

Synthesis: These characteristics of the DAF and adjacent deposits lead us to the interpretation that the unit represents the remnants of a major south circumpolar ice-rich deposit that existed in the Hesperian and that underwent significant melting, sublimation and retreat. Estimates of the present deposit thickness, and the amount of material thought to have been removed suggest that the original volume could have been as much as $5.9 \times 10^6 \text{ km}^3$, equivalent to a global layer of water ~20 m deep if the deposit consisted of 50% volatiles. Positive evidence is seen for bottom-up melting (volcanic eruptions); top-down melting may also have occurred. Some of the water from this melting drained laterally overland, but a significant portion may well have entered the groundwater system, potentially recharging the global aquifer [3]. A portion of the volatiles are predicted to have remained in the deposit, representing a net removal from the atmosphere and from the active hydrologic system. Today the DAF forms an accessible record of aqueous conditions and possible biological environments dating from early Mars history.

References: 1) R. Craddock and A. Howard, JGR, 10.1029/2001JE001505, 2002; 2) W. Hartmann and G. Neukum, Space Sci. Rev., 96, 165, 2001; 3) S. Clifford and T. Parker, Icarus, 154, 40, 2001; 4) K. Tanaka and D. Scott, USGS Map 1802-C, 1987; 5) J. Head and S. Pratt, JGR, 106, 12275, 2001; 6) K. Tanaka and E. Kolb, Icarus, 154, 3, 2001; 7) S. Milkovich et al., JGR, 10.1029/2001JE001802, 2002; 8) S. Milkovich and J. Head, Microsymposium 24, 2001; 9) J. Head and G. Ghatan, LPSC 32, #1062, 2001; 10) G. Ghatan and J. Head, JGR, 10.1029/2001JE001519, 2002; 11) G. Ghatan and J. Head, LPSC 34, #1129, 2003; 12) G. Ghatan et al., JGR, 10.1029/2002JE001972, 2003; 13) J. Head and B. Hallet, LPSC 32, #1366, #1373, 2001; 14) J. Head and S. Pratt, LPSC 32, #1159, 2001; 15) J. Dickson and J. Head, LPSC 34, #1185, 2003; 16) G. Ghatan and J. Head, 6th Mars Conf., #3034.

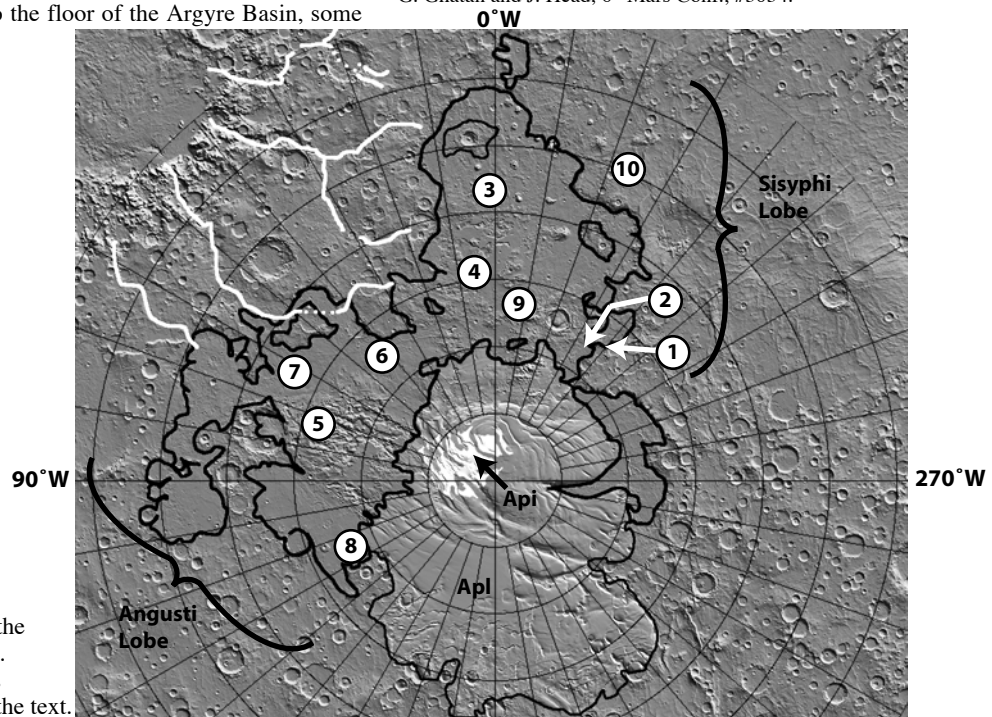


Figure 1. Distribution of the DAF and related deposits. Numbers refer to features and regions described in the text.

TROPICAL MOUNTAIN GLACIERS ON MARS: EVIDENCE FOR AMAZONIAN CLIMATE CHANGE:

James W. Head¹, David E. Shean¹, Sarah Milkovich¹ and David Marchant², ¹Dept. Geol. Sci, Brown Univ., Providence, RI 02912 USA, ²Dept., Earth Sciences, Boston Univ., Boston, MA 02215 USA, james_head@brown.edu

Introduction and background: Polar deposits on Mars represent one of the most significant current volatile reservoirs on the planet and these, together with high-latitude surface and near-surface ground ice, the global cryosphere, possible groundwater, and small amounts of atmospheric water vapor, represent components of the hydrological cycle. Recent Odyssey data have been interpreted to signify the presence of significant amounts of near-surface ice at mid-to high latitudes in both hemispheres [1]. These deposits, together with other topography and morphology data, have been interpreted to mean that volatile-rich deposits have been emplaced from about 30° north and south latitude to the poles during obliquity excursions on the order of <35° [2], perhaps relatively recently, in agreement with predictions from climate models [3].

In this contribution, we outline evidence for the accumulation of ice deposits below 30° north and south latitude during the Amazonian Period. These near-equatorial ice accumulations take the form of tropical glacier deposits that extended outward from the flanks of the Tharsis Montes and Olympus Mons (Figure 1).

Interpretation of Glacial Landforms on Mars: Recent terrestrial studies as well as analysis of landforms on Mars have led to a new understanding of cold-based glacial landforms [e.g., 4]. Although cold-based glaciers do not erode their underlying substrates appreciably, they do deposit characteristic landforms. The material within these landforms originates from supraglacial debris, commonly rockfall and/or volcanic ejecta that falls onto the glacier surface. These rockfall and volcanic particles flow passively through the ice toward glacier margins. During deposition, the resulting landforms (e.g., drop moraines, sublimation till, rock-glacier deposits) are perched on existing topography. Sharp basal contacts and undisturbed underlying strata are hallmarks of cold-based glacier deposits.

The term *drop moraine* is used here to describe ridges that form as supra- and englacial particles are dropped passively at the margins of cold-based glaciers. In the Dry Valleys, such moraines may be cored by glacier ice, owing to the insulating effect of the debris on the underlying glacier. In plan view, drop moraines closely mimic the pattern of former ice margins, though moraine width may vary spatially, owing to the characteristic inhomogeneity in the distribution of supraglacial debris.

Sublimation along the ice-atmosphere interface may bring englacial debris passively to the ice surface. The rate of ice sublimation slows as the evolving sublimation till thickens, eventually insulating the underlying ice by retarding vapor diffusion and thermal change. Many *sublimation tills* in the western Dry Valleys region of Antarctica are underlain by glacier ice, even though some are in excess of a few Ma. Differential flow of underlying glacier ice may result in distinct surface lobes of sublimation till

In the western Dry Valleys region of Antarctica, *rock glaciers* form as sublimation concentrates debris on the surface of active glaciers. Continued flow of the underlying glacier through internal deformation produces ridges and lobes of sublimation till atop the glacier. The thickness of this debris increases down ice flow, as material is continually added to the base of the sublimation till as it moves down valley. In general, rock glacier formation is favored by high debris accumulation rates and low ice velocities, conditions com-

mon in an advanced state of glacial retreat. Spoon-shaped hollows that commonly form at the head of many terrestrial rock glaciers likely arise due to excess sublimation in areas with incomplete debris cover as opposed to preservation by the more extensive tills down valley.

Three shield volcanoes, collectively known as the Tharsis Montes, cap the broad Tharsis Rise, a huge center of volcanism and tectonism spanning almost the entire history of Mars. Olympus Mons is located on the flank of the rise (Figure 1). Each of these volcanoes, although largely constructed of effusive and explosive volcanic deposits, contains a distinctive and unusual lobe, or fan-shaped deposit on their west-northwestern flank. These deposits consist of three facies and various hypotheses have been proposed for their origin including one or more of the following: lahars, debris avalanches, landslides, pyroclastic flows, and/or generally related to the advance and retreat of ice [see review in 5].

New Mars Orbiter Laser Altimeter (MOLA) altimetry and Mars Orbiter Camera (MOC) images from the Mars Global Surveyor spacecraft have permitted us to characterize the fan-shaped deposits in much more detail. On the basis of present surface temperatures on Mars and those of the recent past, any mountain glaciers would likely be cold-based and most similar to the slow-moving, cold based glaciers of the Dry Valleys region of Antarctica. We outline here the deposit characteristics and use Antarctic Dry Valley analogs to aid in their interpretation.

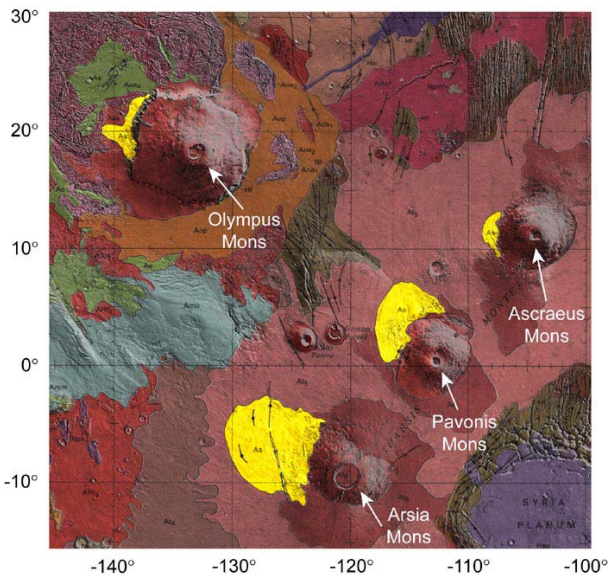


Figure 1. Geologic map of Mars showing the fan-shaped deposits (yellow, unit As) associated with the northwest flanks of the Tharsis Montes and Olympus Mons [8].

Arsia Mons: At Arsia Mons, an outer ridged facies that consists of multiple laterally extensive, arcuate and parallel ridges resting without disturbance on both well-preserved lava flows and an impact crater, is interpreted to be a series of drop moraines formed at the margin of an ablating and predominantly receding cold-based glacier. A knobby facies that consists of equidimensional

knobs, each up to several kilometers in diameter, is present inward of the ridges; this facies is interpreted as sublimation till derived from *in situ* downwasting of ash-rich glacier ice. A third facies comprising distinctive convex-outward lobes with concentric parallel ridges and aspect ratios elongated downslope likely represents rock-glacier deposits, some of which may still be underlain by a core of glacier ice. Taken together, these surficial deposits show that the western flank of Arsia Mons was occupied by an extensive mountain glacial system accumulating on and emerging from the upper slopes of the volcano and spreading downslope to form a piedmont-like fan occupying in excess of 180,000 km². We find little evidence for meltwater features in association with any facies, and thus conclude that the glacier ice was predominantly cold based throughout its history and ablation was largely by sublimation.

Pavonis Mons: The Pavonis fan-shaped deposit (Figure 1) extends approximately 250 km northwest of the shield base [6]. The deposit ranges from 3.0-8.5 km above the Mars datum and covers an area of 75,000 km², approximately half of the area covered by the Arsia deposit. The ridged facies consists of a series of hundreds of concentric, parallel ridges around the distal margins of the deposit. The ridged facies is also observed in the central regions fan-shaped deposit, with some inner ridges only 70 km from the base of the shield. This geographic distribution of the ridged facies is unique to Pavonis. We interpret these ridges as drop moraines formed at the margins of a retreating cold-based glacier. A knobby or hummocky facies, that lies both inward and outward of the ridged facies, consists of sub-km scale knobs and depressions that are sub-rounded to elongated downslope in places. The knobby facies appears to superpose underlying features including the ridged facies, and we interpret it to be a sublimation till derived from *in situ* down-wasting of ash-rich glacier ice. There are four isolated regions of the smooth facies within the Pavonis deposit, the largest extends into the central regions of the fan-shaped deposit.

Additional evidence in support of the glacial hypothesis is seen where the Pavonis fan-shaped deposit is bounded to the east by lava flows. A large scarp exists in these regions where the fan-shaped deposit is 200-250 m lower than the adjacent Tharsis plains. It appears that these lava flows were deflected from flowing toward lower topographic areas and instead continue for over 100 km to the north-northwest. The most likely explanation is that a large ice sheet with a relief of at least 250 m blocked westward flow at the time of lava emplacement.

An area of several, high relief, unique flow-like features exists in the western regions of the fan-shaped deposit. These features are morphologically different from subaerial lava flows at higher elevations on the flanks of Pavonis outside the fan-shaped deposit and also from flows on the Tharsis plains beyond the fan-shaped deposit to the west. They consist of elevated plateaus with leveed edges and steep walls, some with relief of over 500 m. Also present in the central regions of the fan-shaped deposit are several linear ridges. These ridges are radial to the base of the shield and have dimensions of approximately 100-200 m high, 1 km wide, and 30-60 km long. Analysis of high-resolution MOC images and THEMIS Day IR images suggests that these features may be flows and radial dikes, which erupted in a subglacial environment.

Ascraeus Mons: Ascraeus Mons has the smallest fan-shaped deposit of the three Tharsis Montes, which extends approximately 90 km from the base of the

shield [7] and covers an area of around 30,000 km². The strong westerly trend and small size of the deposit confine the accumulation zone for the glacier on the lower western flanks of Ascraeus Mons. Within the fan-shaped deposit, we see a well-defined ridged facies around the outer margins of the deposit as well as an area of the knobby facies in the central regions. Several flow-like features are also present, similar to those observed at Pavonis. They appear to emanate from a series of fractures to the southwest of the fan-shaped deposit. These flows form a large, 300 m high scarp that is roughly concentric to the outer margin of the Ascraeus fan-shaped deposit, suggesting that they were emplaced at a time when an ice sheet was still present at Ascraeus. The most obvious dissimilarity between the Ascraeus deposit and those at Arsia and Pavonis is the absence of the smooth facies. The lack of a smooth facies at Ascraeus may indicate that it was never present or that underlying volatiles have completely sublimated away due to recent climatic conditions.

Olympus Mons: Extending from the base of the Olympus Mons scarp is a unit consisting of several facies, the most extensive of which are fan-shaped deposits including multiple lobate deposits extending up to 90 km from the base of the scarp. Individual lobes are characterized by regular, arcuate, subparallel ridges up to 60 km long. Many depressions are found in this unit; several are circular and are interpreted as small impact craters while others are irregularly shaped. Depressions tend to be hundreds of meters wide and thousands of meters long with depths on the order of tens of m. One lobe is approximately 700 m high and concave in topographic profile. The margins of the lobes are marked by linear ridges hundreds to thousands of meters long and tens of meters high. This unit is interpreted as the remnants of debris-covered glaciers extending from the basal escarpment. The ridges are interpreted to be moraines. Cross-cutting relations imply several episodes of advance and retreat.

Five lobes on Olympus Mons can be traced back to cirque-like hollows in the basal escarpment. The steep scarps at the heads of these erosional hollows rise approximately 4 km above the fan-shaped deposits, and may have served as the accumulation regions. The characteristics of the Olympus Mons fan-shaped deposits are similar in scale and morphology to features within the Tharsis Montes deposits interpreted to be rock glaciers to rock glaciers in the Antarctic Dry Valleys. The ridges at the outer margins of the deposit lobes are interpreted to be distal moraines and the concentric ridges to be drift ridges typical of Antarctic Dry Valley and may other rock glaciers.

Summary and Conclusions: During the Amazonian, significant climate changes created conditions that permitted accumulation of ice deposits in excess of several hundreds of meters thickness, their spreading away from the base of the volcanoes, and their retreat and readvance. Deposits range up to 180,000 km² in area and must have persisted for significant periods of time. These deposits provide evidence for the existence of tropical mountain glaciers and are testimony to the possibility of radical climate changes that might have accompanied orbital parameter perturbations such as obliquity excursions in excess of 45°.

References: 1) W. Feldman et al., *Science*, 297, 75-78, 2002; 2) J. Mustard et al., *Mars* 6, #3250, 2003; 3) M. Richardson and J. Wilson, *JGR*, 107, 7.1-7.28, 2002; 4) J. Head and D. Marchant, *Mars* 6, #3087, 2003; 5) J. Head and D. Marchant, *Geology*, 31, 7, 2003; 6) D. Shean and J. Head, *Mars* 6, #3036, 2003; 7) J. Zimbelman and K. Edgett, *LPSC* 22, 31, 1992; 8) D. Scott and K. Tanaka, USGS Map #I-1802-A, 1986.

SPECULATIONS ON ORBITAL FORCING OF SUBLIMATION FROM THE POLAR CAPS M. H. Hecht,
Jet Propulsion Laboratory, California Institute of Technology (michael.h.hecht@jpl.nasa.gov)

Introduction: Calculation of the periodic variations in the martian orbital parameters by Ward [1] and subsequent refinements to the theory [2,3] have inspired numerous models of variation of the martian water cycle. The limitations of models such as this can not be overstated. Albedo, for example, has a much greater influence on temperature than orbital forcing, and seems to be linked to insolation, possibly via its influence on dust transport [4]. To make further progress, either new constraints must be identified, or additional clues must be obtained from remote sensing and *in situ* exploration.

The MGS and Odyssey missions have provided us with several such critical pieces of information. The discovery of what can only be described as an ice sheet underlying a lag deposit over enormous areas of both hemispheres is one such clue [5], along with indications from surface features of recent, wide-scale modification by water [6]. Another is the observation of mantling of gullied slopes, presumably a vestigial layer of frost and snow protected by a similar lag deposit [7]. More speculative, perhaps, are suggestions from analysis of MOLA data of a net seasonal increase in thickness of the northern cap [8], or correlation of PLD structures with orbital variations dominated by precession of the L_s of perihelion [3]. Speculative implications of these new data are summarized in the sections below.

Critical oscillations: Most orbital forcing models have focused on variations in planetary obliquity (on both a short-term, 110 kyr time scale and larger oscillations occurring over millions of years) [9-11]. The fastest mode of variation, perihelion precession, has generally been deemphasized because it does not change the integrated annual insolation. But as a result of this precession, the asymmetry in peak summer insolation between the poles exceeds 50% today, with the maximum cycling between poles every 25.5 kyrs. Variations in planetary eccentricity also play a role, defining the magnitude of the excursions associated with this perihelion precession.

Fanale, for example, concluded that precession of the longitude of perihelion may be sufficient to increase water removal from the poles by factors of 50-100 [9]. He calculated the peak vapor pressure at the North Pole by assuming a surface of pure water ice or CO_2 ice with distinct optical properties, incorporating only radiative balance and latent heat of CO_2 deposition. It was further assumed that the zonal humidity was proportional to that peak water vapor, which was

in turn a simple function of the ice surface temperature. This assumption is reasonable because the energy deposited as sunlight into the polar cap must ultimately be accommodated in the form of sublimation. If advection or vertical transport is insufficient to remove the generated water vapor, for example, it will recondense as fog, pumping heat into the atmosphere and either generating convective currents or increasing the saturation vapor pressure.

Figure 1 shows the results of calculations using a protocol similar to Fanale's, but with the critical addition of tracking latent heat of water condensation and sublimation. All three curves represent an extrapolation back only 150 kyrs. Rather than extrapolating back far enough to reflect large changes in obliquity, the obliquity was forced to specific values. Thus one curve represents the calculated obliquity, a second holds the obliquity at the current value of 25° , and the third holds the obliquity at 40° . The data is expressed in terms of the amount of heat from insolation that is converted to sublimation under these circumstances. It can be seen that, at constant obliquity, the sublimation rate can increase by a factor of 100 with the passage of only 20 kyrs. Changing the obliquity from 25° to 40° adds another factor of only approximately 5.

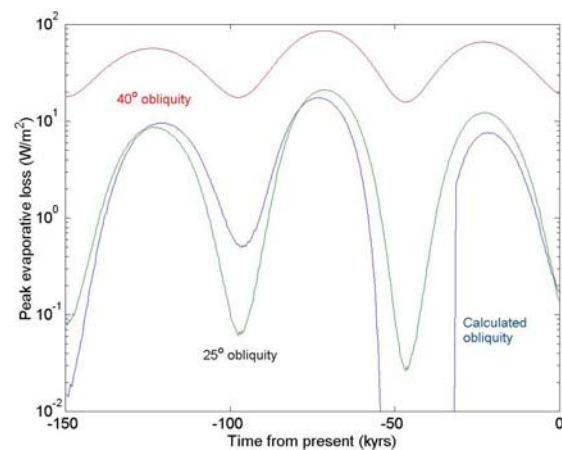


Figure 1: Calculated peak evaporative loss at the North Pole of Mars, expressed as an evaporative heat measure over 150,000 years. The calculation balances radiation, latent heat of CO_2 and H_2O , and insolation using orbital parameters from Ward [1], albedo and emissivity values suggested by Fanale et al [9]. To show the relative effect of precession and obliquity, the three curves represent calculated obliquity and obliquity fixed at 25° or 40° .

Lag deposits and ice cap evolution: Odyssey results suggest that the vast majority of ice on Mars is sequestered beneath either a lag deposit of dust or a buffer layer of CO₂. The reason for this seems straightforward – the water table will retreat to a depth such that the annual thermal wave does not result in temperatures above the dewpoint [12]. In other words, the boundary of the cryosphere will tend to adiabatically adjust to the changing heat balance. The southern hemisphere is currently favored by summer perihelion, and not surprisingly exposed water is scarce. To the extent that cap evolution can track climate change, the boundary of the exposed northern polar cap would represent the latitude above which the surface temperature doesn't exceed the frostpoint.

The appearance of the PLD and the apparent high resurfacing rates of the cap itself [13] suggest that the age of the cap isn't geologically great. There are few polar features suggestive of flow, implying that the cap periodically retreats by other processes, presumably sublimation and transport to lower latitudes or the opposing hemisphere. The time scale for disappearance and reconstruction of the cap has never been resolved, but could range from many millions of years to the rapid 51,000 year cycle of precession.

As the northern hemisphere warms up due to orbital precession, two things may occur. The boundaries of the cap may be encouraged to retreat to higher latitude, and measurable amounts of water may be seasonally removed from the polar cap. If formation of a lag deposit halts the surface erosion of the cap, then further erosion may be limited to the scarps and slopes at the edges of the cap, effectively eroding the cap from the outside. Only by vigorous removal on the perimeter, where gravitational forces remove the residue, could the cap be substantially modified on the timescale suggested by the geological record. Supporting such a view is the observation that as ice sublimates, surface facets will tend to grow normal to the sun direction, maximizing further erosion [14]. We might imagine, therefore, that as the summers become hotter in the north over the next 20,000 years, the diameter of the northern cap will become smaller, with material being vigorously removed from the edges and redeposited on top. Indeed, if the net increase in thickness of the cap suggested by the MOLA data were verified, it would not be inconsistent with such a mechanism. It is also not unreasonable that the cap would bifurcate into two regions – a high latitude, actively growing region with thermally stable exposed ice, and a lower latitude region with suppressed growth, where a lag deposit protects the ice from further erosion.

Conclusions: Models of peak seasonal sublimation from the north polar cap suggest that the important cycle of water injection may be 25.5 or 51 kyrs, depending on whether one or two poles are involved. If the process is limited by hemispheric depletion of available dust-free water, the result may be periodic pulses of water injection. The tendency of the surface to form lag deposits above ice layers is consistent with an equilibrium water table determined by the frostpoint. As temperatures warm, this stability level will retreat below the surface at higher latitudes, encouraging polar cap retreat. The ability of the cap to shrink from the surface may also be limited by lag formation, suggesting that the cap grows and shrinks from the perimeter, with the sublimed material being transported from perimeter to top surface. Favorable geometries with respect to the sun would make this an efficient form of water transport.

References: [1] Ward W.R. (1974), *J. Geophys. Res.* 79, 3375-3386. [2] Laskar J. (1990), *Icarus* 88, 266-291. [3] Laskar J., Levrard B., Mustard J.F. (2002), *Nature* 419, 375-377. [4] Kieffer H.H., Zent A.P. (1992), in *Mars*, ed. H. H. Kieffer et al., 1180-1218. [5] Boynton, W. et al. (2002), *Science* 297 81-85. [6] Kreslavsky M. and Head J. (2000), *JGR* 105, 26695. [7] Christensen P.R. (2002), *Nature* 422, 45-48. [8] Smith, D. E., M. T. Zuber, G. A. Neumann (2001), *Science* 294, 2141. [9] Fanale F.P. et al. (1986), *Icarus* 67, 1-18. [10] Carr, M.H. (1982), *Icarus* 50, 129-139. [11] Hecht M. H. (2002), *Icarus* 156, 373-386. [12] Leighton R.B., Murray B.C. [1966], *Science* 153 136-144 [13] Herkenhoff, K. E. and J. J. Plaut (2000), *Icarus* 144, 243-253. [14] Ingersoll A.P., Svitek T., Murray B.C. (1992), *Icarus* 100, 40-47.

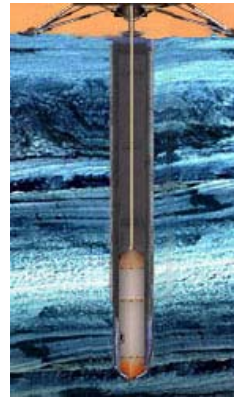
Acknowledgements: This work was performed at the Jet Propulsion Laboratory, California Institute of Technology, under funding from NASA. Useful discussions with Frank Carsey are greatly appreciated.

CRYOSCOUT: A DESCENT THROUGH THE MARS POLAR CAP M. H. Hecht¹ and R. S. Saunders², ¹Jet Propulsion Laboratory, California Institute of Technology (michael.h.hecht@jpl.nasa.gov), ²NASA Headquarters, Washington, D.C. (ssaunde1@hq.nasa.gov)

Introduction: Recent discoveries on Mars—from the numerous gullies seen by Mars Global Surveyor (MGS) to the vast expanses of near-surface ice seen by Odyssey—draw attention to the importance of a modern hydrological cycle and the possibility of extreme climate variations driven by orbital forcing. The surface/atmosphere interactions that define this cycle are presumably reflected in the stratigraphy of the polar layered deposits (PLD), comprising a climate archive that possibly spans many millions of years. If a terrestrial ice sheet were so endowed it would be studied by coring, in order to retrieve the most pristine record of past chemical and physical properties, and to evaluate modification induced by time and stresses within the ice. On Mars' north polar cap, thermal probes are feasible and can provide a reasonable approximation of coring. Optical and spectroscopic analysis of the layers, which are presumably demarcated by embedded dust, would contribute to the reconstruction of a timeline. Meltwater analysis is a convenient way to determine the soluble chemistry of that embedded dust, and to monitor gradients of the isotopic ratios of hydrogen and oxygen that reflect atmospheric conditions at the time the layer was deposited. As on Earth, local thermal measurements can be used to determine bulk mechanical properties of the cap, as well as the geothermal gradient.

CryoScout was proposed as just such a subsurface investigation of the stratigraphic climate record embedded in Mars' North Polar cap (Figure 1). After landing on a gentle landscape in the midst of the mild summer season, CryoScout was to use the continuous polar sunlight to power the descent of a "cryobot," a thermal probe, into the ice at a rate of about 1 m per day. CryoScout would probe deep enough into this time capsule to see the effects of planetary obliquity variations and discrete events such as dust storms or volcanic eruptions. By penetrating tens of meters of ice, the mission would explore at least one of the dominant "MOC layers" observed in exposed layered terrain.

CryoScout's primary objective was to determine the conditions under which the north PLD, the only known unmodified and accessible record of recent Mars climate history, was laid down over the past million years. Secondary objectives were to characterize the present-day polar cap structure and surface conditions. These objectives would be pursued by acquiring data on the present surface mass balance and the varia-



tion of compositional, physical, and thermal properties as a function of depth below its surface.

Figure 1: Fueled by continuous sunlight on Mars' North Pole, the cryobot uses heat to sink through undisturbed polar layered deposits.

CryoScout's detailed log of images, temperature, and compositional data, would reflect the influence of meteorology, depositional episodes (volcanic, impact, dust storms), and planetary orbital/axial modulation. Among the questions CryoScout might address are these:

- How has the climate changed with orbital parameters in the past million years? Can such change explain young gullies (MGS) or evidence of ground ice (Odyssey)?
- What is the fine-scale stratigraphy of the North Polar cap?
- What is the inventory of dust, salts, and organic compounds incorporated into the ice?
- What is the inventory of volatiles, including water, CO₂, and clathrate hydrates?
- Has there been recent volcanism on Mars?

Mission Overview: As proposed for the recent Scout competition, a Type 2 trajectory was to deliver a cryobot [1] and surface instruments to the North Polar region of Mars in 2008, arriving at L_s=73, just before the summer solstice. CryoScout would then be in continuous sunlight throughout the 90-day mission, during which the cryobot would penetrate about 80 m into the North PLD. Powered by a large, tracking solar array, the cryobot would descend an average of 4 cm per hour, transmitting data through a tether that slowly unreels from its aft bay.

Six instruments were selected to accomplish the CryoScout goals. IceCam, the cryobot camera, would record the visible stratigraphy. With 1-mm vertical resolution in nephelometer mode, IceCam would provide a time resolution of months to centuries (assuming deposition rates of 0.01–10 mm per year [2]). In imaging mode, IceCam would acquire full-color stereo images at 10⁻⁵ m per pixel, probably sufficient for observing annual layers similar to terrestrial varves.

By analyzing the meltwater with a suite of electrochemical sensors, the Mars inorganic chemistry analyzer (MICA) would determine the salt composition and abundance in the embedded dust, providing clues to its origin. The Mars isotopic laser hygrometer (MILH) would measure variations in relative hydrogen- and oxygen-isotope abundance in that same meltwater, reflecting source and climate conditions under which the ice was deposited.

A fiber thermometer incorporated into the tether linking the cryobot to the surface, the Distributed Temperature Sensor (DTS) would measure the time-dependent ice temperature profile, including the thermal wave penetration in the top ~20 m and geothermal heat flux below. The DTS would determine both conductivity and diffusivity, which are needed for macroscopic models of the ice structure and evolution.

The dynamics of the polar cap surface were to be studied through imaging with the stereoscopic surface imager (SSI), which would also measure the thermal balance by recording atmospheric opacity and surface albedo [3]. A surface version of the MILH would record the movement of water vapor, provide a baseline measurement of isotopic ratios, and monitor basic meteorology.

Additional information could be gleaned from various internal sensors, such as detection of inclusions of CO₂ hydrate-clathrates.

Ongoing work: The cryobot approach suffered from two prominent liabilities. First, the cryobot expended large amounts of energy just to compensate for conductive losses in the cold ice of Mars. As a result, it required approximately 500W just to avoid being frozen into the ice, and an average of over 1 kW to achieve the desired descent rate. Second, the meltwater sampling scheme was far from optimal in that the pool of water surrounding the vehicle contained the accumulated solutes of the entire descent.

To remedy these deficiencies, the Subsurface Ice Probe (SIPR) is being tested as a means to perform an "open-hole" descent. The SIPR drill head sits in the bottom of a dry, open hole and melts a small quantity of water at a time, pumping it to the surface for analysis. The tether reel and all analytical instrumentation stay on the surface. By only requiring a small drill-head to be submerged in water, SIPR minimizes thermal losses, and can achieve its mission with less than 100W average power. Second, by returning samples to the surface, SIPR simplifies sidewall imaging (as compared to systems that image through silt-laden water), retains good depth resolution for chemical analysis, and does not require analytical instrumentation to be miniaturized for down-hole use. The only potential drawback to SIPR is the fact that the eventual flow or

failure of the ice limits both the depth and duration of the hole. For planetary exploration, this limitation is of marginal importance. On Mars, in particular, SIPR should penetrate up to a kilometer, more than sufficient to study the polar layered deposits.

References: [1] Zimmerman W. et al (2002), Proc. IEEE Aerospace Conf.[2] K.E. Herkenhoff K.E. and Plaut J.J. (2000), Icarus 144, 243–253[3] Smith P. and Lemmon M. (1999) JGR 104, 8975–8986.

STRATIGRAPHY AND STRUCTURE OF THE SOUTH POLAR LAYERED DEPOSITS ON MARS. K. E. Herkenhoff, L. A. Soderblom and R. L. Kirk, U. S. Geological Survey Astrogeology Team, 2255 N. Gemini Dr., Flagstaff, AZ 86001 (kherkenhoff@usgs.gov).

Introduction: The martian polar layered deposits (PLD) are probably the best source of information about the recent climate history of Mars [1-7], but their origin and the mechanisms of accumulation are still a mystery [8]. The polar layers are sedimentary deposits that most planetary scientists believe are composed of water ice and varying amounts of wind-blown dust [2-4], but their composition is poorly constrained [9]. Because climate changes are likely recorded as variations in composition or deposition/erosion rates between layers, the detailed stratigraphy of the PLD is of great interest. Layer thicknesses of ~10 to 50 m were observed in Viking Orbiter images of the north PLD by Blasius *et al.* [10], and Mars Orbiter Camera (MOC) images resolve layers with similar or lesser thicknesses in both polar regions [11]. In order to accurately determine the thickness of layers and interpret PLD stratigraphy and structure, the topography of exposures must be known. Previous studies have identified deformation in the PLD similar to that observed in terrestrial glaciers [12-14], but lack of detailed topography has hindered structural interpretations. Here we describe results of our continuing study to evaluate the topography, structure, and stratigraphy of the south PLD using photoclinometry on MOC images.

Approach: Because the south PLD surface is typically rough (Fig. 1), we used a 2-dimensional photometric technique [15] constrained using simultaneously-acquired MOLA data. This technique is well suited to images taken at high latitudes when the surface was covered by seasonal frost and the solar elevation angle was low so that albedo variations and their effects are minimized and topographic modulation is emphasized (Fig. 1). The high density of MOLA data in the polar regions allows gridded topographic products to be generated at higher spatial resolution (~250 m/pixel) than is possible at lower latitudes. We introduce MOLA topography into the process in five ways [16]: 1) for planimetric control; 2) to precisely model surface and atmospheric reflectance/scattering; 3) to account for subtle variations in surface albedo; 4) as the starting solution for the photometric model; 5) as the DEM base map on which the MOC NA high-resolution DEMs are mosaicked. A sample of the results of this approach is shown in Figure 2.

Results: The photometric models show evidence for folding and faulting of the PLD. Figure 2 shows what appear to be folded beds between relatively planar layers. The planar layers are in some places truncated by the folded layers, either from

above or below. These relations suggest that the folds are not simply the result of compression of the entire stack of PLD, although the layers at the bottom of the exposure in Figure 2 may have been folded in this way.

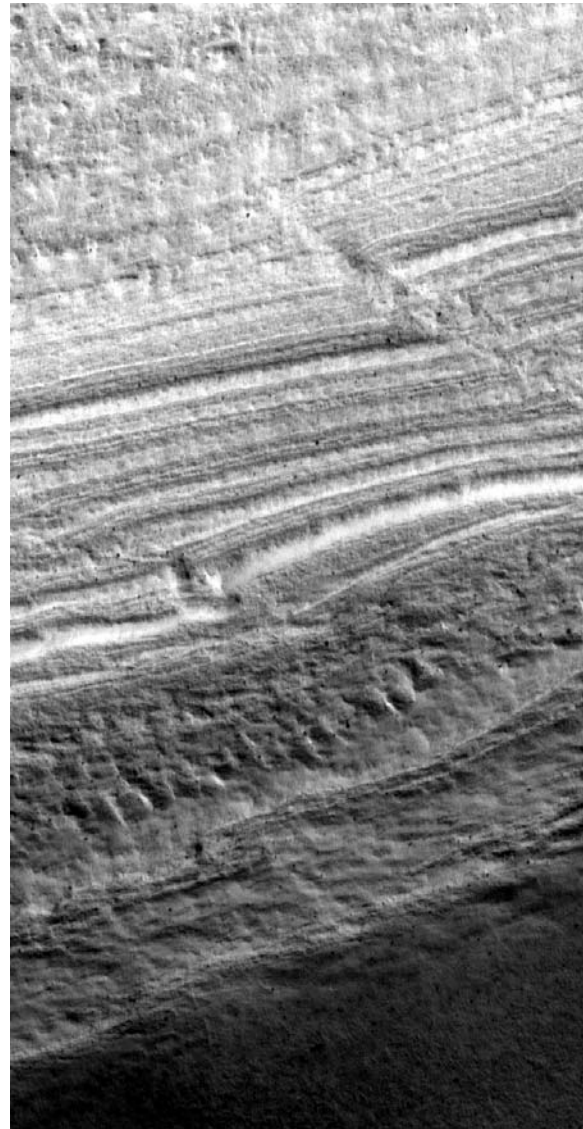


Figure 1. Part of MOC image m0402455 of apparent reverse faults in south PLD. Illumination from bottom left, 2.8 m/pixel.

For the wavy structures near the top of the section, deformation by faulting and/or flow is implied. If the folding was caused by ductile or fluid flow, erosion of the planar beds is required to produce the observed

terminations. The flow process may have caused erosion of the adjacent layers, for example. The feature near the top of the section shown in Figure 2 is consistent with viscous flow down the current topographic slope. Alternatively, the truncations may have been caused by faulting along non-planar surfaces. For example, the wavy structure just above the green plane in Figure 1 may be a fault zone, formed by low-angle normal displacement with the slip vector trending approximately parallel to the present topographic gradient. Analysis of photoclinometric models of other PLD exposures will be discussed at the conference.

References: [1] Murray, B. C., *et al.* (1972). *Icarus* **17**, 328-345. [2] Cutts, J. A., *et al.* (1979). *J. Geophys. Res.* **84**, 2975-2994. [3] Squyres, S. W. (1979). *Icarus* **40**, 244-261. [4] Toon, O. B., *et al.* (1980). *Icarus* **44**, 552-607. [5] Carr, M. H. (1982).

Icarus **50**, 129-139. [6] Howard, A. D., *et al.* (1982). *Icarus* **50**, 161-215. [7] Plaut, J. J., *et al.* (1988). *Icarus* **76**, 357-377. [8] Thomas, P., *et al.* (1992). In *Mars*, University of Arizona Press, Tucson, pp. 767-795. [9] Clifford, S. M. *et al.* (2000). *Icarus* **144**, 210-242. [10] Blasius, K. R., *et al.* (1982). *Icarus* **50**, 140-160. [11] M. C. Malin and Edgett, K. S. (2001). *J. Geophys. Res.* **106**, 23,429-23,570. [12] Kargel, J. S. (2001). *Eos, Trans. AGU.*, **82**, F724. [13] Brightwell, S. N., *et al.* (2003). *LPS XXXIV*, Abstract #2077. [14] Murray, B. C., *et al.* (2002). *Icarus* **154**, 80-97. [15] Kirk, R. L., *et al.* (2003). ISPRS Working Group IV/9 Workshop "Advances in Planetary Mapping 2003", Houston. [16] Soderblom, L. A. and Kirk, R. L. (2003). *LPS XXXIV*, Abstract #1730.

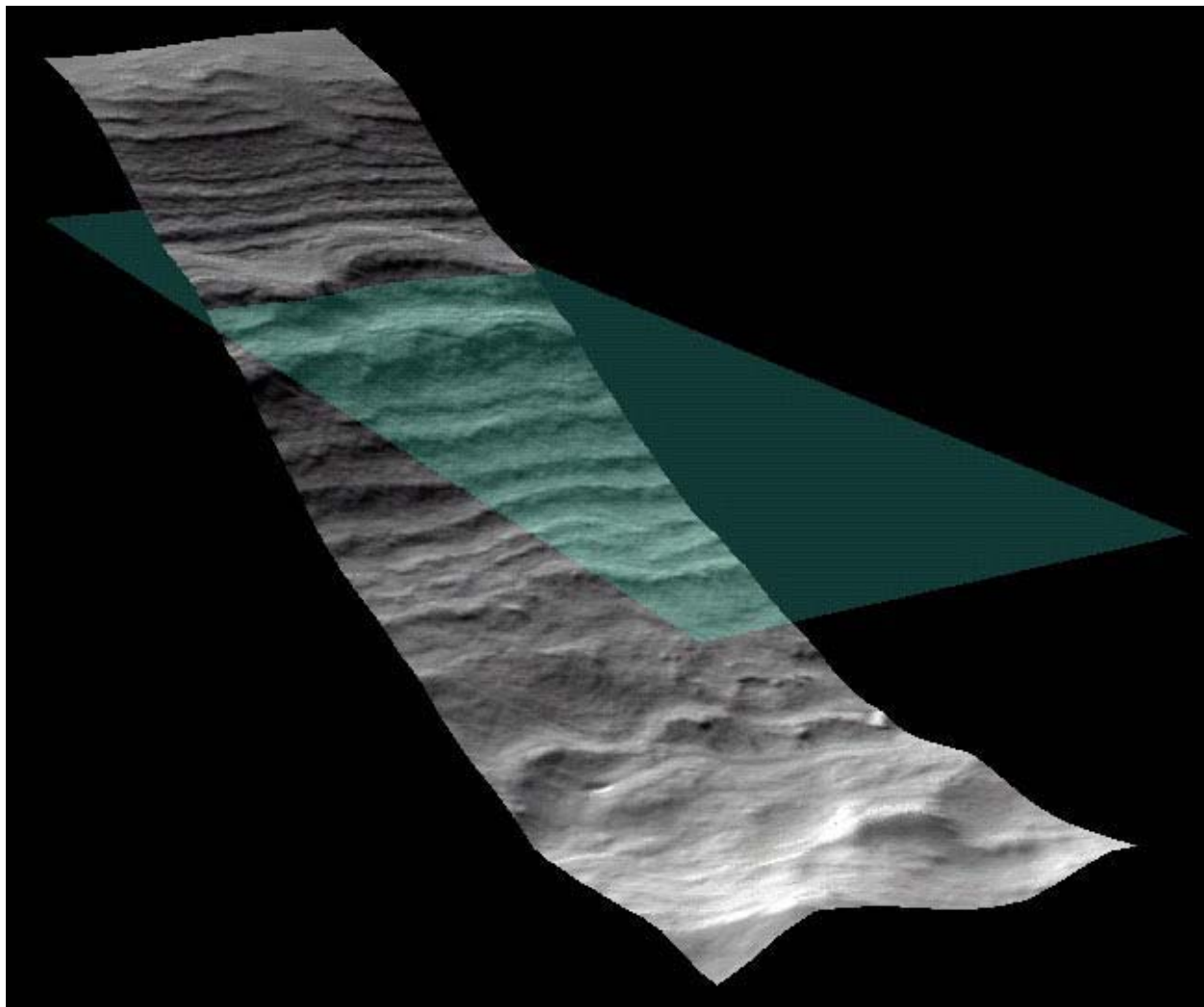


Figure 2. Oblique view of digital elevation model derived from MOC narrow angle image m0905983 (2.7 m/pixel) of south polar layered deposits. Green plane is horizontal reference surface. Note that bedding is not everywhere horizontal, perhaps due to faulting or flow of originally flat-lying layers.

THE MARS IMAGER FOR CLOUD AND AEROSOL (MICA). V. J. Hipkin¹, J. R. Drummond¹, J. Hackett², R. Deschambault², J. Abbatt¹, G. Besla¹, C. T. McElroy¹, S. M. L. Melo¹, K. Strong¹, J. J. Caldwell³, J. C. McConnell³, D. V. Michelangeli³, P. Bernath⁴, J. Sloan⁴, W. Ward⁵ and B. Tolton⁶. ¹University of Toronto, Toronto, Ontario, ²COMDEV Ltd, Cambridge, Ontario, ³York University, Toronto, Ontario, ⁴University of Waterloo, Waterloo, Ontario, ⁵University of New Brunswick, Fredericton, New Brunswick, ⁶Synodon Ltd, Edmonton, Alberta

Introduction: Cloud and dust play an important role in the Mars polar atmosphere. Of particular interest is the evolution of cap-edge dust storms observed during the Mars Global Surveyor mission [1] and the development of the polar hood.

This poster describes the Mars Imager for Cloud and Aerosol (MICA), a four-band visible camera designed to characterize Mars cloud and dust by imaging the limb at sunrise and sunset. It will be capable of producing profiles of Mars aerosol optical properties from 0-75km with a vertical resolution better than 600m. MICA will follow on from Mars Express and MRO cloud and aerosol vertical profile mapping, providing new information, higher vertical resolution and adding to the Mars cloud and dust climatology.

MICA instrument design: Two-band twilight limb images from Viking were analyzed by Jaquin et al [2] and used to produce detailed aerosol extinction profiles. The power of this technique lies in the strong scattering response of small particles to visible light, and in viewing this signal against the dark limb. It allows very thin particle layers to be observed with high signal to noise.

The MICA design uses multiple bands and a new occulting disk technique to provide enhanced dust characterization capabilities. The full dynamic range of the camera is optimized for scattered light. A pin-hole in the occulting disk attenuates direct sunlight, reducing its intensity to levels produced by scattering. The resulting composite image contains both a detailed image of the sun and a sensitive wide-angle image of the distribution of thin cloud and aerosol layers (Figure 1). Absolute calibration is possible through viewing the sun at high angle above the atmosphere. The calibrated solar image produces particle extinction measurements directly, while the wide-angle part of the image can be used to fit the scattering phase function in the case of horizontally homogeneous layers. These measurements will provide significant new constraints on Mars aerosol particle size distribution and optical properties.

Proposed mission: This instrument has been proposed as part of the Mars Volcanic Emission and Life (MARVEL) Scout. In the MARVEL mission proposal, MICA's visible observations are complemented by additional aerosol composition information from a

bore-sighted high-resolution FTIR instrument. These combined observations produce an extremely powerful data set for the study of Mars dust and cloud latitudinal, seasonal and vertical variability and micro-physical processes. The addition of a flip mirror gives MICA the capability to observe the surface.

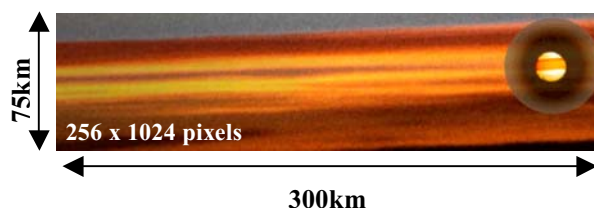


Figure 1: A simulated MICA sunset limb image showing cloud and dust layers. The shadow around the sun is the occulting disk penumbra.

References:

- [1] Cantor, B. A. et al (2001) *JGR*, 106
- [2] Jaquin et al (1986) *Icarus*, 68

Acknowledgments: This work was supported by the Canadian Space Agency, CREStech and COM DEV LTD.

Further information: Contact Dr. Vicky Hipkin, Dept of Physics, University of Toronto, 60 St. George St, Toronto, Ontario, Canada, M5R 2W3. **Email:** vicky@atmosph.physics.utoronto.ca

ACCURACY OF MARS' POLAR AXIS DETERMINATION BY EARTH-BASED RSDI.

I. V. Holin, Space research institute, Moscow, holin@mail.cnt.ru

Introduction: Radar Speckle Displacement Interferometry (RSDI) is a new Earth-based radar technique to measure instantaneous spin components of inner planets with unprecedented accuracy [1-4]. To avoid mixing with known techniques (VLBI, RORI) note that RSDI is based on the effect of far coherence (speckle displacement) [3-5]. The only right comments on RSDI known to the author until now were given in [6].

RSDI instruments: The heart of RSDI as applied to Radar astronomy needs (Radio astronomy needs are not discussed in this work) is a radar transmitter. At present the only in the world fully steerable and powerful enough radar is the 70m ~450 KW Goldstone transmitting facility in South California, USA. Radar echoes scattered from planetary surfaces can be received by a radio interferometer consisting of two (or more) radio telescopes all over the world, e.g. two-element interferometers are 70m Goldstone – 100m Green Bank, West Virginia (transAmerica ~ 3000 km baseline), 100m Green Bank – 70m Madrid, Spain or 100m Green Bank – 100m Effelsberg, Germany (transAtlantic ~ 6000-7000 km baselines), 100m Goldstone – 70m Kashima, Japan (transPacific ~ 7000 km baseline) and so on.

Limiting accuracy: The limiting RSDI accuracy in instantaneous polar axis orientation of Mars can be written as [7]

$$\sigma = 1 / qb \sim 1 \text{ arcsec} \quad (1)$$

where $b \sim 3000$ km is the baselength (Goldstone – Green Bank), $l \sim 3$ km is the correlation radius of scattered radar field (size of a speckle), $q = Q^{0.5}$, Q – power signal-to-additive noise ratio (snr) at the correlator output. Eq. (1) presents one-look (measuring time about 1 min) accuracy in instantaneous obliquity or precession angle that can not be overcome by Earth-based monochromatic radar.

Experiments: First RSDI experiment was proposed about Venus in 1992 [7]. Another RSDI experiment on Mercury was analysed in very details in 1999 [8]. Only in May-June 2002 after extensive discussions with S. J. Peale (nobody in Russia except the author believed in success) the first reliable RSDI experiment was carried out on Mercury with the Goldstone – Green Bank radar interferometer by Margot et al. [9]. The May-June 2002 experiments clearly confirmed the theoretical analysis [5]. Now we all know that the technique really works. Also we may hope that

a few arcsec final accuracy can be achieved. Most probably RSDI experiments on Mars are upcoming as well. Accuracy on Mars during a single conjunction with Earth can be better than 1 arcsec. Also any variations in Mars' polar axis orientation (nutations) can be measured by the technique. If a new more powerful and more dedicated radar transmitter can be designed and constructed in near future to cover advanced radar astronomy needs in XXI century then after regular observations RSDI accuracy on Mars can be of an order of tens mas (milliarcseconds). We hope future RSDI experiments may help substantially to accelerate extensive theoretical work on creating adequate detailed models of spin dynamics of Mars, Mercury, Venus including all related problems (interiors, dynamics of atmospheres and other).

References: [1] Holin I. V. (2003) *LPS XXXIV*, Abstract # 1109 [2] Holin I. V. (2003) *MetSoc.* 66, Abstract # 5003 [3] Holin I. V. (2003) *Meteoritics & Planet. Sci.* (in revision) [4] Holin I. V. (2002) *Solar System Res.* 36, 206 [5] Holin I. V. (1988) *Radiophys. & Quantum Electron.* 31, 515 [6] Peale S. J. et al. (2002) *Meteoritics & Planet. Sci.* 37, 1269 [7] Holin I. V. (1992) *Radiophys. & Quantum Electron.* 35, 433 [8] Holin I. V. (1999) *Uspekhi Sovr. Radioelektron.*, No. 7, 16 (in russian) [9] Margot J.-L. (2002-2003) private communications.

ECHO SOURCE DISCRIMINATION IN AIRBORNE RADAR SOUNDING DATA FOR MARS ANALOG STUDIES, DRY VALLEYS, ANTARCTICA. J. W. Holt¹, D. D. Blankenship¹, M. E. Peters¹, S. D. Kempf¹, D. L. Morse and B. J. Williams¹, ¹University of Texas Institute for Geophysics, The John A. and Katherine G. Jackson School of Geosciences, University of Texas, 4412 Spicewood Springs Rd., Bldg. 600, Austin, TX 78759, jack@ig.utexas.edu

Introduction: The recent identification of features on Mars exhibiting morphologies consistent with ice/rock mixtures, near-surface ice bodies and near-surface liquid water [1,2], and the importance of such features to the search for water on Mars, highlights the need for appropriate terrestrial analogs in order to prepare for upcoming radar missions targeting these and other water-related features. Climatic, hydrological, and geological conditions in the McMurdo Dry Valleys of Antarctica are analogous in many ways to those on Mars, and a number of ice-related features in the Dry Valleys may have direct morphologic and compositional counterparts on Mars.

We have collected roughly 1,000 line-km of airborne radar data over permafrost, subsurface ice bodies, rock/ice glaciers, ice-covered saline lakes, and glacial deposits in Taylor and Beacon Valleys. These data are being analyzed in order to develop general radar propagation models of features with direct relevance to Mars.

A crucial first step in the data analysis process is the discrimination of echo sources in the radar data. The goal is to identify all returns from the surface of surrounding topography in order to positively identify subsurface echoes. This process will also be critical for radar data that will be collected in areas of Mars exhibiting significant topography, so that subsurface echoes are identified unambiguously.

Data Acquisition Methods: Using a Twin Otter airborne platform, data were collected in three sepa-

rate flights during the austral summers of 1999-2000 and 2001-2002 using multiple systems, including a chirped 52.5 – 67.5 MHz coherent radar operating at 750 W and 8 kW peak power (with multiple receivers) and 1 - 2 microsecond pulse width, and a 60 MHz pulsed, incoherent radar operating at 8 kW peak power with 60 ns and 250 ns pulse width. The chirped, coherent data are suitable for the implementation of advanced pulse compression algorithms and SAR focusing.

A laser altimeter (fixed relative to the aircraft frame) was also used during both seasons. Post-processing of the positioning data yields accuracies of ~ 0.10 m for samples at ~ 15 m intervals. Precise positioning was accomplished through the use of two carrier-phase GPS receivers on the aircraft and two at McMurdo Station.

Surface and shallow subsurface properties are being supplied by glacial geomorphologists conducting ground-based studies in Taylor and Beacon Valleys.

Data Acquisition Targets: Flight paths for the Dry Valleys flights in late 2001 are shown in Figure 1. Flights in early 2000 achieved approximately the same coverage, excluding Beacon Valley (due to weather). Flight elevation was nominally 500 m above the surface. Radar and laser altimetry data were collected over the following targets relevant to Mars:

Taylor Glacier: The entire length of Taylor Glacier was surveyed. These profiles extend from Taylor Dome on the polar plateau to the terminus in Taylor Valley

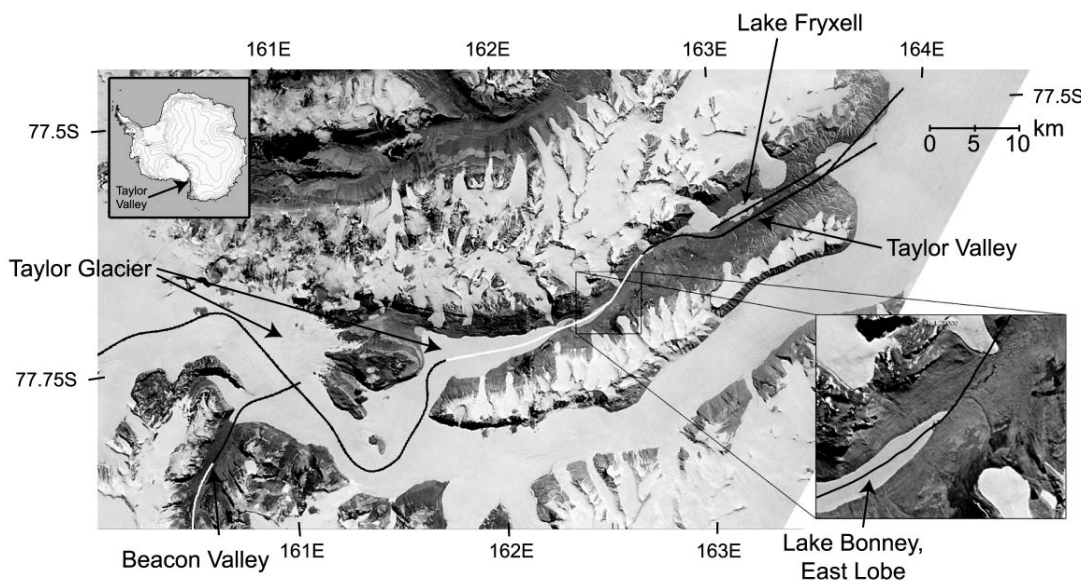


Figure 1. Optical satellite photo of Taylor Valley (center) and Beacon Valley (lower left) within the McMurdo Dry Valleys of Antarctica. UTIG airborne radar profiles (from 2001) are indicated by the solid

black and white alternating lines.

where it is characterized by a high-angle, ice-cored thrust moraine [3]; this profile also includes a lobe that penetrates Beacon Valley. Possible subsurface reflectors in the preliminary data near the terminus appear to be a root of the ice-cored thrust moraine.

Friedman Rock Glacier, upper Beacon Valley:

This glacier is 1-2 km wide by 3-4 km long, is heavily debris-covered and is slow moving (max 40 mm/a) [4]. Preliminary data show possible basal reflectors below the glacier where we overflew it.

Debris flows, Taylor Valley: East of Lake Bonney (Fig. 1), a debris flow emanating from the northern wall of Taylor Valley is hypothesized to have occurred in a subaqueous environment [3]. This flow is fairly well defined in the preliminary data (Fig. 2).

Ancient subsurface ice body, central Beacon Valley: This body is covered by < 1m of glacial drift and hypothesized to be ~ 8 Ma [5].

Permafrost and active layers: In lower Taylor Valley, the Bonney drift includes reworked lake deposits and hummocks thought to be dessicated thrust moraines [3]. Polygonal terrain that we overflew in Beacon Valley is underlain by ice bodies and ice-cemented soil [6].

Lakes Fryxell and Bonney, Taylor Valley: We collected data over both of these ice-covered saline lakes. Permafrost underlies Lake Fryxell [7] and probably Lake Bonney, so we expect a shallow perched water table near the lakes. The reflector underlying the debris flow adjacent to Lake Bonney appears to merge with the lake (Fig. 2).

Data Analysis: The first stage of analysis is the discrimination of subsurface echoes from surface echoes due to surrounding topography. Two techniques are being used in parallel for echo discrimination. Surface returns are being simulated using aircraft position data, the modeled radar antenna pattern, and surface topography from a digital elevation model (DEM) recently acquired by the USGS and NASA in the Dry Valleys with 2-meter postings. These will be compared with the actual data to reveal side echoes.

The second method identifies all echoes in the radar data and maps them into possible correlative surface features to the sides of the aircraft through range estimation. This uses the measured time delay of the echo and known surface topography. We map the echoes onto the DEM (and optical imagery) at the appropriate range in order to identify candidate surface return sources. The two methods should identify all echoes that are not from the subsurface. The comparison of different radar configurations and par-

allel tracks where they are available will also be utilized to identify the source of any ambiguous echoes.

Once this stage is completed, forward models of the radar properties of these targets will be developed. These can then be applied in a general sense to similar features on Mars, in the context of future radar missions.

Conclusions: Preliminary results of airborne radar sounding in the Dry Valleys of Antarctica indicate penetration of a debris flow, a rock glacier, and massive subsurface ice bodies. Two methods of echo discrimination are being developed in order to confirm apparent subsurface reflectors: (1) forward modeling of echoes using known properties of the radar, antenna pattern and topography, and (2) mapping of radar echoes to the sides of the aircraft to identify features in the topography that could be echo sources.

Acknowledgements: This work is supported by NASA grant NAG5-12693 and the University of Texas at Austin. Data acquisition was supported by NSF grants OPP-9814816 and OPP-9319379. Thanks to Beata Csatho for access to the Dry Valleys DEM.

References: [1] Malin M. C. and Edgett K. S. (2000) *Science*, 288, 2330-2335. [2] Baker V.R. (2001) *Nature*, 412, 228-236. [3] Higgins S. M., Denton G. H., and Hendy, C. H. (2000) *Geogr. Ann.*, 82A, 365-389. [4] Rignot E. J., Hallet B. and Fountain A. (2002) *JGR*, submitted. [5] Sugden D. E., Marchant D. R., Potter N., Jr., Souchez R. A., Denton G. H., Swisher C. C., and Tison J.-L., (1995) *Nature*, 376, 412-414. [6] Sletten R. (2002), *pers. comm.* [7] Harris H. J. H. and Cartwright K. (1981), *Antarctic Res. Ser.*, 33, 193-214.

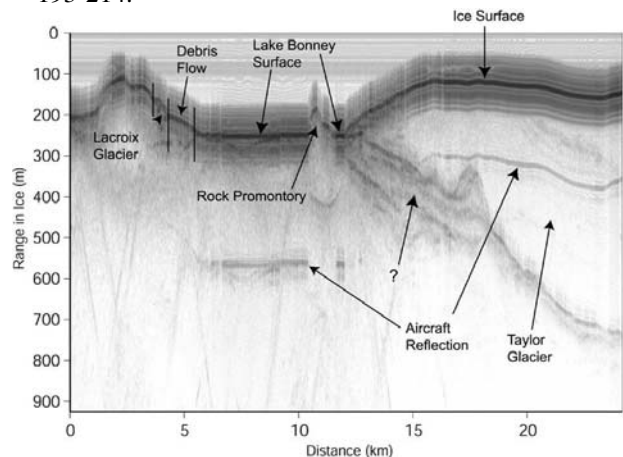


Figure 2. A portion of the radar sounding profile of Taylor Valley (white segment of flight path in center of Figure 1). Up-valley is to the right in this figure. The (?) points to a possible debris-rich layer at the base of Taylor Glacier that may be the source of ice-cored thrust moraines that outcrop at the terminus.

MODELING MARTIAN FOG FORMATION IN THE NORTHERN HIGH LATITUDES DURING THE RETREAT OF THE SEASONAL NORTH POLAR CAP. A. Inada, *Max-Planck-Institut für Aeronomie, Katlenburg-Lindau D37191, Germany (inada@linmpi.mpg.de)*, M. I. Richardson, *Division of Geological and Planetary Sciences, California Institute of Technology, Pasadena, CA, USA (mir@gps.caltech.edu)*, A. D. Toigo, *Center for Radiophysics and Space Research, Cornell University, Ithaca, NY, USA (toigo@astro.cornell.edu)*.

Introduction The early stages of spacecraft exploration of Mars showed that dust plays as important a role in the Martian atmosphere as water vapor does for the Earth. Gierasch and Goody (1972) showed that a model including the radiative effects of suspended dust provided a good fit to the atmospheric temperature structure observed by Mariner 9. The effects of water ice particles in the atmosphere and climate is a more recent concern. The vertical distribution of water vapor varies due to the precipitation of cloud particles (*e.g.*, Kahn 1990; Clancy *et al.*, 1996; Richardson *et al.*, 2002). The radiative effect of cloud particles has been discussed by Colaprete and Toon (2000). Water vapor condenses at high altitudes of about 80 km as a detached haze, at altitudes (depending on the season and latitude) of 10-50 km as clouds, over the polar caps as polar hoods, and near the surface as fogs. The various clouds, hazes, and fogs make up one component of the the water cycle on Mars (Jakosky, 1983; Richardson and Wilson, 2002). For example, as suggested by Kahn (1990) and demonstrated by Richardson *et al.* (2002), clouds in late northern summer are essential for returning water to the surface at a rate consistent with observations. In addition, the condensed phase of atmospheric water may play a significant role in modifying the spatial distribution of dust, through sequestration, as well as affecting surface temperatures and the atmospheric temperature structure.

Ice particle motions and radiative effects depend on particle size. Additionally, the particle size is sensitive to the manner in which the water ice particle was nucleated (homogeneous or heterogeneous nucleation). This important parameter has been estimated using Mie theory to fit observed infrared spectral data (Curran *et al.*, 1973), using one-dimensional haze models to fit Viking limb images (Kahn, 1990), and most recently, using multi-angle thermal and visible observations (R. T. Clancy, private communication, 2003).

These data, combined with morphological information from images (Wang and Ingersoll, 2002), provide important constraints on microphysical models, which seek to provide more detailed insight into the dynamic nature of clouds, hazes, and fogs. One of the earliest explicit models of cloud formation was that of Michelangeli *et al.* (1993), who used the method developed by Toon *et al.* (1988) in a one-dimensional Martian climate model. Recently microphysical processes codes have been included in the Geophysical Fluid Dynamics Laboratory (GFDL) Mars General Circulation Model (GCM) (Rodin *et al.*, 2001) and the NASA Ames Mars GCM (Colaprete and Haberle, 2001).

Most previous work modeling atmospheric ice aerosols has focused on clouds. Near-surface water ice particles (“fogs”) have been less widely discussed. The boundary layer model of Savijärvi (1995) was used to model fog formation. It



Figure 1: Fog in canyons seen by Viking Orbiter.

showed thin fog formation at the Viking Lander 1 site (22.5° N, 48.0° W). Fogs at the Pathfinder landing site (19.2° N, 33.2° W) and in the Memnonia region (15.0° S, 145.0° W) were simulated with microphysical processes by Inada (2002). Both are one-dimensional models and the simulated locations are in the low-middle latitudes. Fogs imaged by the Viking Orbiter, Mars Global Surveyor, and Mars Odyssey cameras have been observed to form in craters and channels, which motivates the simulation of fogs with models that explicitly treat three-dimensional atmospheric flow in response to high-resolution topographic information. Additionally, the abundance of water vapor sublimated from the northern polar cap leads to a large mixing ratio in high latitudes, and indicates that this may be a place of common fog formation. The purpose of this work is to investigate fog formation in the northern high latitudes during the retreating phase of the seasonal cap.

Observations It is generally difficult to identify optically thin clouds and fogs in images taken from orbiters; however, some of these images show brightening in craters, channels, and other depressions (Figure 1). This indicates that the bright feature is related to the surface topography, and is most likely ice aerosol formed near the surface, which can be called fogs. The optical depth of a typical crater fog observed in an orbiter images taken near the Viking Lander 1 site measured by Hoekzema (personal communication, 2003) was 0.92 in the red and 0.93 in violet, while that over the clear surface was about 0.55.

The Mars Atmospheric Water Detector (MAWD) on the Viking Orbiters provided a dataset of the column water vapor abundance that was the primary source of information on the water cycle for many years (Farmer *et al.*, 1977; Jakosky and Farmer, 1982). Recently, spectra from the Thermal Emission Spectrometer (TES) on Mars Global Surveyor (MGS)

MESOSCALE MODELING OF MARTIAN FOG FORMATION: Inada *et al.*

have been used to determine the annual variation of column-integrated water vapor (Smith, 2002). Both observations show the peak of water vapor amount in the northern high latitudes after the seasonal cap retreat. The maximum column density is over the edge of the northern polar cap in early-to-mid-summer and is more than 75 precipitable microns (pr. μm). This water vapor is contributed to a polar atmosphere which is quite cool, and thus the northern summer pole becomes one of the very few places on Mars when the atmosphere is nearly saturated (Richardson *et al.*, 2002). The vapor distribution (the mass mixing ratio) is likely to decrease with height from the surface; elsewhere on the planet, it is likely uniformly distributed with height to at least 10 km. The northern polar atmosphere is thus a likely place for water recondense in the atmosphere due to the diurnal temperature cycle.

Model The simulation of fogs in the polar region is implemented with the Mars MM5 described by Toigo and Richardson (2002). This model is based on the Pennsylvania State University (PSU)/National Center for Atmosphere Research (NCAR) Mesoscale Model Version 5 (MM5) (Dudhia, 1993) and converted for use on Mars. It has been developed to research atmospheric dynamics on scales of a few hundreds meters to a few hundreds of kilometers, so that it is the most suitable model to study fog formation. The surface topography is taken from MGS Mars Orbiter Laser Altimeter (MOLA) high-resolution data set. Boundary conditions are provided by the GFDL Mars GCM (Richardson and Wilson, 2002)

For this study, we add the fog model of Inada (2002) to the Mars MM5. This enables the mesoscale atmospheric model to better simulate the water ice cycle. The microphysical processes of nucleation, condensation, sublimation and sedimentation are included. Coagulation due to sedimentation will be added in the future. Brownian coagulation is negligible because it affects only small particles with r less than $0.01 \mu\text{m}$, where r is particle radius. The nucleation rate is a function of the radius of nuclei particles, with nucleation on large dust particles being faster than that on small particles. All dust particles are assumed to act as nuclei. Since there are typically many large dust particles near the surface, little nucleation occurs on particles with $r < 1.0 \mu\text{m}$.

Outlook Fog formation in the northern high latitudes is driven by the retreat of the northern seasonal polar cap. We will present the diurnal time sequence of fog formation, the size distribution of fog particles, water ice amount and the optical depth. The radii of formed ice particles depends on the pre-existing dust particles which are active as nuclei. Since water ice particles are segregated to the surface during the formation phase of the seasonal cap, large dust particles which act nucleation cores of water ice particles are removed from the atmosphere. The seasonal variance of dust size distribution is also simulated. Finally we compare the simulated fogs with observations from the Viking Orbiters cameras, the Mars Orbiter Camera (MOC) and TES on MGS, and the Mars Odyssey THEMIS.

References

Colaprete, A., and R. M. Haberle, A comparison of Mars GCM cloud simulations with observations, American Geophysical Union, Fall Meeting 2001, abstract P31A-0534

- Curran R. J., B. J. Conrath, R. A. Hanel, V. G. Kunde, and J. C. Pearl, Mars: Mariner 9 spectroscopic evidence for H_2O ice clouds, 1973
- Dudhia, J., A nonhydrostatic version of the Penn State-NCAR mesoscale model: Validation tests and simulation of an Atlantic cyclone and cold front, *Mon. Weather Rev.*, 121, 1493–1513, 1993
- Farmer, C. B., D. W. Davies, A. L. Holland, D. D. LaPorte, and P. E. Doms, Mars: Water vapor observations from the Viking Orbiters, *J. Geophysics, Res.*, 82, 4225–4248, 1977
- Inada, A., Numerical simulations of Martian fog formation and inflight calibration of Mars Imaging Camera on NOZOMI for its future observations, Doctoral Thesis, Kobe Univ., Kobe, 2002
- Jakosky, B. M., and C. B. Farmer, The seasonal and global behavior of water vapor in the Mars atmosphere: Complete global results of the Viking atmospheric water detector experiment, *J. Geophys. Res.*, 87, 2999–3019, 1982
- Jakosky, B., The role of seasonal reservoirs in the Mars water cycle—II. Coupled models of the regolith, the polar caps, and the atmospheric transport, *Icarus*, 55, 10–39, 1983
- Kahn, R., Ice haze, snow, and the Mars water cycle, *J. Geophys. Res.*, 95, 14677–14693, 1990
- Michelangeli, D. V., O. B. Toon, R. M. Haberle, and J. B. Pollack, Numerical simulations of the formation and evolution of water ice clouds in the Martian atmosphere, *Icarus*, 100, 261–285, 1993
- Richardson, M. I., and R. J. Wilson, Investigation of the nature and stability of the Martian seasonal water cycle with a general circulation model, *J. Geophys. Res.*, 107(E5), doi:10.1029/2001JE001536, 2002
- Richardson, M. I., R. J. Wilson, and A. V. Rodin, Water ice clouds in the Martian atmosphere: General Circulation Model experiments with a simple clouds scheme, *J. Geophys. Res.*, 107(E9), doi:10.1029/2001JE001804, 2002
- Rodin, A. V., R. J. Wilson, and M. I. Richardson, GCM simulations of the current Martian water cycle: Clouds and dynamical leverage *Bull. Am. Astro. Soc.*, 33(3), abstract 27.04, 2001
- Savijärvi, H., Mars boundary layer modeling: Diurnal moisture cycle and soil properties at the Viking Lander 1 Site, *Icarus*, 117, 120–127, 1995
- Smith, M. D., The annual cycle of water vapor on Mars as observed by the Thermal Emission Spectrometer, *J. Geophys. Res.*, 107(E11), doi:10.1029/2001JE001522, 2002
- Toigo, A. D. and M. I. Richardson, A mesoscale model for the Martian atmosphere, *J. Geophys. Res.*, 107(E7), doi:10.1029/2000JE001489, 2002
- Toon O. B., R. P. Turco, D. Westphal, R. Malone, and M. S. Liu, A multidimensional model for aerosols: Description of computational analogs, *J. Atmos. Sci.*, 45, 2123–2143, 1988
- Wilson, R. J. and K. P. Hamilton, Comprehensive model simulation of thermal tides in the Martian atmosphere, *J. Atmos. Sci.*, 53, 1290–1326, 1996

ANALYSIS OF PROPERTIES OF THE NORTH AND SOUTH POLAR LAYERED DEPOSITS. A. B. Ivanov¹, S. Byrne², M. I. Richardson², A. R. Vasavada³, T. N. Titus⁴, J. F. Bell⁵, T. H. McConnochie⁵, P. R. Christensen⁶, THEMIS Science Team, ¹*Jet Propulsion Laboratory, MS168-416, Pasadena, CA, 91106; e-mail : anton.ivanov@jpl.nasa.gov*, ²*California Institute of Technology, Division of Geological and Planetary Sciences, Pasadena, CA*, ³*University of California, Los Angeles, CA*, ⁴*U.S. Geological Survey, 2255 North Gemini Drive, Flagstaff, AZ*, ⁵*Cornell University, Department of Astronomy, Ithaca, NY*, ⁶*Arizona State University, Tempe, AZ*.

1 Introduction

One of the many questions of Martian exploration is to uncover the history of Mars, through analysis of the polar layered deposits (PLD). Martian polar ice caps hold most of the exposed water ice on the surface of Mars and yet their history and physical processes involved in their formation are unclear. We will attempt to contribute to our knowledge of the composition and stratigraphy of the PLD.

In this work we present the latest imaging data acquired by the Mars Odyssey THERMAL EMISSION IMAGING SYSTEM (THEMIS) [1] and place it into context of the Mars Global Surveyor (MGS) data. We have discussed the North Polar data in [5]. This work concentrates on data acquired over the South pole of Mars and compares properties of North and South PLD.

We are primarily interested in properties of the layers in both ice caps : their continuity, morphology and stratigraphy. These questions can be addressed by THEMIS VIS color images, along with MOC high resolution data and MOLA Digital Elevation Models (DEM). We will investigate thermophysical properties of the layered deposits employing THEMIS IR images. Based on the data obtained by the orbiting spacecraft and described here, we will attempt to expose major directions for modeling and further understanding of the physical processes involved in the formation of the polar layered terrain

2 Available data

2.1 THEMIS VIS

The THEMIS Visible Imaging Subsystem (VIS) is a 5-color, 1024x1024 interline transfer CCD camera that acquires high spatial resolution 18 to 72 m/pixel multispectral images (425 to 860 nm) from Mars orbit ([1, 6]). In order to gain coverage some images are downsampled to a resolution of 36m/pixel. This averaging mode was primarily employed to obtain full coverage of the South Polar Layered Deposits (SPLD) during early spring, when this area is still covered by seasonal frost. A fragment of THEMIS VIS mosaic is shown in Figure 1. This fragment shows a part of residual south polar ice cap between 270E and 320E. Layers are clearly seen in this figure. Since this area is all covered by seasonal frost at this time, brightness variations in this image are primarily due to changes in topography. The staircase structure of the layered deposits is clearly seen. Layers in the North PLD are much smoother and don't exhibit staircase structure. Figure 2 shows a THEMIS 36m/pix image and a MOC high-resolution image of a scarp in the SPLD. Layers are clearly visible in both THEMIS VIS and MOC images. Continuity of the layers can be easily analyzed from the one band THEMIS VIS mosaic, while color images can be taken in selected areas. MOC high-resolution images

taken along the trough provide excellent high-resolution morphology.

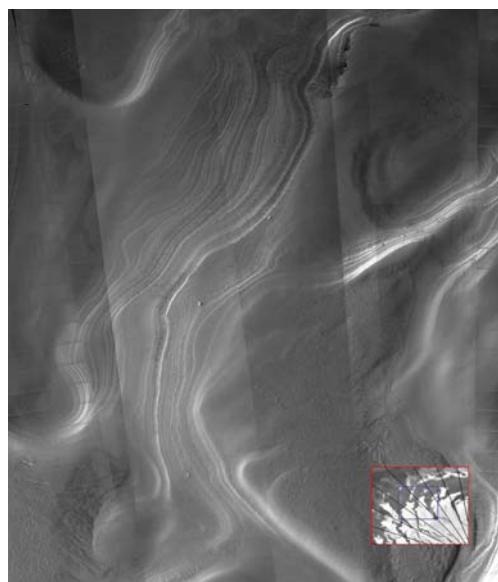


Figure 1: A fragment of THEMIS VIS mosaic of SPLD. The original image resolution is 36 m/pixel. Location of this fragment is shown in the lower right corner on top of the MOC image mosaic. Images were taken in early spring, while ground is still covered by CO_2 frost. Existence of frost on the ground is confirmed by the THEMIS IR data. Context image is shown in the lower-right corner (inside the blue box).

The high quality of the THEMIS VIS data and the high data rate available to download the images will allow us to complete mosaic of the SPLD. We plan to re-image this area during southern summer, when all the seasonal frost will be gone.

2.2 THEMIS IR

The THEMIS IR camera has 10 bands from 6 to 15 μm [1]. Due to signal-to-noise restrictions the most useful band for polar observations is band 9 (12.57 μm). Band 10 (14.88 μm) data can be used for atmospheric calibration. High resolution THEMIS IR data allows us to distinguish bulk properties of layered terrain and ice [5]. We were not able to distinguish between individual layers, however bulk thermophysical properties are under investigation.

2.3 Mars Global Surveyor data

Very interesting details of the polar layered deposits become evident in high resolution MOC Narrow Angle images [4].

POLAR LAYERED DEPOSITS: RESULTS FROM THE THEMIS INVESTIGATION

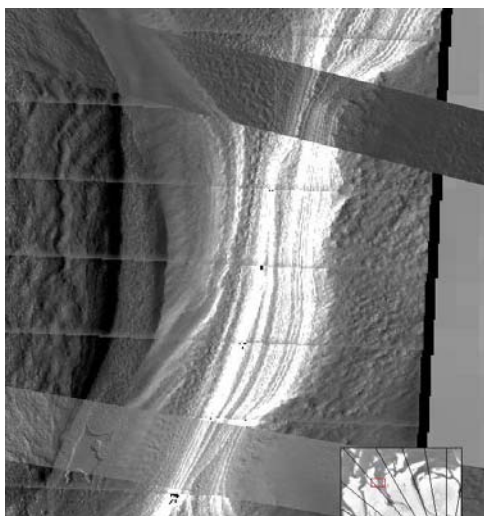


Figure 2: Mosaic of THEMIS VIS and two MOC NA images of a scarp in the SPLD. Images were taken during early southern spring with sun geometry is approximately the same for both MOC and THEMIS images. MOC NA images provide great morphological detail of the layers, while THEMIS VIS images allow to extrapolate this information over much larger areas of SPLD. Context area is shown in the lower-right corner of the figure. Pronounced stripes in the THEMIS image are due to scattered light from adjacent filter in the THEMIS camera.

These images are invaluable for interpreting details of the layered deposits observed with THEMIS. Narrow Angle MOC and THEMIS VIS images are ideal complements for each other. An example of a MOC images mosaicked with THEMIS VIS is shown in Figure 2.

3 Discussion

Large spatial and relatively high-resolution coverage provided by the THEMIS visible camera can resolve individual layers in the NPLD over long distances [5]. Higher resolution MOC narrow angle data can be used to characterize these individual layers. Comparing the trace of these layers to topographic data generated by the Mars Orbiter Laser Altimeter (MOLA) yields information in three dimensions about the position of the layer exposure. Strikes and dips of individual layers can be extracted allowing us to predict if this same layer will be exposed in troughs elsewhere in the layered deposits. Testing large-scale continuity of layers in this fashion may help us distinguish between a flowing or non-flowing ice cap. In addition the possibility of extracting a low-resolution version of the topography underlying the icecap from the three dimensional shape of many layers also exists.

The surface appearance of the layered deposits is distinctly different between the two poles [4]. However MOLA data [2] suggests that the general form of the ice caps is roughly the same and they are both composed of water ice mixed with dust [1]. A possible explanation for this difference lies in the

timescale of the processes responsible for the formation of the layered deposits. Short-time scale processes are currently eroding the surface of the SPLD, while long-term (compared to obliquity cycle) formation processes are still the same for both caps. We will attempt to probe the internal structure of the cap by collecting vertical positions of selected layers in North and South PLDs.

We have successfully demonstrated the use of THEMIS VIS and MOC data in [5]. We were able to trace a marker bed through a trough and locate the same layer in other troughs.

4 Summary

In this work we present a description of the properties of the South Polar Layered Deposits and compare them with their North counterparts. We employ all available datasets, concentrating on data from Mars Odyssey's THEMIS investigation. Our ultimate goal is to characterize major properties of the polar layered terrains and suggest mechanisms and timescales for their formation. Our approach is to use THEMIS VIS images to investigate continuity of the layers in the layered deposits and their stratigraphic relationships using high-resolution MOLA topography. MOC images will provide important morphological detail. We will also attempt to detect heating or cooling trends in THEMIS Thermal IR imagery for selected troughs in the PLD and interpret these data in terms of thermophysical properties (e.g. thermal inertia) of the layers. The MGS TES atmospheric dataset will provide context and will be important for calibration of THEMIS data.

References

- [1] P. R. Christensen, and the THEMIS Science Team. Morphology and Composition of the Surface of Mars: Mars Odyssey THEMIS Results. *Science*, 300(5628):2056–2061, 2003.
- [2] D. E. Smith, M. T. Zuber, and et al. Mars Orbiter Laser Altimeter: Experiment summary after the first year of global mapping of Mars. *JGR*, 106:23689–23722, October 2001.
- [3] M. D. Smith, and et al. TES results: Mars atmospheric thermal structure and aerosol distribution. *JGR*, 106:23929–23946, October 2001.
- [4] M. C. Malin and K. S. Edgett. MGS MOC: Interplanetary cruise through primary mission. *JGR*, 106:23429–23570, October 2001.
- [5] A. B. Ivanov, and the Themis Science Team. Analysis of properties of the north polar layered deposits. In *Mars6 Conference Abstracts*, July 2003
- [6] J. F. Bell, and the Themis Science Team. High Spatial Resolution Visible Color Units on Mars from the Mars Odyssey THEMIS/VIS Instrument. In *LPSC Conference Abstracts*, March 2003

PROSPECTING FOR MARTIAN ICE FROM ORBIT. L. C. Kanner¹, M. S. Bell², and C. C. Allen³, ¹Carleton College (300 N. College Street, Northfield, MN 55057), ²Lockheed Martin @ Johnson Space Center (2400 NASA Rd. 1, Mail Code C23, Houston, TX 77058, mary.sue.bell1@jsc.nasa.gov), ³NASA @ Johnson Space Center (Mail Code ST, Houston, TX 77058)

Introduction: Recent data from the Gamma-Ray Spectrometer (GRS) on Mars Odyssey indicate the presence of a hydrogen-rich layer tens of centimeters thick in high latitudes on Mars [1]. This hydrogen-rich layer correlates to previously determined regions of ice stability. It has been suggested that the subsurface hydrogen is ice and constitutes 35 +/- 15% by weight near the north and south polar regions [2]. This study constrains the location of subsurface ice deposits on the scale of kilometers or smaller by combining GRS data with surface features indicative of subsurface ice.

The most recognizable terrestrial geomorphic indicators of subsurface ice, formed in permafrost and periglacial environments, include thermokarst pits, pingos, pseudocraters and patterned ground. Patterned ground features have geometric forms such as circles, polygons, stripes and nets. This study focuses on the polygonal form of patterned ground, selected for its discernable shape and subsurface implications. Polygonal features are typically demarcated by troughs, beneath which grow vertical ice-wedges. Ice-wedges form in thermal contraction cracks in ice-rich soil and grow with annual freezing and thawing events repeated over tens of years. Ice wedges exist below the depth of seasonal freeze-thaw [3]. Terrestrial ice wedges can be several meters deep and polygons can be tens of meters apart [4, 5, 6], and, on rare occasions, up to 1 km [7]. The crack spacing of terrestrial polygons is typically 3 to 10 times the crack depth [8].

Polygonal terrain is the dominant form of patterned ground seen on Mars [9] and has been recognized in several high resolution Viking Orbiter images [10,11,12,13] and Viking Lander 2 images [14]. High-resolution images from Mars Orbital Camera (MOC) on Mars Global Surveyor reveal Martian surface features in unprecedented detail and meter-sized polygons are more easily discernible and characterized [15]. Martian polygons range in size from 10 m [16] to 10 km [14] or on rare occasions up to 20 km [11]. Polygonal terrain is generally grouped based on size and theorized origin into small-scale (~10-250 m) and large-scale (~250 m-20 km) polygons. Small-scale polygons are applicable to this study because it is thought that the origin of small-scale polygons on Mars is the result of permafrost thermal contraction cracking similar to that found on Earth [17,16]. The presence of polygonal ground on the surface generally indicates the presence of ground ice at depths of sev-

eral meters and can reveal much about the latitudinal distribution of ground ice and ground ice history [17]. Large, multi-kilometer scale polygons likely form by processes unrelated to subsurface ice.

Methods: Using high-resolution narrow-angle MOC images (1.55-12.39 m/pixel), we have noted the presence, absence, and possibility of polygonal terrain around the planet in a latitude band from 30°N to 65°N. Data sets from August 1997-July 2002 were used, less the September 1999-February 2000 set. Polygonal terrain identified in this study can be characterized by the following features: diameter of individual polygons range in size from 25 m - 250 m, polygons are bounded by nearly straight troughs or raised rims and angular joins. Troughs and raised rims frequently show a preferred north-south orientation.

The distribution of polygonal terrain was compared to a mercator projection of GRS relative hydrogen abundance [1,2] as well as a recent geologic map of Mars [18].

Observations: A total of 5,280 images were analyzed and 283 images revealed the presence of polygonal terrain. The distribution of polygonal terrain is scattered throughout the regional band at low elevations (<0m) and nearly all latitudes. The distribution is similar to that found by Seibert and Kargel (2001) [16]. Polygons were identified neither below 35°N nor in the cratered highlands. Particularly high concentrations of polygonal ground are present in the Casius quadrangle between 278°W-258°W and 40°N-50°N. In this region of the Utopia Planitia basin, 74% of the total 132 images analyzed showed the presence of polygonal terrain.

GRS detects hydrogen in high concentrations poleward of 50 +/- 5° [1,2]. The comparison of GRS hydrogen abundance data to the distribution of polygonal terrain shows no correlation (Figure 1). Polygons are present in areas of low concentrations of near subsurface ice as frequently as they are present in areas of high concentrations of near subsurface ice. The high concentration of polygonal ground in western Utopia Planitia correlates to an area of lower concentrations of near subsurface ice.

The majority of polygonal terrain in Utopia Planitia correlates to Hesperian-age units, while there are some occurrences to Amazonian-age units [18]. According to Greeley and Guest, these units, Hesperian and Ama-

zonian, are of diverse origin – volcanic, tectonic, alluvial, and eolian.

Discussion and Interpretation: What can the anti-correlation between near subsurface ice and presence of polygonal terrain in the Casius quadrangle between 282°W-262°W and 40°N-50°N suggest about the composition of the near and deeper subsurface? One possibility is that the presence of this type of polygonal terrain on Mars is not a response to thermal contraction cracking of ice-rich ground. Ice may be absent at depths of several meters, in turn making the polygonal terrain a response to other contraction processes---desiccation, fracturing of cooling lava, deep-seated horizontal stresses, or stratigraphic control.

On the other hand, ice may exist and do so both as near subsurface ice in the first meter as detected by GRS and as deeper ground ice as seen by the presence of ice-wedging terrain. Data collected in this study suggests the existence of near subsurface and deeper subsurface ice layers which can be explained as a response to climate oscillations. It is likely that hydrogen concentrations in the first meter of the Martian surface are a result of climate conditions at present obliquity. Diurnal temperature oscillations affect only the first 2-3 m of the Martian regolith [19]. Ground ice is thought to exist in equatorial regions despite its current instability at the surface [10,20,21]. This conflict can be resolved if deep ground ice is a relic of a colder climate during periods of high obliquity [22]. Theoretical modeling shows that ground ice may have persisted at depths greater than 200 m shortly after the beginning of Mars's geologic history and that ground ice will persist for longer periods of time in regolith of small pore size [23].

If the abundance of Martian small-scale polygons are geomorphically, and structurally similar to terrestrial polygons, their presence should not correlate to hydrogen abundance in the first meter for the following reasons: initial propagation of ice wedges occurs below the freeze-thaw layer, or the ice would melt (or sublime), and ice-wedges can extend tens of meters deep. Martian ice-wedge polygons may correlate to thicker layers of ground ice not detected by GRS.

Acknowledgements: We thank William C. Feldman and William V. Boynton for allowing us to use the GRS data and Buck Janes for sending it. Jan Bednarski has provided numerous aerial photos and interpretation of Canadian, as well as Martian, permafrost features.

References: [1] Feldman W. C. et al. (2002) *Science*, 297, 75-78. [2] Boynton W. V. et al. (2002) *Science*, 297, 81-85. [3] Williams P. J. and Smith M. W. (1989) *The Frozen Earth: Fundamentals of Geocryology*, p23. [4] Lachenbruch A. H. (1962) *GSA*

Spec. Pap., 70, 69p. [5] Kerfoot D. E. (1972) *Arctic*, 25, 142-150. [6] Pewe T. L. (1973) *Geoforum*, 15, 15-26. [7] Pratt W. E. (1958) *AAPG Bulletin*, 40, 2249-2251. [8] Mellon M. T. (1997) *LPS XXVIII*, Abstract #1495. [9] Squyres A. B. et al. (1992) *Mars*, p549. [10] Carr A. B. and Schaber C. D. (1977) *JGR*, 82, 4039-4054. [11] Morris E. C. and Underwood J. R. (1978) *Rep. Planet. Geol. Prog, NASA TM 79729*, 97-99. [12] Evans N. and Rossbacher L. A. (1980) *Rep. Planet. Geol. Prog., NASA TM 82385*, 376-378. [13] Brook G. A. (1982) *Rep. Planet. Geol. Prog., NASA TM 85127*, 265-267. [14] Mutch T. A. et al. (1977) *JGR*, 82, 4452-4467. [15] Malin M. C. et al. (June, July 2003) *Malin Space Center Systems Mars Orbiter Camera Image Gallery* (http://www.msss.com/moc_gallery/). [16] Seibert N. M. and Kargel J. S. (2001) *GRL*, 28, 899-902. [17] Mellon M. T. (1997) *JGR*, 102, 25,617-25,628. [18] Greeley R. and Guest J. E. (1987) *USGS Misc. Inv. Series Map I-1802-B*. [19] Clifford S. M. (2003) *personal contact*. [20] Moughins-Mark P. (1979) *JGR*, 84, 8011-8022. [21] Allen C. C. (1997) *JGR*, 84, 8048-8059. [22] Mellon M. T. and Jackosky B. J. (1993) *JGR*, 98, 3345-3364.

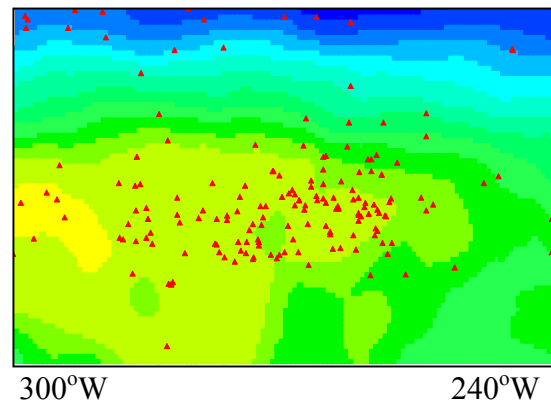


Figure 1. Map of the Casius quadrangle in terms of relative hydrogen abundance (yellow-shaded regions represent areas of low concentrations, blue-shaded regions areas of high [1,2] and distribution of polygonal terrain marked by the red triangles.

ASTER IMAGERY AND INTERPRETATION OF GLACIERS IN JASPER NATIONAL PARK AND ELSEWHERE IN THE CORDILLERA. J.S. Kargel¹ and B. Molnia², ¹U.S. Geological Survey, 2255 N. Gemini Dr., Flagstaff, AZ 86001, U.S.A.; Email: jkargel@usgs.gov; ²USGS, Reston, Email: bmolnia@usgs.gov.

Fourteen-band ASTER imagery has a spatial resolution of 15 m/pixel in VNIR, one band of which is in stereo; 30 m/pixel in SWIR; and 90 m/pixel in TIR. Variable gain settings selectable for snow and ice targets, high radiometric and geometric fidelity, 60-km scene width, special acquisitions of glacier imagery as a part of the GLIMS project (Global Land Ice Measurements from Space, www.glims.org), and high data downlink rate make ASTER ideal for many glacier studies. Spectacular imagery of glaciers in the Cordillera, including some in Jasper Nat. Park, are being used for detailed assessments of glacier morphology, extent, dynamics, hazards, and value as Mars analogs. A large-format poster will present a sample of ASTER imagery for Jasper Nat. Park and other selected areas of the Cordillera in Alaska and British Columbia.

Fig. 1 (above). Glaciers in South-central Alaska. Portion of ASTER image, VNIR RGB, June 27, 2001.

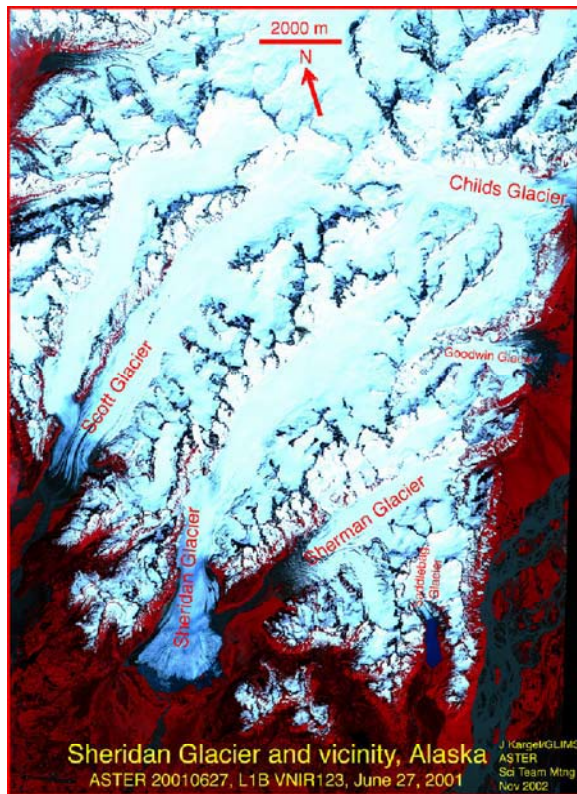
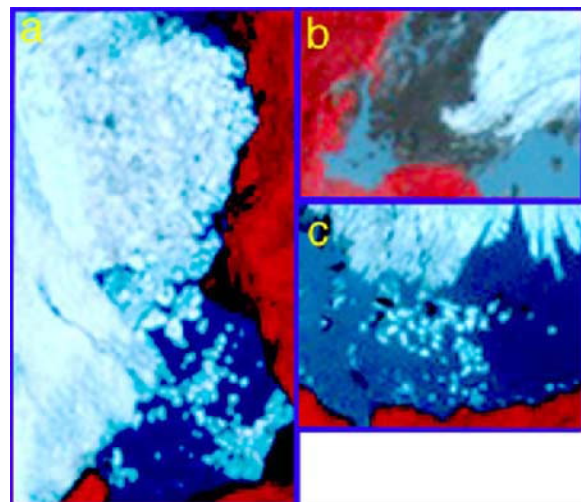
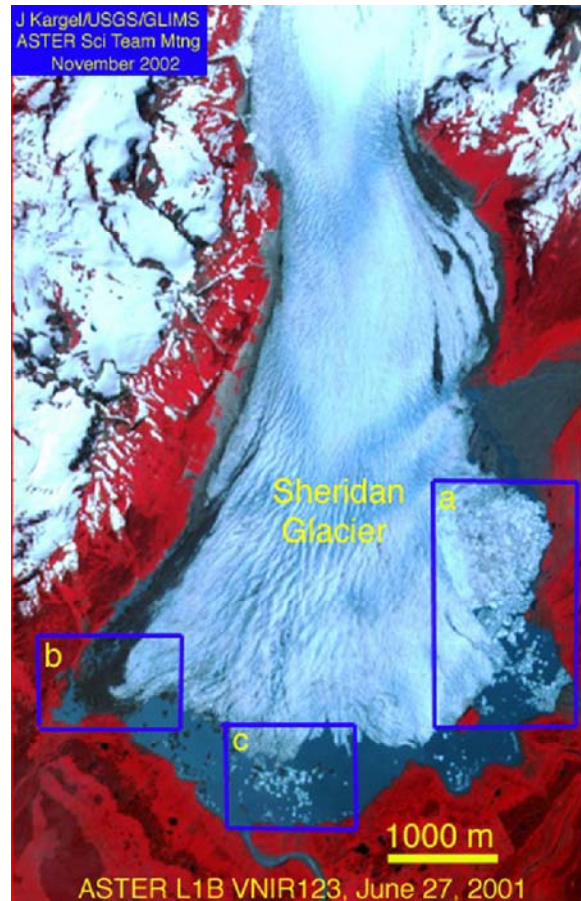
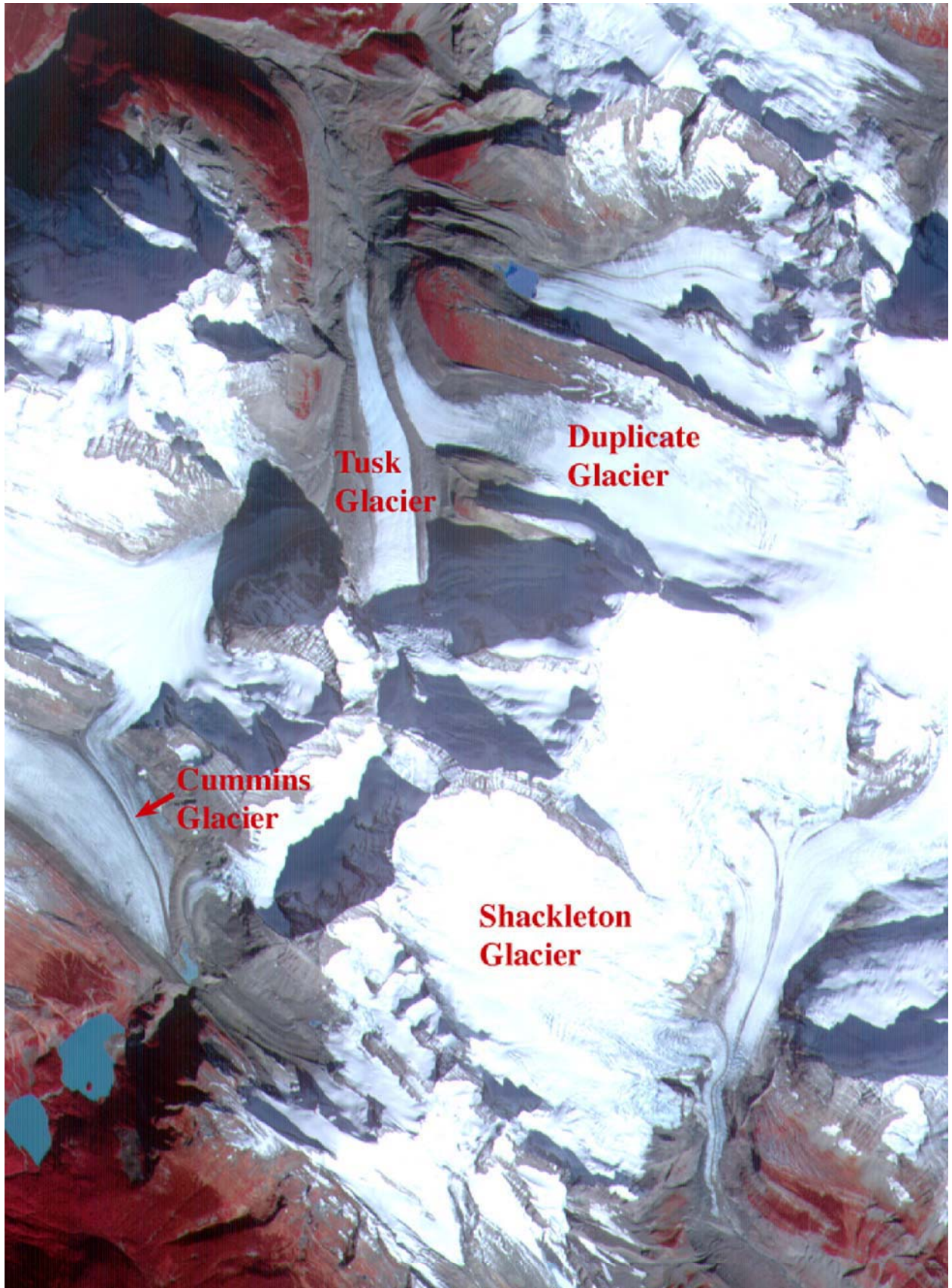


Fig. 3 (next page). Part of the Clemenceau Ice Field, Jasper National Park. Portion of ASTER VNIR R-G-B image July 22, 2002; scene width about 10 km.

Fig. 2. (Below) Sheridan Glacier, SC Alaska, June 27, 2001. Blown up sections of image shown in Fig. 1.





MARTIAN POLAR ICE SHEETS AND MID-LATITUDE DEBRIS-RICH GLACIERS, AND TERRESTRIAL ANALOGS. J.S. Kargel¹, B. Molnia², and K.L. Tanaka³, ¹U.S. Geological Survey, 2255 N. Gemini Dr., Flagstaff, AZ 86001, U.S.A.; Email: jkargel@usgs.gov; ²USGS, Email: bmolnia@usgs.gov; ³USGS, Email: ktanaka@usgs.gov.

Introduction: Glaciers are commonly defined as perennial masses of ice and snow that exhibit morphologic indications of significant flow down-slope under its own weight (under the influence of gravity). This definition does not imply a particular origin or flow mechanism, and in the broadest sense it does not even require that the ice is H₂O. Thus, terrestrial rock glaciers are a type of glacier by this definition, as are Earth's snow-fed alpine glaciers, ice caps, and polar ice sheets; Martian lobate debris aprons, lineated valley deposits of the fretted terrain, and the south polar cap are also glaciers. Martian glaciers apparently include both H₂O-dominated and CO₂-rich icy flows; the ones being rich in CO₂-rich are restricted to the south polar cap. Debris-covered snow-fed glaciers and periglacial rock glaciers provide the closest terrestrial analogs to lobate debris aprons and lineated valley deposits of the fretted terrain.

Martian glacier types and terrestrial analogs: Among Martian glaciers and their Earth analogs, we observe many indications of both brittle and ductile flow behavior. Scarps and troughs in Mars' carbon dioxide-covered south polar cap locally expose intense deformation—buckles, folds, boudins, crevasses, thrust faults and elastic flexural bulges; and in outlying areas of polar layered deposits faults are common. Although there are profound differences between the Martian polar caps and terrestrial polar ice sheets, many of the morphologic characteristics of the Martian south polar cap are similar to characteristics of Earth's ice sheets.

Crevasses, faults, folds, medial moraines, and pressure ridges are commonly expressed on Martian valley and alpine glaciers as deeply etched surface structures whose relief is brought out by differential sublimation. These features are directly comparable to those of terrestrial valley and alpine glaciers. Only one good example comparable to braided glacial outwash systems on Earth has been identified on Mars. Small gullies and debris flows associated with Martian glaciers, like those widely observed for Himalayan debris-covered glaciers, are common. Indications of

sublimation are widespread in precisely the geographic locations where sublimating ice is most expected based on Mars climate models.

Terrestrial glaciers are the closest landform analogs of the Martian glaciers, but some structural features of the Martian icy flows are mimicked by structures best known from high-grade metamorphic and plate tectonic systems on Earth. Terrestrial high-grade metamorphic complexes, where deep crustal spreading of hot plastic layered rocks occurred, offer insights relevant to boudins, folds, and faults in the south polar cap (Figs. 1 and 2). Ductile compressive shortening and the lobate forms of major polar flow lobes (Fig. 3) have good analogs in glacial ice sheets; pahoehoe lava flows exhibit some of the same morphologies. Also in the south polar cap we observe elastic plate flexure, where good process analogs include oceanic plate flexure due to the loads of ocean islands and magmatic arcs. In lobate debris aprons of Deuteronilus Mensae, wrinkle-ridges (similar to those of lunar maria and Martian volcanic plains) and plate obduction (Fig. 4) are observed, but more common are surface buckles, flowlines, and medial moraines (Fig. 5) similar to those of Earth's rock glaciers and debris-covered glaciers.

Conclusions and Implications: The implications of these analogs, along with insights drawn from analytical models, are that (1) the Martian cryospheric flows are composed of a flowing, faulting, folding substance; (2) it is a substance capable both of sublimating and melting at conditions near the Martian surface; and (3) the flow features are generally rheologically layered. This layering in the subpolar glaciers is probably due to differential debris/ice contents as well as vertical thermal stratification. In the south polar cap rheological layering is probably due both to thermal stratification (offering many orders of magnitude variation in effective viscosity) and differential amounts of water ice, dry ice, clathrate hydrate, and minor constituents (salts, acids, and inert dust components).

In contrast with the southern perennial CO₂-surfaced cap, the north polar cap and icy deposits

around the southern perennial cap have only rare ductile behavior, folding, and other evident indications of a soft, glacier-like rheology.

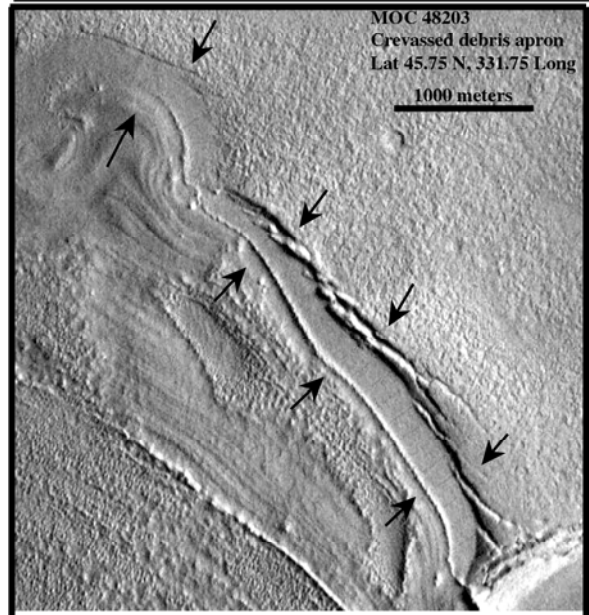
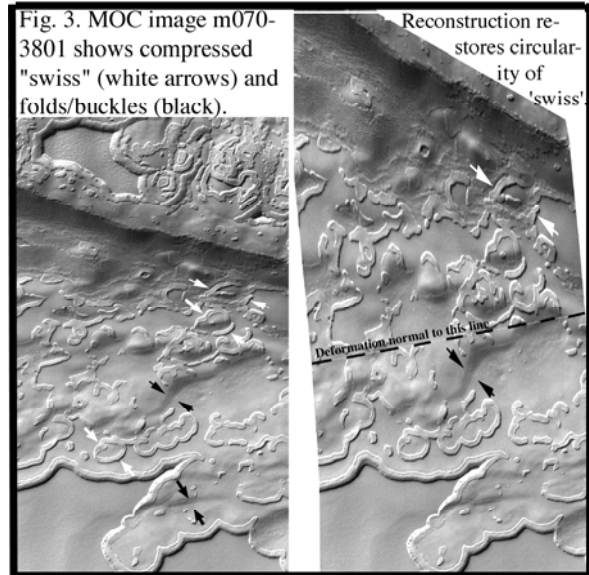
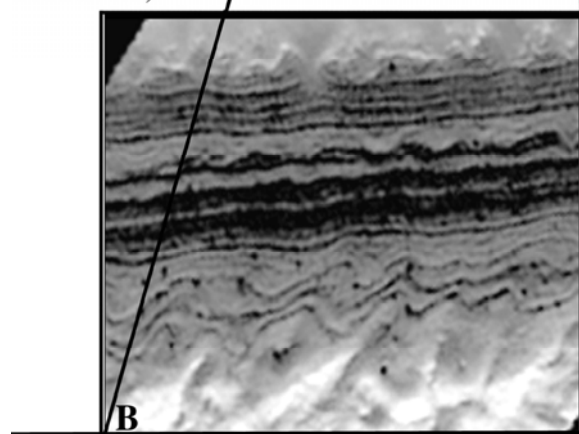
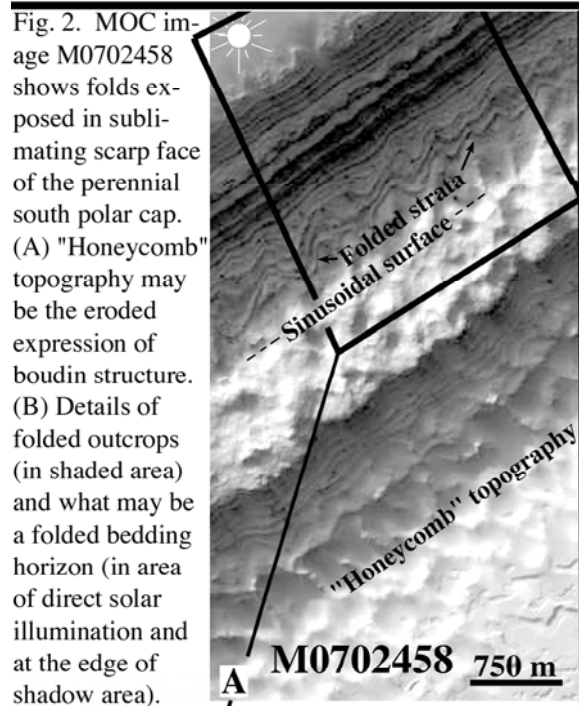
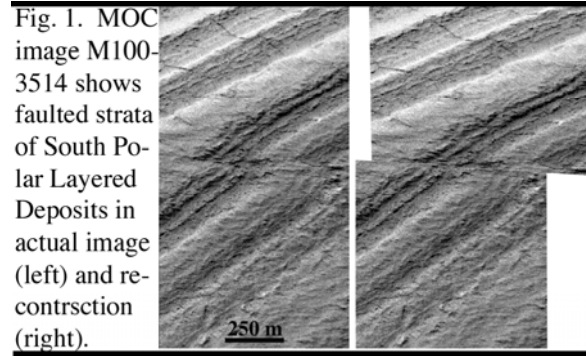


Fig. 4. Mutually obducting lobate debris apron 'plates.'

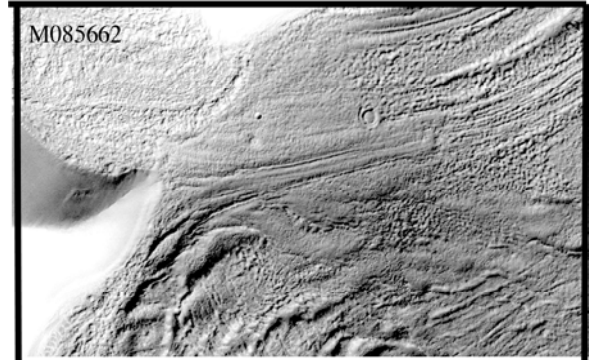


Fig. 5. Medial moraine and flow structure, Coloe Fossae.

RECENT DETECTION OF WINTER POLAR WARMING IN THE MARS UPPER ATMOSPHERE

G. M. Keating, M. E. Theriot, Jr., and R. H. Tolson, *George Washington Univ. Campus at NASA Langley, Hampton, VA 23681 USA* (g.m.keating@larc.nasa.gov), S. W. Bougher, *Univ. of Michigan, Ann Arbor, MI, USA*, F. Forget and M. Angelats i Coll, *Univ. of Paris, Lab. de Meteorologie Dynamique, Paris, France*, and J. M. Forbes, *Univ. of Colorado, Boulder, CO, USA*.

The Mars Global Surveyor (MGS) z-axis accelerometer has obtained over 1600 vertical structures of thermospheric density, temperature, and pressure, ranging from 110 to 170 km, between Sept. 1997 and March 1999, compared to only three previous such vertical structures from Viking 1, 2, and Pathfinder [1]. In November 1997, a regional dust storm in the Southern Hemisphere triggered an unexpectedly large thermospheric response at mid-northern latitudes, increasing the altitude of thermospheric pressure surfaces there by as much as 8 km and indicating a strong global thermospheric response to a regional dust storm [2].

From analysis of the MGS accelerometer data, enormous planetary scale waves have been detected in the Martian thermosphere between 60°N and 60°S. Fourier analysis of the wave structure reveals high amplitude waves 2 and 3 which appear to remain at nearly constant longitude between $\pm 60^\circ$ latitude when viewed near 3 PM [3,4]. However, measurements near 3 AM show evidence of essentially a phase reversal in wave 2 [3]. Taking into account the near sun-synchronous orbit it appears that these waves are principally non-migrating tides propagating to the east. Studies by Wilson et al. [5] and Forbes et al. [6] indicate the wave 2 component observed from MGS is principally an eastward propagating diurnal wave 1 which rotates around Mars in the opposite sense of the sun once per day. The wave 1 Kelvin wave principally results from the interaction of tides and topography. Analysis of Thermal Emission Spectrometer (TES) MGS data near 30 km [5] indicates a similar phase to this wave at 30 km [5], which is in accord with the Kelvin wave, and thus the wave appears to propagate up from below into the thermosphere. The observed wave 3 may be a combination of an eastward propagating, semi-diurnal wave 1 and the eastward propagating, diurnal wave 2 (basically the wave 2 Kelvin wave). Both the observed wave 2 and wave 3 maximize near the equator. These results give further evidence of coupling between the lower and upper atmosphere.

The Mars Odyssey 2001 (M01) Spacecraft was placed into orbit about Mars in September

2001. Aerobraking was performed from then until January 2002 to circularize the M01 orbit. The spacecraft carried triaxial accelerometers, which were used to safely perform aerobraking and to continue exploration of the detailed properties of the upper atmosphere, which had begun with the Mars Global Surveyor accelerometer measurements. The accelerometers were used to measure atmospheric density, and from the vertical structures measured on both inbound and outbound trajectories the scale height, temperature and pressure were determined. Altogether 600 vertical structures were obtained ranging from 95 km to above 170 km. Measurements were obtained for the first time near the North Pole. Also, the first measurements were obtained on the night-side in the Northern Hemisphere. Temperatures near 110 km were discovered to increase with latitude maximizing near the North winter pole, apparently due to dynamical heating [7]. This result is contrary to the MarsGram and MTGCM models used for Odyssey aerobraking, where model temperatures are predicted to minimize near the winter pole. For example, maximum temperatures near the North winter pole at 100 km were observed to be near 200 K while MTGCM temperatures were predicted to be near 100 K. However, an upper atmosphere winter polar warming is predicted by the European Mars GCM [8] at both the North and South Poles in local winter at high altitudes. The altitudinal variations and high latitude diurnal variations of temperature near the North Pole also appear to be in fair accord with the Forget et al. model. Apparently, the upper atmosphere North polar winter warmings may result from adiabatic heating from the subsiding branch of the cross-equatorial meridional circulation from the Southern Hemisphere summer. The only measurements of the Southern Hemisphere winter polar upper atmospheric temperatures were obtained from accelerometers aboard the Mars Global Surveyor. These measurements do not show winter polar warmings, but minimum temperatures near the winter South Pole more in accord with radiative equilibrium, and more in

accord with the MTGCM model. Apparently, the summer-to-winter cell supplying dynamical heating to the North winter pole near perihelion is much stronger than the summer-to-winter cell supplying dynamical heating to the South winter pole near aphelion. The stronger dynamical heating during the North polar winter may result from being near perihelion where the closer sun and stronger dust activity may strengthen the meridional cell.

Previously, intense warming of the winter polar atmosphere was observed in the lower atmosphere (~25km) by the Infrared Thermal Mapper Instrument (IRTM) aboard the Viking orbiters during the onset of the 1977b global dust storm at northern hemisphere winter solstice [9,10].

References

- [1] R. H. Tolson, G. M. Keating, et al. (1999) Application of accelerometer data to Mars Global Surveyor aerobraking operations, J. of Spacecraft and Rockets, 36, No. 3.
- [2] G. M. Keating, et al. (1998) The structure of the upper atmosphere of Mars: In Situ accelerometer measurements from Mars Global Surveyor, Science, 279, 1672.
- [3] G. M. Keating, et al. (2001) Persistent planetary-scale wave-2 and wave-3 density variations observed in Mars upper atmosphere from MGS accelerometer experiment, Proceedings of European Geophysical Society, 78, 229.
- [4] S. W. Bougher, G. M. Keating, et al. (2001) The upper atmosphere wave structure of Mars as determined from Mars Global Surveyor Accelerometer, EOS, Trans. AGU, supplement, page F717.
- [5] R. J. Wilson. (2002) Evidence for nonmigrating thermal tides in the Mars upper atmosphere from the Mars Global Surveyor accelerometer experiment, Geophys Res. Lett., 29, (7), 10.1029 GL013975.
- [6] J. M. Forbes, G. M. Keating, et al. (2002) Nonmigrating tides in the thermosphere of Mars, In Press, J. Geophys. Res., Planets.
- [7] G. M. Keating, et al. (2002) Detection of North Polar winter warming from the Mars Odyssey 2001 accelerometer experiment, Proceedings of the 34th Scientific Assembly of the Committee on Space Research (COSPAR) and the World Space Congress, 142.
- [8] F. Forget, et al. (1999) Improved general circulation models of the Martian atmosphere from the surface to above 80 km, J. Geophys Res., 104, 24155.
- [9] B. M. Jakosky and T.Z. Martin. (1987) Mars: North-polar atmospheric warming during dust storms, Icarus, 72, 528.
- [10] R. J. Wilson. (1997) A general circulation model simulation of the Martian polar warming, Geophys. Res. Lett., 24 (2), 123.

BEHAVIOR OF SOLID CO₂ ON MARS: STILL A ZOO. Hugh H. Kieffer, *U. S. Geological Survey [Emeritus], Flagstaff, AZ 86001, USA, (hkieffer@uneedspeed.net).*

Observations of the martian polar caps by TES, THEMIS and MOC have revealed a variety of peculiar patterns: now informally known as **Cryptic material, Dalmatian spots, spiders, oriented fans and fried eggs**. These result from the characteristics and behavior of solid CO₂ on Mars, which is unlike anything on Earth. The proposed model involves the micro-physical interaction of CO₂ and dust with the solar and thermal radiation fields on Mars. This abstract is a shortened version of that for Mars VI, with no citations.

CO₂ Surface Condensation Modes: The condensation of the predominant gas in an atmosphere by radiative cooling yields the prominent seasonal polar caps on Mars. This process has no terrestrial analogy, which limits our intuition. This process is difficult to impossible to simulate in the laboratory because the natural force that allows condensation at a location other than at the coldest boundary (which sets the radiation balance) is gravitation, involving a characteristic scale many km. A practical laboratory scale would require a warm physical barrier that is completely transparent to thermal radiation.

TES observations in many areas in the polar night indicate that most of the condensation occurs at the Martian surface. TES spectra in the 25 μm region indicate that the “**Cryptic**” regions of cold-dark polar material consist of a CO₂ non-scattering slab composed of indeterminately large grains, or a slab. In other regions, fine-grained frost is found.

For condensation of a nearly pure gas by radiative loss there can be two end-member solutions for the form of the solid. If the abundance of non-condensing gases is negligible, so that a diffusion gradient of the condensing material is not involved, then a thick slab can form. On Mars, the dominant radiative loss of the condensate is from inside the bulk material. Growth perturbations outward from a planar solid interface, such as a crystal spike growing upward, have a longer conductive path to the bulk solid which, in turn, can radiate the latent heat of condensation. Lacking a diffusion gradient at the tip of such a spike, the condensation rate is limited by conductive heat loss, and this tip is at a disadvantage for condensation relative to the bulk solid. Thus perturbations do not grow, and the expected steady state form is a thick slab with a smooth surface. Such slabs are observed to grow in laboratory conditions of pure condensing gases, although the thermal gradient internal to the slab results from conduction to a cold substrate rather than by radiative cooling.

In the presence of some amount of non-condensing gas, e.g., the 5% of N₂ plus Ar on Mars, at the micro-physical level there will be some diffusion gradient of the condensing gas toward the condensation sites. Both the temperature gradient and the concentration gradient of the condensate are expected to be linear for steady state conditions. Because of the nonlinear dependence of saturation pressure upon temperature, the partial pressure will be above the saturation pressure throughout this layer. Under this condition, spikes sticking up into this diffusion gradient become the favored site of condensation and they will grow more rapidly than locations deeper into the diffusion gradient. The steady state solution for the form of such

a growing deposit is long columnar crystals oriented along the diffusion gradient. Such deposits also are observed to form in laboratory conditions of substrate cooling when small amounts of non-condensing gas are introduced into the chamber. This process of growth in a diffusion gradient gives rise to the beautiful H₂O hoar-frost crystals seen on calm terrestrial winter mornings.

TES observations indicate that both the slab growth and deposition of fine-grain CO₂ condensates occur in the polar night and that different condensation processes are dominant in different locations. The reason for the geographic distribution of the Cryptic material is unknown.

Radiation Balance in a Pure Solid CO₂ Slab: During the polar night, the radiative balance of surface CO₂ will be negative (barring an extraordinarily warm atmosphere). With the Sun above the horizon, solar radiation penetrates deeply into pure CO₂. The relative absorption lengths for solar and thermal energy become important.

Using the optical properties of solid carbon dioxide, the penetration of both solar energy and ambient thermal radiation into a slab of CO₂ have been calculated. For typical polar summer conditions (incidence angle of 65°, $U = 1.5$), 2/3 of the solar energy penetrates 1m into pure solid CO₂, whereas thermal flux is reduced to 50% in 3.7 mm. The top 2 mm of the slab are in net radiative loss; below that absorption of insolation results in net heating.

Dirty CO₂ Ice: Mars atmosphere is generally dusty with particles of radius on the order of 2 μm. During the CO₂ condensation season, atmospheric dust grains probably act as condensation nuclei; perhaps first for H₂O and then for CO₂. The proportion of dust in the CO₂ cap has not been measured, but is reasonably assumed to be near the average abundance of dust in the atmosphere. Using an average visual opacity of the atmosphere of 0.5 yields a dust abundance of about 1.5×10^{-3} kg m⁻³ or roughly 2×10^{-5} by mass. Because the particle size is smaller than thermal wavelengths, the presence of embedded dust will make little change to the thermal radiation environment, but will shorten substantially the solar absorption lengths, narrowing or removing entirely the surficial layer with net radiation loss.

Using the above values, and densities of dust grains and solid CO₂ of 2300 and 1600 kg m⁻³, respectively, corresponds to a mean dust grain separation of ~130 μm. If a seasonal cap budget of 1000 kg m⁻² is adopted, the mass of dust in the cap is 0.02 kg m⁻² and the geometric opacity of the dust in the cap is ~1.6. The visual opacity of dust in the slab at sunrise will be roughly the average opacity of the southern atmosphere during the condensation season times the ratio of slab to atmospheric mass, or ~3.3, in agreement with the geometric opacity if the scattering efficiency is taken as 2.0, as expected from Mie theory.

CO₂ Self Cleaning by Entrained Dust Movement: A first approximation is that for a dirty CO₂ slab, all of the solar energy is absorbed by the dust grains. However, because the surrounding CO₂ is isothermal, this radiation absorbed

SOLID CO₂ BEHAVIOR: H. H. Kieffer

by the grains must go into sublimation of solid CO₂. If the local material is impermeable, a high-pressure pocket of gas will form around the grain and local elastic deformation will increase the pressure in the solid CO₂, allowing some heat to be absorbed without sublimation. The warmer grain cannot be in direct contact with the CO₂, but must rest on a microscopic layer of gas at the bottom of its vapor prison. If the local gas bubble does not rupture, there will be a downward migration of the bubble through the solid as vapor re-condenses on the roof of the bubble, the location most distant from the grain and hence coolest, and the grain will "burrow" downward as sublimation continues under the grain. Thus, a sealed finite vertical columnar hole will travel downward with the grain. When the grain reaches the bottom of the impermeable layer, it will be ejected downward. This self-cleaning, self-annealing process will tend to reduce the amount of dust in the ice through the spring. Because the net solar flux is greater toward the top of the slab, the uppermost particles will move most rapidly, resulting in concentration of dust as a descending "curtain" in the slab, leaving clean ice above.

Development of Pathways and Vents: The net positive radiation divergence near the surface of pure CO₂ will tend to seal small holes in the surface layer. Porosity will generally be sealed in a region that grows downward from the surface. Thus, the gas formed by springtime sublimation generally cannot diffuse upward through the CO₂ deposit. The gas resulting from net sublimation below the surface must escape somewhere and will hold open some set of larger holes. Because the gases in these vents will have some entrained dust, they can continue to absorb solar radiation, transfer energy to the vent walls, and remain open and grow. Also, gas under an impermeable CO₂ slab could reach pressures several times the atmospheric surface pressure. The saturation temperature under a 1000 kg m⁻² slab would be 162K, enhancing the ability of venting gas to enlarge the pathways. Because higher velocities are possible and because of the r^2 heat flow versus the r^1 circumference, larger holes/paths will grow at the expense of smaller ones. Gas released beneath the slab must find some path to the open atmosphere. It may travel laterally underneath the slab to vents, cracks, or even to the edge of the seasonal deposit. It is difficult to predict the spacing of such vents, but they collectively must carry the total sublimation gas flux of about 10 kg m⁻² /day. Vent spacing of tens to hundred meters is observed.

As the effective vents are separated by substantially more than the slab thickness, gas velocities will become far greater than required to suspend dust particles, and any sub-slab lateral transport may begin erosion of underlying loose material. Once the velocity exceeds the fluid threshold, erosion will begin.

The sub-slab lateral gas velocity will depend upon the geometry of the flow; increasing toward a vent. Because the soil thermal inertia of the Cryptic region is low, it is likely that the surface material is incohesive and that channelized flow will develop by scouring, beginning near the vents and progressing outward. Although velocities on the order of 10 m/s are required to initiate transport of fine material by saltation, injection of dust released from the CO₂ into the lateral flow may initiate motion and scouring at lower velocities; 2 mm/s

vertical velocity is adequate to maintain atmospheric dust in suspension.

Dark radially converging dendritic patterns are visible in MOC images of some portions of the spring polar cap, these have been termed "spiders" by the MOC team. In this model, these patterns represent channels formed by sub-slab channelized flow of the sublimation gas toward the vents. Increasingly large particles could become entrained closer to the vent.

The velocity in the vents will be approximately $.005X^2$ m/s, where X is the ratio of vent separation to vent diameter. For example, for vents 1 m in diameter spaced by 100 m, the gas velocity would be 50 m/s. When the jets exhaust into the atmosphere and velocities decrease, the coarser entrained material will fall out in the prevailing downwind direction. In this model, the oriented dark fans seen in the MOC images are caused by this process. This is an exotic model that agrees with observations thus far. It predicts that the dark fans will be oriented into the prevailing wind, that they are seasonal and will disappear with, or shortly after, the CO₂ is gone, and that the "spiders" will be found only in the Cryptic region.

Darks vents are generally, but not exclusively, associated with dunes. Vents can progress into dark spots (**Dalmatian spots**) which grow monotonically until they coalesce. Dark halos commonly develop around the Dalmatian spots; these have been termed "fried-eggs" based on their symmetry and proportions. Many MOC images of the seasonal cap in summertime show great variegation of reflectance, interpreted to be incomplete solid CO₂ cover. Sequences of images show the development of evenly-distributed circular dark spots, which may represent the evolution of vents, commonly spaced by order 100 m, that gradually expand to consume the seasonal cap.

This model has been supported by a survey of the location of "spiders" in MOC imaging which shows that they are largely confined to the Cryptic region and their centers generally correlate with the location of fans. Spiders commonly persist as low relief features through the summer.

Most of this story has been developed from observations of the south polar cap. The north and south caps seem to be somewhat different in terms of the abundance of these features; e.g., spiders have not yet been identified in the north.

Summary: Deep in the martian polar night, there is some CO₂ snowfall, but most of the solid CO₂ takes the form of a uniform, continuous, non-scattering slab with embedded dust (and H₂O ice) grains. Following seasonal sunrise, in some areas the ice brightens due to fracture or surficial frosting, but in other areas the slab persists to form the *Cryptic* regions. The solar energy is largely absorbed by the dust grains, which either burrow downward or escape upward, cleaning the CO₂ slab which anneals small holes near its surface. Sunlight then penetrates to the bottom of the slab, warming the soil and subliming ice from the bottom. Widely spaced vents develop that allow the gas to escape. As the sub-slab gas converges toward the vents, it scours the soil surface along ragged channels (*spiders*). Dust entrained in the jetting gas falls out downwind to form *oriented fans*. The vents enlarge to become *Dalmatian spots*, some of which form *fried-egg* halos; these enlarge to consume the seasonal cap. Only the topographic ghosts of the *spiders* persist through the summer.

DETAILED GEOLOGIC ANALYSIS OF PART OF THE SOUTH POLAR LAYERED DEPOSITS, PLANUM AUSTRALE, MARS.
E.J. Kolb¹ and K.L. Tanaka², ¹Arizona State University, Dept. of Geological Sciences, Tempe, AZ 85287, eric.kolb@asu.edu, ²Astrogeology Team, U.S. Geological Survey, 2255 N. Gemini Dr., Flagstaff, AZ 86001, ktanaka@usgs.gov.

Introduction. We have begun geologic mapping of the martian south polar layered deposits (SPLD) as part of a project to map PLD at both poles at 1:1,500,000 scale. In this abstract, we present preliminary geologic mapping results of SPLD exposed in a trough system east of and adjacent to Chasma Australe within Planum Australe (Fig. 1). Our mapping has allowed us to address outstanding SPLD-related issues including: SPLD bedding characterization, relative timing and modes of trough emplacement, and the formation of secondary features such as the north-trending ridged-and-grooved (“wire brush”) terrain and the sinuous, generally east-trending ridges (“snakes”). The major goals of the mapping project consist of: (1) Construction of stratigraphic sections of the PLD, including topographic analysis of prominent layers and layer sequences and investigation of intra- and inter-polar stratigraphic and topographic variations in the PLD and residual ice caps, (2) detection and interpretation of structural deformation in the PLD, (3) description and interpretation of the erosional history of the PLD. Geologic mapping of the PLD is being performed using a GIS-integrated, multi-dataset approach consisting of current and to-be-released data products including MOLA topography, MOC NA images and THEMIS VIS and IR datasets.

Here, we discuss the geology of the SPLD within a broad trough whose floor dips gently from near the center of the SPLD down toward the margin of Planum Australe. This north-trending, radially orientated trough portrays some diverse and enigmatic landforms (within the region of 100 to 270°W, 80 to 87°S). Data coverage of the trough feature includes 114m/pixel MOLA-derived DEM’s and shaded relief maps, 105 mappable MOC NA images and several VIS and IR THEMIS images. We have developed several geologic cross-sections across and along the length of the trough to aid in the characterization of bedding attitude and structure of PLD exposed within the trough.

PLD Sequences. Within the trough, we have identified six distinct, overlapping, mappable sequences of PLD. PLD subdivision is based on the topographic expression (e.g., cliff vs. terrace forming, Fig. 1) of layer sequences. The sequences are bounded by marker beds that are laterally continuous throughout the study area and beyond, extending >150 km along the trough, within both enclosing trough walls, as well as within a trough system east of the mapping area. Marker beds can also be seen extending from PLD exposed within the trough floor into scarps of the adjacent spiral troughs. Individual sequences are 28 to >150 m thick; total thickness of the six sequences is several hundred meters. PLD bedding attitudes and features appear structurally controlled (Fig. 2 and 3), exhibiting syn- and antiformal beds with wavelengths of kilometers to tens of kilometers and maximum bedding dip angles of 1.5°. In Figure 3, large wavelength anti-formal bedding and smaller syn- and antiforms within it control the topographic expression of the PLD sequences.

Morphologic Features. Along the trough floor and on the western trough wall are a series of closely spaced ridges and intervening grooves that are described as “wire brush terrain” by [1]. In some cases, the ridges and grooves occur within single layers, but where there is more relief, they cut across many layers (Figure 1 and 2). Some of the grooves form enclosed, lenticular troughs, whereas other grooves appear to be composed of coalescing pits. Intervening ridges in some cases appear to be capped by narrow ridges of probably relatively resistant material. In one instance, where cliff-forming PLD sequences exposed in the eastern trough wall extend onto areas of the trough floor overprinted with ridges and grooves, the more resistant material forms streamlined outliers orientated parallel to the ridge and groove trend. MOC NA images show large boulder-like mounds in places. Transecting pole-ward regions of the trough are a series of east-trending ridges spaced tens of kilometers apart. They are tens of kilometers long, up to several kilometers wide, and have only several meters of local relief. Some of the ridges exhibit moderate sinuosity. A few ridges can be traced almost continuously across the trough flanks and floor, whereas others appear only within the trough or on trough-enclosing, high-standing SPLD. The ridges are overprinted with the ridge-and-groove features. Where imaged by the MOC NA camera, the ridges commonly exhibit layering only on the ridge’s south-facing side. At several locations (most notably on the flanks of the trough), ridges are composed of undisturbed PLD that are traceable on both sides of the ridge. In all instances where this is seen, MOLA topography indicates a gentle northward apparent dip of the PLD that make up the ridges—in parallel with subjacent PLD sequences. PLD surfaces, including the “wire brush” terrain and bedding terraces, appear in MOC NA images to be marked by small irregular, shallow pits and alcoves. These features give the PLD a rugged appearance at meters to tens of meters length scales.

PLD Sculpturing. Proposed trough and ridge-and-groove formation mechanisms include glacial scouring and/or streaming, sub-ice volcanism, and eolian activity whereas the west-trending ridges may indicate deformation episodes or in-filled fractures composed of relatively more resistant material [1 and ref within]. Problems with the glacial hypothesis for the ridge-and-groove features include: (1) The supposed basal surface which the moving ice would have scoured is actually within PLD that is well above the base of Planum Australe, yet the underlying PLD does not appear deformed; (2) the trough would have been planed smooth by glaciers; instead, the PLD beds appear terraced; and (3) based on terrestrial examples, the supposed ice stream (marked by the location and extent of ridge-and-groove terrain) should have occurred at or near the margins of the ice sheet [2], not the higher, interior areas of the SPLD. Large collapse pits and crevasses within PLD that should be overlying any hypothetical calderas had sub-ice volcanism occurred are not seen.

The PLD appear to be composed of beds alternating in competency, given: (1) the stair-step slope profile of the PLD, and (2) the alignment of the tops and bottoms of well-developed ridge-and-groove features with the tops and bottoms of individual layers (Fig. 2). The variable competency of the PLD beds may be related to degree of induration, ice composition and structure, and/or concentration of dust particles within an icy matrix. Thus we conclude that eolian scouring chiefly formed the PLD topography. The occurrence of ridge-and-groove terrain within the trough may be attributable to enhanced intensity and longevity of down-slope winds that have carved dip slopes of friable material. However, the ridge-and-groove terrain does not seem to be actively developing; instead, fine-scale pitting and scarp retreat appears to be the most recent observed landform development, perhaps due to back wasting and sublimation of surface or near-surface ice. An eolian scouring trough-formation mechanism would indicate that several hundred meters of SPLD material has been removed (Fig. 2). In Figure 3, the east-trending ridge occurs at the presumed crest of an anticline. This association, and that PLD is typically only seen on the south side of the ridges indicates that the ridges are the erosional expression of north-dipping SPLD beds.

Relative Timing. Along the length of the radial trough are transecting and evenly spaced topographic swales that connect with and are of the same dimensions and orientations, as that of adjacent spiral trough features within Planum Australe. Within the radial trough, swale crest elevations are 100’s of meters lower than their counter parts within the spiral troughs. We postulate that the radial trough post-dates initialization of spiral trough formation and that the swales are the remnants of spiral trough features that had previously extended into regions now occupied by the radial trough. If the spiral troughs have formed by ice-flow processes [3], the undisturbed, continuous bedding contacts that extend from the radial trough into the spiral troughs indicate that since commencement of trough formation, ice flow has not occurred. Erosion of the spiral troughs may be facilitated by along-trough winds (as supported by the streamlined morphology of capping SPLD located on the crest of a spiral trough at 250°W, 83°S) or sublimation of equator-facing slopes. However, we see no evidence for the redeposition of layers on pole-facing slopes [4].

Summary. Our investigation of the trough in Planum Australe that contains distinctive ridge-and-groove (“wire brush”) terrain suggests that the PLD:

- (1) Consist of layers of variable competency
- (2) Include distinctive marker beds traceable for >100 km
- (3) Have not been eroded significantly by glacial scour
- (4) Do not show deposition of spiral trough wall material on pole-facing slopes
- (5) Have experienced significant eolian erosion, including the development of the broad radial trough, the ridge-and-groove terrain, and east-trending ridges by down-slope winds on dip slopes in beds of alternating competency
- (6) Radial trough emplacement occurred after spiral trough formation began; their development may include eolian erosion and/or sublimation
- (7) Have undergone slope backwasting to reveal beds of variable erosional resistance
- (8) Most recently have been dominated by pitting and scarp retreat that may be related to localized removal of ice-rich material

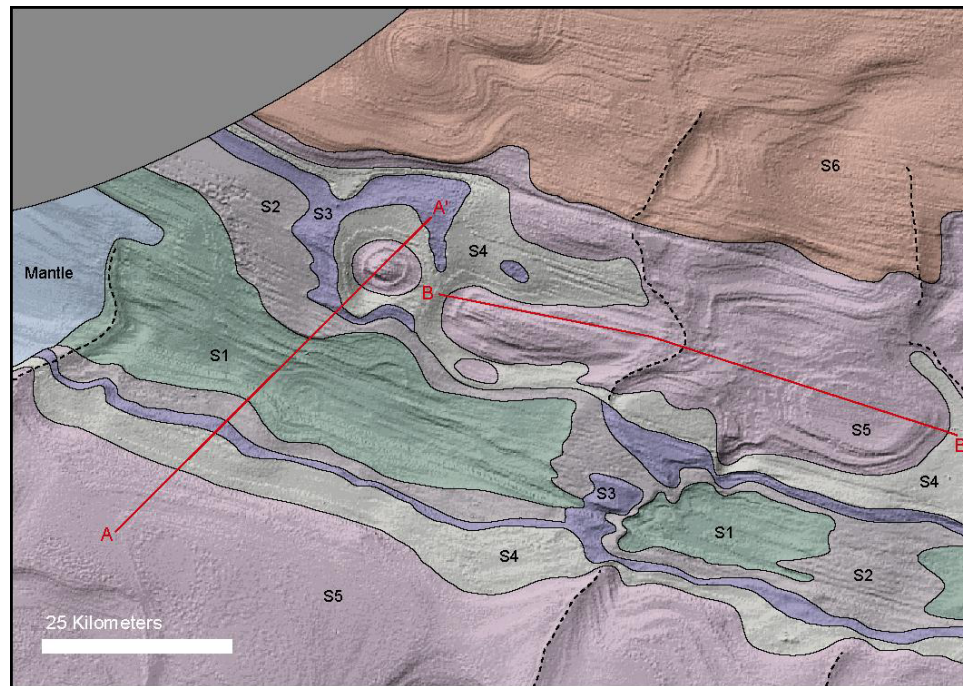


Figure 1. Geologic map of part of the north-trending radial trough east of Chasma Australe. The east-trending ridges are highlighted with a dashed line.

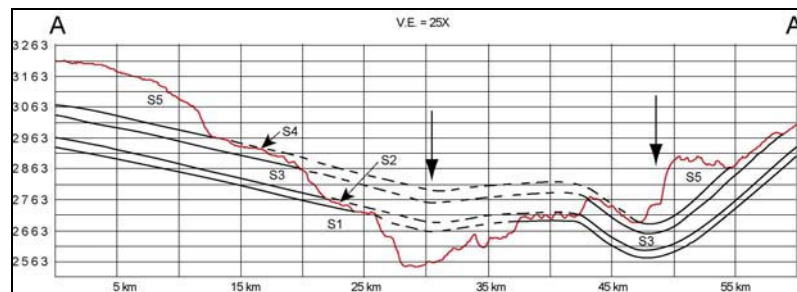


Figure 2. Elevation in meters. Maximum bed dip angle is $\sim 1.5^\circ$. The large arrows highlight the axis location of two north-trending synclines.

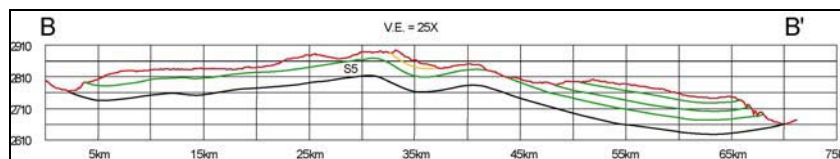


Figure 3. Green lines represent individual layer sequences within Sequence 5 that can be traced along the cross-section. The yellow line is drawn to highlight bedding orientations where the SPLD crosses an east-trending ridge. The PLD descend over 200 m towards the margin of Planum Australe and the average bed dip angle is $\sim 0.5^\circ$.

References: [1] Koutnik M.R. et al., (2003) 6th Intl. Mars Conf. #3134 [2] Hourmark-Nielson, M. et al., (2001) Paleo-Ice Stream International Symposium. Pg. 35 [3] Fisher, D. A. (1993) *Icarus* **34**, 501-511. [4] Howard, A.D. (2000). *Icarus* **144**, 267-288.

INTERCRYSTALLINE SWELLING OF STRATIFIED SILICATES EXPOSED TO NEGATIVE TEMPERATURES.

I.A. Komarov Department of Geocryology, Faculty of Geology, Moscow State University, Vorob'evy Hills, Moscow, 119899, Russia. ilya_komarov@mail.ru

ABSTRACT: Theoretical calculations based on a thermodynamic model together with experimental results based on differential scanning calorimetry are used to test whether intercrystalline swelling occurs in montmorillonite under negative temperatures.

Introduction

The analysis of adsorption properties of expandable stratified silicates, exposed to positive temperatures, provides the basis of proposing the existence of intercrystalline swelling caused by the interaction of silicates with water or other polarizing liquids. Swelling produces characteristic peaks (figure 1) on curves relating differential heat adsorption Q_v and moisture W when observing isotherms for the sorption of water vapor by montmorillonite and vermiculite clays. In particular, the heat of adsorption Q_w for askangel drops as a result of saturation with water. Two maxima on the $Q_w=F(W)$ curve at $W \approx 10\%$ and $W \approx 23\%$ are associated with the intrusion of water between silicate layers of askangel. Minimums on the $Q_w=F(W)$ curve are associated with loss of heat due to expansion of the mineral skeleton during adsorption [5]. Similar maxima and minima are observing for ogranlin and pigew Na-montmorillonite, kovdor vermiculite, and Ca montmorillonite. It is proposed, therefore, that intercrystalline swelling could also take place at negative temperatures, because of presence of unfrozen water near sediment and rock surfaces. Signs of swelling at negative temperatures should be evident from differential thermal analyses (DTA) of temperature curves and heat capacities because water between silicate layers could liberate heat. I examine this problem theoretically using thermodynamic equations for a range of temperature and moisture conditions.

Observation

1.1. Thermodynamic model.

Proposed swelling of stratified silicates at negative temperatures is based on the calculations developed from a model of phase and adsorption equilibrium for water in unsalted and salted frost rocks proposed by Komarov (2001). The basis for this model is that pore liquids are part of a multi-component solution. This point of view is obvious for salted rocks. For unsalted rocks H_2O can occur in a solid, liquid or gaseous phase. A wide range of experimental data derived by various authors using various techniques (e.g. nuclear magnetic resonance (NMR), X-ray, calorimetric) show that unfrozen water is structurally and energetically non-homogeneous [2]. It is proposed, therefore, that water act as a binary solution even without presence of soluble ions in the liquid. Furthermore, I propose that individual H_2O molecules do not associate with the surface of rock particles. Instead water molecules next to the rock surface occur as monomers, which are 5th-8th layers of single water molecules with a thickness of 15 - 25 Å. These monomers are the first pseudo-component of Komarov's [3] model. Moving away from the rock surface, the next layer occurs in a field that is influenced by long distance forces associated with the rock surface. As the distance from the rock surface increases rock-induced forces are diminished such that forces associated with interactions between water molecules and structures within associated polymers dominate. This part of pore liquid is the second pseudo-component of the Komarov [3, 4] model.

The thermodynamics of this model requires that the first component of water have strong adsorption that is localized in the surface layer of the rock particles. This will stratify the solution creating a border between the first component and other components further from the rock surface. This border is characterized by a dynamic equilibrium between water monomers and associated polymers. The ice solution in the binary pore solution is representing by two processes, thawing

of ice and mixing of the two determinate components of unfrozen water.

The main preconditions for model construction are in the labour [3, 4]. Evaluation of phase equilibrium parameters of water in salted and

$$\sum_i^2 [\ln(m_j f_j)_i]_{T=\theta_j} = \sum_i^2 \left[-\frac{L\theta_i}{RT_0^2} \sum_1^n \left(\frac{\theta_i}{T_0}\right)^{n-1} \right] + \sum_i^2 \left[\frac{\alpha_i \theta_i^2}{RT_0^2} \sum_1^{n+1} \frac{n}{n+1} \left(\frac{\theta_i}{T_0}\right)^{n-1} \right] + \sum_i^2 \left[\frac{\beta_i \theta_i^3}{RT_0^2} \sum_1^n \frac{n}{n+2} \left(\frac{\theta_i}{T_0}\right)^{n-1} \right] + \sum_i^2 \left[\frac{\gamma_i \theta_i^4}{RT_0^2} \sum_1^{n+3} \frac{n}{n+3} \left(\frac{\theta_i}{T_0}\right)^{n-1} \right] + \frac{I}{R} \left[\frac{(T_v - T_0) + \theta_i}{T_v(T_0 - \theta_i)} \right] \sum_i^2 (H_j^0 - H_j)_i, (n=1, 2, \dots, n) \quad (1)$$

unsalted rocks follows Komarov [3]:

where: m_j, f_j - mole concentration and coefficient of activity; j - component (solution); $\theta = T_f - T_0$ - freezing point temperature (T_f - K degrees); L - molar latent heat of crystallization of water in the volume; R - gas constant; $\alpha_i, \beta_i, \gamma_i$ - coefficients determined from the heat capacity of ice and unfrozen water for single temperatures in unsalted rocks and from salt concentrations and compositions for salted rocks; T_v - the temperature of experiment; $(H_j^0 - H_j)$ - the difference in enthalpies, which is the value of differential heat of adsorption and moistening with back sign for unsalted rocks, and it is the differential heat of solution for salted rocks; $i = 1$ for unsalted pore solutions, $i = 2$ - for pore solutions with soluble ions, n - the number of the member of sum ($n=1, 2, \dots, n$).

Equation (1) is a generalization of methods obtained by authors [6]. These authors considered single unsalted rocks where unfrozen water occurs in one of the three phases of H_2O and water properties correspond to the properties of deep cool water in freezing volume. This approach is less physically based. In contrast, properties of the solution in the freezing volume in my model are peculiar to the second conditionally determinate component, which is the solvent. Specific interactions between the surface of rock particles and adjacent layers of pore liquid, which do not freeze even under low negative temperatures, is not taking into account in previous approaches. The value for moisture of first component in my current analyzes varies from 0.45 to 0.7 which corresponds to maximum hygroscopic moisture. Transfer to the real surface layers of water is accomplished by adding a coefficient of surface activity for active salt ions.

1.2. The results of simulation.

The temperature curve of unfrozen water for askangel, calculated by equation (1) for unsalted rocks ($i=1$) and corresponding adsorption data are presented in Figure 1. Parameters used in equation (1) to generate the figure are described by Komarov [4]. Theoretical calculations (Fig. 1) are within 10-15% of experimental results (Figure 2). Data received from labours [2] derived using a variety of methods (e.g. nucleus magnetic resonance (NMR), calorimetry, contact and cryoscopic methods) produce characteristic peaks for calculated curves in temperature ranges of -16 to -18 °C and -45 to -47 °C (Figure 2).

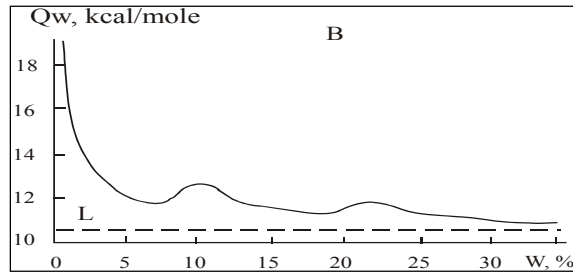


Figure 1. Dependence of differential adsorption heat Q_w on humidity W for the samples of montmorillonite [5].

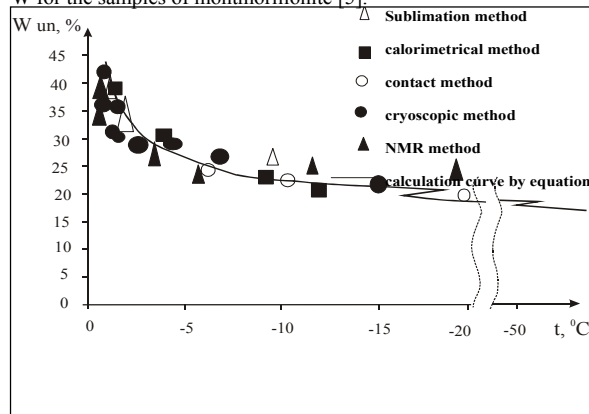


Figure 2. The comparison of calculated curve and experimental (obtained with different methods) data of volume of unfrozen water W_{un} for the samples of Na – montmorillonite.

These peaks are influenced by the interdependence of $Q_w = f(W)$ (Figure 1) and uncertainty that arises when the same value of heat adsorption can result from moisture with three possible phases moisture. Researchers have not previously considered this type of temperature dependence of unfrozen water. In my view this dependence is sensitive to small changes in the quantity of unfrozen water and considerable precision is required when using methods for determining phase consistence. This results in the smoothing of estimated adsorption on the graph. I suspect that this dependence of phase consistence on temperature is related to the intrusion of water between stratified silicate layers and expansion the lattice. Peaks in calculated curves are likely caused by the using of thermodynamic calculations to generate adsorption data. This would require that the surface of the rock not be deformed. However, the results of some work [8, 7] shows that this proposition is not correct even for rocks with inflexible cell structures (e.g. kaolin, talk and pyrophyllite). In particular, parameter B of cell structure changes as water is incorporated. The epitaxial growth of water films creates tension which drives mechanical deformation of particles. As a result, changes in phase consistence are gradual.

1.3. Experimental data.

Thermal capacity and enthalpy was determined by low-temperature differential scanning calorimetry (DSC) (calorimeter “Mettler TA-2000B”). This method is explained at length by Komarov [4]. Hysteresis was fixed for cycles of heating and cooling using the curves of DSC for heat capacity. Shifts in emission peaks varied from 10 to 17 degrees. Circumstantial evidence supporting the existence of crystal swelling in montmorillonite at negative temperatures is obtained by measuring heat capacity, which is a subtle indicator of structure deformations. There are three peaks in the plot of experimental data that relates heat capacity C_p and temperature $C_p = f(t)$ (Figure 3).

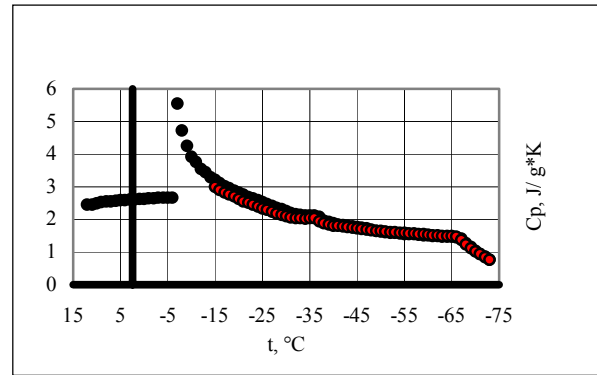


Figure 3. Experimental temperature curves of heat capacity for two samples of Na – montmorillonite ($W=15\%$).

Two of these peaks are likely caused by gradual intrusions of the first and second layers of water between silicate layers in montmorillonite. The range of these peaks corresponds to predicated values that take into consideration shifts in peak caused by changing temperature. These structural reformations cause heating that can be recognized on the DSC curves. In fact, these peaks fix for Li, Na, K, and Ca – montmorillonite [1].

The origin of these peaks was not explained by the original authors. We present our DSC curve in the labour (Komarov 2001, 2003), that we use to evaluate heat effects Q_{11} of the intrusion of second water layer into silicate structures. However, the sensitivity of calorimeters was insufficient to quantity the effect for first layer. It is $Q_{11} = 0.11-0.13$ j/g (related on gram of weight of sample of rock). It use calculated curve (Figure 2), which let to evaluate the quantity of unfrozen intruded water, that is necessary for evaluation of Q_{11} meaning on gram of unfrozen water. It is $1.2 \div 1.5$ %. Then the heat effect for gram of water is $Q_{11} = 20 \div 30$ j/g. This meaning is close to experimental data in positive range of temperatures, the valuations of heat of moistening of second water layer, which intrude to inter layer space of Na – montmorillonite and come to $Q_{11} = 12 \div 20$ J/g [8]. The evaluation is less on order as latent heat, which is emitted during the freezing of water. The fundamental interpretation of this effect with help of modeling, x-ray analyses transgress from borders of this paper and was discussed in the labour [4].

It is reasonably to appoint two ideas as applied to Martian conditions: a) taking into account the discussed phenomena lets to correct in the side of increasing adsorption moisture content in the regions with stratiform silicates in the surface layer; b) As the water evaporation heat could exceed ice sublimation heat in 1,5 times and more under low humidity, so ice existence in the rock leads to ice sublimation or its thawing and next adsorption of formed moisture as these processes are more thermalphysically efficiently.

- Reference:**
- Anderson, D. M. and Tace, A. R. (1971). *Soil Science Society of America Proceedings*, vol.35, no.1, pp. 47-54
 - Ershov, E. D. et. al. (1979). Phase compound of moisture in frozen rocks. MSU.pp.189
 - Komarov, I. A. (2001), *7-th International Symposium on Thermal Engineering and Sciences for Cold Regions*, Seoul ,Korea.
 - Komarov I.A., (2003), Thermodynamic and heat mass transfer in disperse frozen grounds, Moscow, *Scientific world*, pp.608.
 - Korolev, V. A. (1983), The collection of scientific works. Moscow. *MSU Publishing*, Vol. 5.
 - Low, P. F., Anderson, D. M., Hoekstra P. , (1968), *Water Resources Research*.4, N 2, p. 379-394.
 - Osypov, V. I. (1979), The origin of mechanical and deformation properties of clay rocks. Moscow. *Nedra*
 - Tarasevich, J. M. Ovcharenko, F. D. (1975), Kiev. *Scientific thought*, pp.351.

PROPERTIES OF DISPERSE FROST ROCK IN THE RANGE OF LOW NEGATIVE TEMPERATURES.

I.A. Komarov, V.S.Issaev, L. V. Mel'chakova

Geological Department, Moscow State University, Vorob'evy Hill, Moscow, Russia,119899

tpomed@garnet.ru

Abstract: this paper presents experimental data for thermo-physical properties of disperse terrestrial soils in the wide range of negative temperatures from 0 to -120 °C. We represent results of comparison with data of thermal lag of Marthian surface.

Introduction

Frozen soils are multi phases and multi component systems in the thermodynamic sense. As heat capacity is an additive amount, so its value is the sum of the heat capacities of its constituents: minerals of rock skeleton and organic components; pore solutions; pore ice; pore gases. Heat capacity of rocks was studied mainly for a range of positive and comparatively high negative temperatures [2].

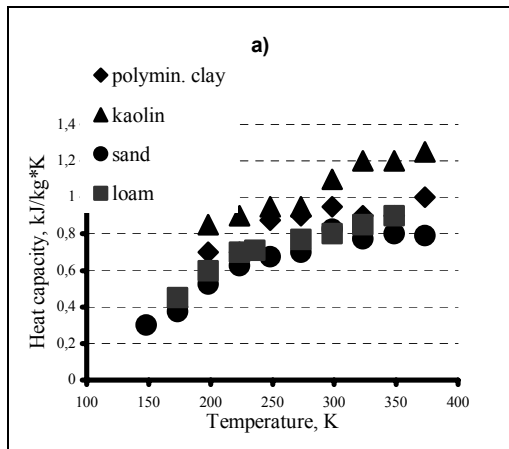
Observation

Experimental researches were surveyed on the basis of adiabatic and differential scanning calorimetry. Methods are described in the labours [5]. Experiments measuring heat capacity of rocks on using calorimetry were made for quartz sand, loam-sand and clays: kaolin, hydromicaceous. The samples were dried at a temperature of 105 °C.

Figure 1. Dependence of heat capacity of skeleton mineral material of various grain size and mineral composition on temperature: a – the data has received with adiabatic calorimeter, b – the data has received with differential scanning calorimeter "Mettler TA-2000B".

In accordance with Figure 1-a specific heat of the skeleton mineral material C_{sk} of soils varies with temperature: it changes little in the range of temperatures from -25 to 100 °C; C_{sk} falls with temperature decrease to -100 °C (30% for hydromicaceous clay). Satisfactory agreement (less 5-10% difference) is observed with similar data from [4] for calorimetric experiments in the range of temperature from 223 to 318 K with temperature steps of 15° and data of [7], who did experiments using a massive calorimeter. It is necessary to consider temperature dependence of heat capacity of skeleton minerals for a wider range of negative temperatures. The influence of mineral grain size in the range of temperatures from 100K to 140K correlates to notions about behavior of the heat capacity of minerals.

Results of experimental investigation of temperature dependence of heat conductivity coefficient of clay loam and quartz sand with fractions of 0.1 -0.25 mm under different values of moisture are given in Figure 2 a,b.



Heat capacity, kJ/kg*K

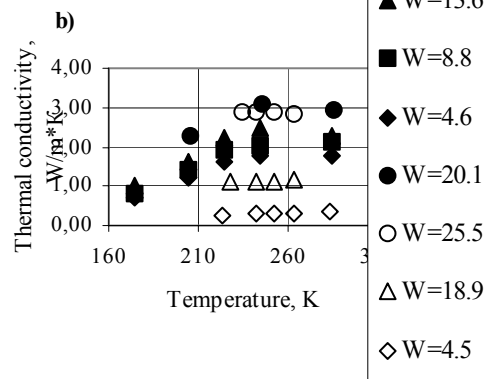
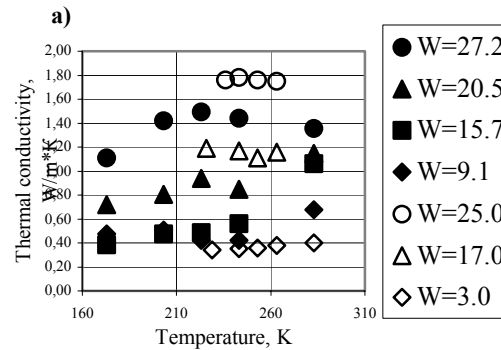
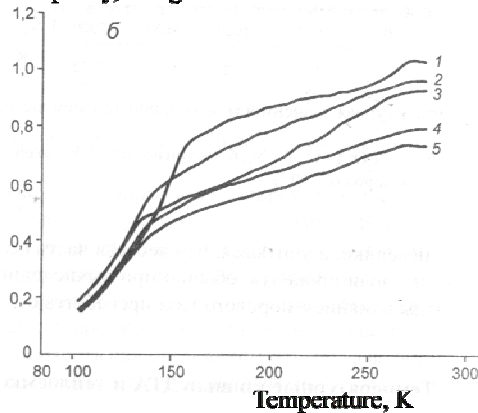


Figure 2. Dependence of thermal conductivity on temperature of various moisture contents: a - of quartz sand (fr.0.1-0.25); b - of clay loam. Unfilled badges are experimental results, filled badges are data from [4].

The coefficient of heat conductivity has inconsiderable dependence on temperature for the air-dry rocks in the light of represent dependencies. These data are comparable with data from [4] for the samples of soils with different dispersion in a more narrow range of temperature about -50°C (Figure 2 a, b). The sum of heat conductivity of soil in an air-dry state has to increase with decreasing temperature, as a result of increasing of heat conductivity of the mineral skeleton.

There is temperature dependence of coefficient of heat conductivity λ of quartz sand of two fractions (0.1-0.25 mm and 0.25-0.5 mm) form moisture on the Fig. 2 a. We observe considerable decreasing of λ value under temperature decreasing from -30 to -100°C , that has confirmed with data for more narrow interval of temperature (to -50°C) [4]. It conflict with assumption that summary coefficient of heat conductivity λ of ice-saturated rocks have to increase with decreasing of temperature. This assumption is based on the character of temperature dependence of thermal conductivity of separate rock's components. λ value of ice increase twice in the temperature range from 0 to -110°C . λ value of organic-mineral rock's skeleton in the same temperature range is not changed. λ value of loamy rocks in air-dry state also isn't related to the same temperature change. We suppose that the causes of λ decreasing are 1) micro-cracks formations in the pore ice (for temperature below -12°C); 2) micro-cracks formations on the pore ice - rock particle's boarder contact as the cause α values differences of phases; 3) micro-cracks formations in the organic-mineral skeleton of rock as the cause α values differences of minerals. Structure's formation leads on decreasing of λ as the cause of increasing of pore gas contents. Comparison of calculation and experimental data with data of distance probe and of morphometric analyses of Martian surface. Data of thermophysical properties for surface layer of Mars could be received from the values of thermal lag I . These values are transmitted from landing space modules. The value $I = (\lambda C \rho)^{1/2}$ equals to $0.004 \div 0.017 \text{ cal/cm sec}^{1/2} \text{ K}$, and rock's density ρ is from 1 to 1.6 g/cm^3 [6]. λ value changes from 0.2 to 0.12 W/m K for $C = 0.42 \text{ kJ/kg K}$. λ values for sandy rocks are in this range. It received from calculation of experimental data for terrestrial atmosphere's conditions with correction to the value of Martian atmosphere's pressure on the surface (6 mm of mercury) Figure 5. It is based on the method [1] for conditions of gaseous phase flowing $22 \geq \text{Kn} \geq 0.1$, where Kn is Knudsen's criterion. Accommodation coefficient is chosen for CO_2 -quartz system. I value changes from 0.004 to $0.006 \text{ cal/cm sec}^{1/2}$ (Kuzmin, 1983) K . It corresponds to λ values from $0.05 \div 0.12 \text{ W/m K}$. This range for Martian atmosphere corresponds to thermal conductivity of dusty particles.

The reason for non increase of heat conductivity of mineral skeleton is heterogeneity of mineral composition and differences in coefficient of linear growth which leads to formation of micro cracking in organic mineral skeleton of rocks. The summary effect of these processes could be dominant and could lead to a decrease in the value of heat conductivity.

The reason of this is increasing of gaseous phase content. Micro cracking process was proved by micro photograph researches, which were done on the basis of the replica method [5]. These effects are more clearly revealed in the analyses of the behavior of heat conductivity of wet soils (Figure 2 a, b). As the temperature dependence of the coefficient of heat conductivity of air-dry soil sand of ice shows by its behavior (abruptly increase of coefficient of heat conductivity with decreasing of temperature about 50 K , so it is reasonable to propose that the sum effect of heat conductivity will increase with fall of temperature for wet rocks. It confirms by experimental data of linear expansion α received on the basis of laboratory work with Japanese dilatometer "Sinky-Rico" model DL-150LS [3]. Nevertheless experimental data does not prove this suggestion. Heat conductivity of kaolin changes inconsiderable with temperature decreases under moisture content of 20% . Heat conductivity firstly decreases and later inconsiderably increases for rocks with moisture content of less than 20% . Heat conductivity falls under temperature decreases from -30 to -100°C for sand samples, which have some individual differences for each sand fraction.

The reasons, which are determined experimentally for decreasing of the value of coefficient of heat conductivity under decreasing of temperature, are the following: formation of micro cracks inside pore ice; formation of micro cracks on the particle - ice interface; existence of micro cracking in organic mineral skeleton. The sum effect of these processes became dominant and leads to decreasing of value of coefficient of wet rock heat conductivity.

References

1. Dulnev, G.N. & Zarychnyak, Y.P. (1974). Leningrad, *Energy*, p. 264
2. Ershow, E. D. (1996). Moscow: *MSU*. p. 397.
3. Ershow, E.D., Komarov, I. A., Brushkova A.V., Hors M.N., (2001), *Proceeding of 2 conference of Russian geocryologists*, . *V.1*, pp 81-88.
4. Haynes, F. D., Carbu, D. L. & Van Pett D.J.(1991). *United State army. Corps of engineers. Cold regions research and engineering laboratory. Hanover, New Hampshire, USA, Ser Crel*.
5. Komarov, I.A. (2003). Thermodynamics и thermomasse transfer and frozen disperse rocks. *Scientific world*, Moscow. pp608
6. Kuzmin, R. O. , (1983), Moscow, *Science Press*. 144 p.
7. Shusherina, E. P. (1973), *Proceeding of 1 All union symposium of rheology of rocks*: 282-292. Erevan: Erevan University.

SEASONAL MELTING OF SURFACE WATER ICE CONDENSING IN MARTIAN GULLIES. K. J. Kossacki, *Institute of Geophysics, Warsaw University, Pasteura 7, 02-093 Warsaw, Poland, (kjkossac@fuw.edu.pl)*, W. J. Markiewicz, *Max-Planck-Institute for Aeronomy, Max-Planck-Str. 2, 37191 Katlenburg-Lindau, Germany.*

Abstract

In this work we consider when and how much liquid water during present climate is possible within the gullies observed on the surface of Mars. We analyze the conditions for melting of H₂O ice, which seasonally condenses within the troughs of the gullies. The model includes both an approximate topography of the gullies as well as the inclination of the slope where the gullies appear. We have found, that water ice condensed in winter on the walls of gully-like troughs can undergo transition to the liquid phase after complete sublimation of CO₂ ice. The amount of liquid water obtained in this way, depends on several parameters but is most likely to be very small.

Introduction

The gullies are one of the most intriguing features discovered with the recent high resolution orbiter imaging of the surface of Mars. They are mostly found on slopes of craters but also on sides of isolated knobs. The gullies are believed to indicate recent surface flows, presumably of liquid water. To date, the details of the formation process of the gullies are not known. Several authors considered creation of gullies by seasonal melting of ice condensing on the surface ((2), (7), (1), (3)). However, these authors assumed flat surface, or at best smooth crater slope without local topography. According to (3) the conditions for melting of water ice can be satisfied on preferentially insolated slopes almost everywhere on Mars, but only at the surface. On the other hand, (1) has shown possibility of water ice melting to a depth of some meters below the appropriately inclined slopes, but not at the present obliquity.

In this paper we address the problem of the role of the shape of the gullies in the diurnal and seasonal cycles of the surface temperature in the present Mars climate conditions. The local topography needs consideration, because the exact slope of the local surface is of key importance for the energy balance and hence for quantifying the conditions for the possible condensation and melting of water ice. We try to answer the question, when and how much liquid water is it possible to form within the gullies on poleward directed slopes. The first condition for this is that the surface has to be above the melting temperature of water ice. At current obliquity, even at high latitudes Martian surface can warm up to temperatures allowing melting of water ice, but only in a very thin surface layer. The second condition is that the atmospheric pressure is above the triple point of water which is 6.1 mbar. In the north hemisphere pressure is high enough for this even at high latitudes, but in the south only at low and regionally middle latitudes.

Model

We analyze heat transport and evolution of ice distribution in the near surface layer of the regolith, in the vicinity of the north-south oriented trough located on a slope, as are most of the the gullies in the south hemisphere (1). The model includes diurnal and seasonal variations of the position of the Sun as well as seasonal variations of atmospheric pressure and composition. Surface condensation and sublimation is calculated for CO₂ and H₂O, on all facets of the troughs. Condensation and sublimation of H₂O is calculated accounting for the temperature dependence of the sublimation/condensation coefficient correcting Hertz-Knudsen equation (5). The model used in this work is based on that presented in (6). The current version differs from the previous one by allowing local inclination of the surface, accounting for the condensation of atmospheric water and including a more consistent way of treating the scattering of light in the atmosphere toward the surface (4).

Results and conclusions

We present the results obtained for two example locations at middle latitude in both hemispheres. They are 50°S, 50°E and the region of Viking 2 landing site at 48°N, 134°E. The surface density of the condensed water ice strongly depends on the atmospheric conditions, in particular strength of the local eddy diffusion which in turn can be parameterized in terms of the speed of the surface wind. For the volcano slopes (8) predict wind speeds reaching 40 m/s. We performed simulations with wind speed 5 m/s and 30 m/s. Toward the end of winter, more and more of the interior facets of the trough become exposed to the direct light. However, the walls receive significant flux of energy only when they are insolated at small angle to the local normal, in the morning at about 6:00 and in the afternoon about 18:00 LST. Thus, seasonal CO₂ ice remains on the walls for some time after the end of winter. When the trough is located on a slope at 50°S, 50°E the middle parts of the walls remain covered by CO₂ ice until $L_s \sim 250^\circ$. Rapid warming of the surface free of CO₂ ice leads to an almost immediate melting of H₂O ice. In the trough located at 48°N, 134°E melting process starts several sols after the complete sublimation of CO₂ ice, when the layer of H₂O ice is thin enough to have no significant influence on the albedo. Fig.1 displays model results for the Viking 2 landing site at 48°N, 134°E. The gully is assumed to be on a slope inclined by 30°. The curves show the evolution of the diurnal maximum of amount of water ice and liquid water on the middle of the west wall of the trough. Thus, the vertical distance to the surface of the slope from this point is 1m. In this place the surface density of ice reaches the maximum value of about 0.7 kg m^{-2} , at $L_s \sim 69^\circ$. After this date diurnal maximums of surface

water ice decreases with the rate depending on the chosen form of the sublimation/condensation coefficient α . When $\alpha = 1$ (classical approach), water ice disappears within one sol. When α is a function of temperature (5), water ice persists until $L_s \sim 73$. The amounts of liquid water, which may appear,

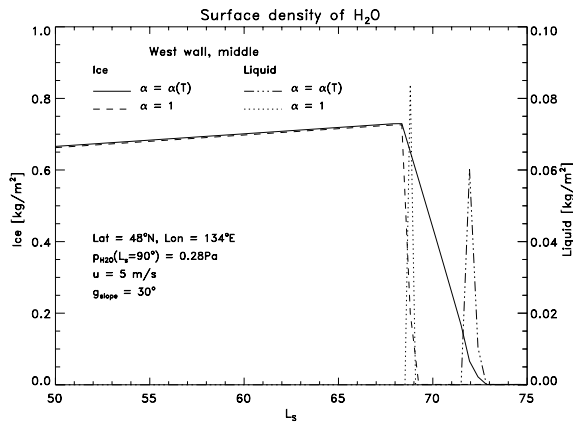


Figure 1: Daily maximum of the surface density of water ice and liquid water, on the middle part of the west wall of the gully-like trough at 48°N , 134°E . The seasonal maximum of vapour pressure is 0.28Pa . The curves are for the sublimation coefficient $\alpha = 1$, and for $\alpha = \alpha(T)$.

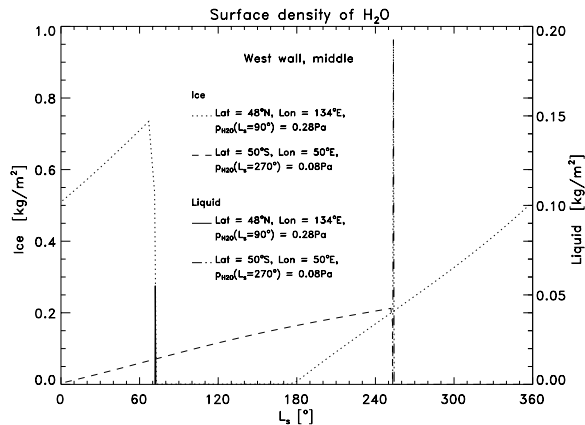


Figure 2: As Figure 1 but for both areographic locations: 48°N , 134°E and 50°S , 50°E , and for a whole Martian year with $\alpha = \alpha(T)$.

are shown as dotted and dashed-dotted lines. The curves are for the diurnal maximum of the surface density of liquid water, again for both forms of the coefficient α . In both cases amount of liquid is less than 0.1 kg m^{-2} , significantly smaller than the seasonal maximum of the accumulated amount of ice. This is because the surface covered by thick layer of ice has high enough albedo for the water ice to absorb enough energy to significantly sublime but not to melt. Ice can start melting only when the amount of surface ice is so small, that it does not affect the optical properties of the surface (in our model $100\mu\text{m}$). For

the trough located in the southern hemisphere, at 50°S , 50°E the spring time insolation is higher and the albedo enhanced due to presence of ice does not prohibit warming of the surface to the melting temperature. This results in the surface density of liquid water being comparable to that of the accumulated water ice, Fig. 2. During the day when the liquid appears in a given place, maximum local temperature greatly exceeds boiling point under low pressure of the Martian atmosphere. Thus, no moisture is likely to remain on the surface until next day. The maximum surface density of liquid water for this location is 0.2 kg m^{-2} .

We analyzed the seasonal cycle of condensation and sublimation of CO_2 and H_2O in the gully like troughs, about ten meters wide. Our simulations show that the H_2O ice deposited in seasonal (winter) cycle on the walls can undergo transition to the liquid phase in spring. When the trough is on the slope at 50°S , 50°E and inclined by 30° , the amount of moisture resulting from our simulations is only about 0.2 kg m^{-2} and can appear in a given place during one day only. The rate of condensation is proportional to the wind speed so that simulations with winds of 30 m/s result in about 1 kg m^{-2} of liquid water. This amount is probably still not enough to cause surface flow.

References

- [1] Costard, F., Forget, N., Mangold, J. P., Peulvast, J. P., Formation of Recent Martian Debris Flows by Melting of Near-Surface Ground Ice at High Obliquity, *Science*, 295, 110–113, 2002.
- [2] Haberle, R. M., McKay, C. P., Schaeffer, J., Cabrol, N. A., Grin, E. A., Zent, A. P., and Quinn, R., On the possibility of liquid water on present-day Mars, *J. Geophys. Res.*, 106, 23,317–23,326, 2001.
- [3] Hecht, M., Metastability of liquid water on Mars, *Icarus*, 156, 373–386, 2002.
- [4] Kieffer, H. H., Titus, T. N., and Mullins, K. F., Mars south polar spring and summer behavior observed by TES: Seasonal cap evolution controlled by frost grain size., *J. Geophys. Res.*, 105, 9653–9699, 2000.
- [5] Kossacki, K. J., Markiewicz, W. J., Skorov, Y., and Kömle, N. I., Sublimation coefficient of water ice under simulated cometary-like conditions, *Planet. Space Sci.*, 47, 1521–1530, 1999.
- [6] Kossacki, K. J., and Markiewicz, W. J., Surface temperature of Martian regolith with polygonal features: influence of the subsurface water ice., *Planet. Space Sci.*, 51, 569–580, 2003.
- [7] Mellon, M. T., and Philips, R. J., Recent gullies on Mars and the source of liquid water., *J. Geophys. Res.*, 106, 23,165–23,180, 2001.
- [8] Rafkin, S. C. R., Sta. Maria, M. R. V., and Michaels, T. I., Simulation of the atmospheric thermal circulation of a martian volcano using a mesoscale numerical model., *Nature*, 419, 697–699, 2002.

SURFACE FEATURES OF THE SOUTH POLAR LAYERED DEPOSITS OF MARS AND POSSIBLE TERRESTRIAL ANALOGUES

M. R. Koutnik¹, S. Byrne², and B. C. Murray², ¹University of Washington (Box 351310, Seattle, WA 98195, mkoutnik@geophys.washington.edu), ²California Institute of Technology (shane@gps.caltech.edu, bcm@gps.caltech.edu).

Introduction: Data from the Mars Orbiter Camera (MOC) and the Mars Orbiter Laser Altimeter (MOLA) aboard the Mars Global Surveyor (MGS) mission have provided important new clues to the past history of the South Polar Layered Deposits (SPLD). There are distinct features presented here that have been observed almost exclusively with these data sets and are unique to the south polar region of Mars. Although we do not conclusively know the origin of these features and don't rule out other interpretations, we consider here the possibility that relatively recent subglacial volcanism and possibly the influence of ice flow may have been active in their formation.

Regional Description: We focus primarily on one region of the SPLD, approximately 190° - 230° W, 85° - 87° S (no MGS coverage south of 87°), where nearly all the features discussed here are found. Most extensive in this area are enigmatic large-scale grooves, termed here the "Wire Brush" terrain. Coverage of the Wire Brush terrain in the MOLA shaded relief map are shown in Figure 1. This region can be identified in Viking coverage of this area and shows that the grooves possibly have a connection with the current residual cap. Poleward of Chasma Australe and possibly one area off the cap are the only other locations where we see this grooved pattern at the south pole.

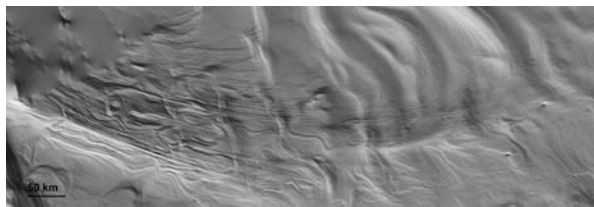


Figure 1. MOLA shaded relief map of the full extent of the Wire Brush Region, 190° - 230° W, 85° - 87° S.

The overall grooved pattern of the Wire Brush region is continuous for more than 300 km, though tracing of individual grooves is difficult to do with certainty for more than about 50 km. The grooves do continue linearly across local topography and are several hundreds of meters across with vertical relief of only a few tens of meters. The slope over the extent of the wire brush terrain is very slight and the grooves do not seem to be influenced by any larger scale topography.

Near to the Wire Brush terrain there are numerous other unique features that may provide clues

to the origin and timing of formation of the large-scale grooves.

Sinuuous Ridges and Enclosed Chasma: There are sinuous ridges cross-cutting the Wire Brush which we have termed "Snakes". The Snakes are up to 2 km in width and tens of km long, although they are only a few tens of meters high. The presence of such vertical features is unusual. It could imply an episode of deformation or fracturing that has been filled subsequently with more resistant material than the surrounding layered deposits. The Snakes are found primarily within the Wire Brush but do extend out from this region as well. At least one Snake extends into an adjacent elongated depression and can be seen to interact with layering in this chasma. The enclosed chasma, shown in Figure 2, is a significant feature in association with the Wire Brush terrain. Unlike Chasma Australe, this chasma does not cut all the way through the layered terrains to the underlying basement rock and does not have an outlet. Given the positions of these two chasmas, on both sides of the Wire Brush Terrain, it is possible that all of these features may be related.

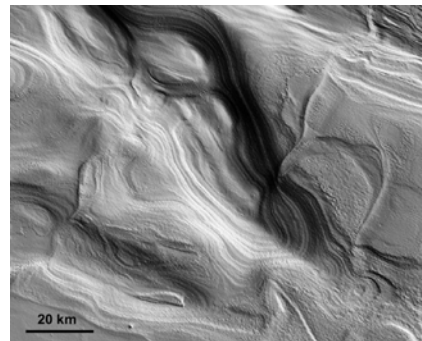


Figure 2. Enclosed depression adjacent to the Wire Brush region (seen in upper right). The Snake features can be seen cutting into the chasma from the right of the image.

Polar Potholes: Another interesting component of the Wire Brush and surrounding region is the presence of small, circular pits. They are found distinctly in the regions 190° - 230° W, 85° - 87° S (within the Wire Brush terrain) and 135°-175° W, 85°-87° S and can be roughly distinguished by orientation and morphology within these two regions. All of the individual polar potholes in both regions are approximately 50-100 m

in diameter. The potholes found within the Wire Brush region are circular, distinct forms. An interesting grouping of potholes is shown in Figure 3 where they are clustered in local circular depressions. The entire population of potholes is found only on the south polar layered deposits and these clustered forms are only in the Wire Brush region.



Figure 3. MOC NA m1102900 showing a distribution of potholes in the Wire Brush terrain that are grouped in larger circular depressions.

Mounds: North along the direction which the grooves trend in the Wire Brush terrain, there is a clustering of distinctive mounds, shown in Figure 4 and can also be seen in the far right of Figure 1. The mounds are few km in diameter and all have similar topographic features as observed from MOLA. The occurrence of these mounds in this location (and nowhere else we have found) and that they share a similar shape leads us to believe they could have a volcanic origin.

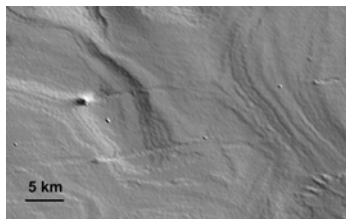


Figure 4. Two of the mound features associated with the Wire Brush region. They appear to act as obstructions, as evidenced by the linear "tail".

Interpretations: The Wire Brush region and associated features could conceivably be the signature of unusual past winds, ancient ice sheet motion, or episodes of catastrophic flooding originating from beneath earlier residual caps. We have explored these interpretations [1] and now look for a mechanism or combination of mechanisms that can best explain all the features we have presented here near to the Wire Brush terrain. Assuming the features we see in this localized region of the SPLD originate from the same or a similar event in south polar history, the interpretation of subglacial volcanism is favored here. As the clustered mounds, enclosed chasma, and

sinuous ridges are especially supportive evidence for volcanism. As well, elsewhere in the south polar region, Ghatan and Head [2] have proposed a past episode of subglacial volcanism of Hesperian age. We do not attempt to explain why there would be a period of increased heat flux in this region but acknowledge that an event like this cannot be completely ruled out.

We will also assess the possibility of ice sheet motion driven by basal melting from changes in cap configuration, not from increased heat flux, active at the south pole in the Martian past. Basal melting beneath the Martian polar caps has been considered possible but is highly sensitive to surface temperature, cap thickness, thermal conductivity, and heat flux [3, 4]. With a heat flux one-third to one-half the terrestrial value [3] basal melting can most easily occur when the ice cap is thick and the conductivity is low, assuming negligible heat production from internal deformation [4]. If basal melting or meltwater generation occurred in the past without increased heat flux, it is assumed that the south polar cap was more extensive or there was a warmer climate. We look at the cap configurations and timing necessary to produce meltwater at the base for the south polar cap.

If the base was lubricated (by cap configuration or increased heat flux) it could be possible to produce large grooved features in the layered terrain by ice flow, analogous to terrestrial ice streams. We also consider the possibility of a large outburst flood occurring, as seen in Icelandic jokulhlaups. It has been proposed that Chasma Australe was formed by a large outburst flood [5] and, given the possible relation of these features to the Chasma, these same arguments could apply for the Wire Brush region.

We consider the processes of subglacial volcanism and ice sheet motion to be possibly active in forming the enigmatic surface features seen in this region of the Martian south pole. The unique location of all these features is evidence of a significant event in the Martian past that had a considerable influence on the SPLD.

References: [1] Koutnik, M., et al. (2003) 6th International Mars Conference. [2] Ghatan, G. and J. Head (2002) *J. Geophys. Res.* 107, E7, 2002. [3] Clifford, S. (1987) *J. Geophys. Res.* 92, B9, 9135-9152. [4] Larsen and Dahl-Jensen (2000) *Icarus* 144, 456-462 [5] Aquita, F. et al. (2000) *Icarus* 144, 302-312.

POLAR WANDER IN THE GEOLOGICAL HISTORY OF MARS: CONSTRAINTS FROM TOPOGRAPHY STATISTICS. *M. A. Kreslavsky*^{1,2} and *J. W. Head*¹, ¹Dept. Geological Sci., Brown University, Providence, RI 02912-1846, USA; misha@mare.geo.brown.edu, ²Astronomical Institute, Kharkov National University, Ukraine.

Introduction: True polar wander (that is change of position of the spin axis of a planet relative to the crust) has been hypothesized for Mars long ago (see [1] for review). The general idea is the formation of Tharsis rise should shift any initial spin axis position so that the rise is centered at the equator.

P. Schultz and A. Lutz [2,3] presented two principally different lines of observational evidence for true polar wander in the past. First, they found [2] a significant excess of large impact craters made by grazing impacts, and attributed them to impacts of tidally decelerated former satellites of Mars, which dynamically could only orbit Mars close to its equatorial plane; location and orientation of such craters suggested a position of the equator very different from that of the present-day. Second [3], Schultz and Lutz found concentration of specific deposits in Arabia Terra and on the opposite side of the planet (Medusae Fossae Formation) which they interpreted as remnants of former layered terrain similar to the present-day polar caps.

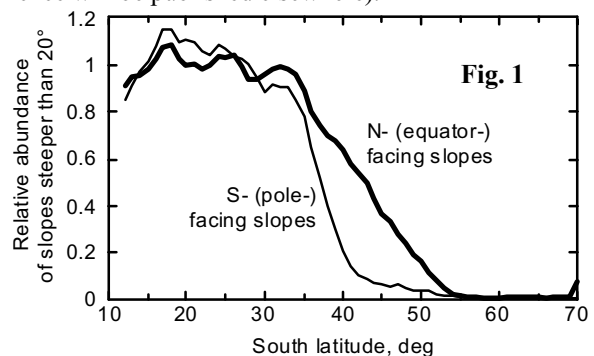
Recently, analysis of strong magnetic anomalies in the southern highlands of Mars provided some new evidence for the polar wander in the past. J. Arkani-Hamed [4] showed that if one suggests that the crustal magnetization reflects the extinct planetary dipole magnetic field at some moment in the past, then inferred positions of the magnetic dipole axes are clustered in a 30° wide area around 130°W 25°N. Since the deflection of the magnetic dipole axis from the spin axis is not high (at least for the same mechanism of magnetic field generation as on the Earth), the inferred pole position in the Early Noachian is close to this point. This point does not coincide with, but is rather close to, the former pole location proposed in [3].

Analysis of the current topography and rotation state of Mars led B. G. Bills and T. S. James [5] to the conclusion that the present-day rotation of Mars is secularly unstable. If the data used for the inference are accurate, than the spin axis can wander at a rate defined by the characteristic time scale of relaxation of elastic stresses in the lithosphere.

Our recent studies showed pronounced latitudinal zonality of the statistical characteristics of the kilometer-scale topography of Mars [6-8]. Here we analyze constraints that our findings put on the hypotheses of past true polar wander.

Observations: Statistical analysis of martian topography along topographic profiles obtained with MOLA

altimeter [9] onboard MGS showed [6] that the circum-polar regions (above 60° latitude) are consistently smoother at kilometer and subkilometer scales than the equatorial zone (below 30° latitude) with a gradual transition with some statistical peculiarities [7] between them. Recently we found [8] that the latitudinal trend of roughness is accompanied by even more pronounced latitudinal trend of steep slope occurrence. **Fig. 1** shows the relative frequency of slopes steeper than 20° as a function of latitude for typical southern highlands in Terra Cimmeria. It is seen that the steep slopes practically disappear above 50° latitude. **Fig. 2** shows locations of the steepest slopes on Mars. The paucity of extremely steep slopes at high latitudes is obvious. (Detailed analysis of the steepest slope occurrence will be published elsewhere).



When we move from the equator to the poles, the abundance of steep slopes drops down sooner for the pole-facing slopes and later for the equator-facing slopes (Fig. 1). This produces a strong asymmetry in steep slope abundance at 40-50°S.

Fig. 3 shows the map of normalized median differential slope at 0.3 km baseline inferred from along-profile statistics. This parameter is a characteristic of the north - south slope asymmetry (see [8] for details). Fig. 3 shows two distinctive belts around 45° latitude in both hemispheres with the opposite sign of the asymmetry parameter, which shows that the equator-facing slopes in both bands are systematically steeper than pole-facing slopes. Note that the map in Fig. 3 reflects the behavior of typical (a few degree steep) slopes, while Fig. 1 and 2 are related to the steepest slopes on the planet. (For discussion of other features seen in Fig. 3 see [8].)

Both belts of slope asymmetry (Fig. 3) show a small deflection from ~45° parallel to the south in the western hemisphere and to the north in the eastern one. The

bands are well approximated by minor circles with 45° radii and the centers shifted $\sim 5^\circ$ from the poles toward $60\text{-}90^\circ\text{W}$ in the northern hemisphere and to the opposite direction in the southern hemisphere.

Interpretation: The approximate symmetry relative to the equator strongly suggests that the role of insolation was important in the formation of the observed trend and the anomalous belts. F. Costard and co-authors [9] have pointed to the possibility of melting of thick layers of ground ice at higher obliquity. Their calculations showed that starting at $\sim 35^\circ$ obliquity, the summertime day-average surface temperature reaches 0°C at high ($>60^\circ$) latitudes; for higher obliquity the zero summer isotherm shifts toward the equator. The day-average temperature can exceed the ice melting point down to $\sim 40^\circ$ latitude at 45° obliquity, but only on steep pole-facing slopes.

We suggest that transient melting of ground ice in summer during periods of high obliquity promotes downslope movement of material and lowers steep slopes. Over geological time scales, this process removed almost all steep slopes above 50° latitude. At $40\text{-}50^\circ$ latitude, the summertime melting and related movement can occur only on pole-facing slopes, making these slopes less steep. The equator-facing slopes in this zone remain intact. This produces the observed latitudinal trend and strong asymmetry of the steepest slopes.

Implications for past polar wander. Well preserved steep slopes in the equatorial highlands are mostly related to impact craters. If our interpretation of the latitudinal trend of the steep slope occurrence and the slope asymmetry bands is correct, the preservation of steep slopes in the equatorial highlands means that the day-average temperature have never exceeded 0°C in these regions. Hence, these regions have never been at high latitudes during the time comparable to the highland crater population age. This constrains the true pole position during the whole Amazonian (and probably the Hesperian; more detailed analysis is necessary) to the vicinity of the present poles.

The deflection of the belts from 45° latitude might be related to effects of persistent atmospheric circulation or albedo patterns during the high obliquity epochs. We believe that it is more plausible that the current pole position is shifted $\sim 5^\circ$ from a formerly stable or long-term-average position. The direction of this shift is neither similar nor opposite to the shift of the geometric centers of the present-day polar layered deposits [10]. The same is true for the platy unit, a geologically older layer of the northern polar deposits [11]. Thus, we see not too strong, but positive evidence for polar wander of $\sim 5^\circ$ amplitude around its average position, which

is determined by the centers of the slope asymmetry belts. The dynamic plausibility of such a process is the subject of a separate study.

Thus, we conclude that planetary-scale polar wander has not occurred since the Hesperian. The topographic information about the Noachian is more obscured, because of the large number of steep slopes produced by cratering and tectonics since that time. However, some information could survive in the topographic record of the Noachian-age highlands. We are presently analyzing this information to test the hypothesis of a different location of the spin axis in the Noachian.

References: [1] Ward, W. R. (1992) In *Mars*, Univ. Arizona Press, 298-320. [2] Schultz, P., and Lutz-Garihan A. B (1982) *Proc. LPSC XIII*, A84-A96. [3] Schultz, P., and Lutz A. B. (1988) *Icarus* 73, 91-141. [4] Arkani-Hamed, J. (2001) *GRL* 28, 3409-3412. [5] Bills, B. G., and T. S. James (1999) *JGR* 104, 9081-9096. [6] Kreslavsky, M. A. and J. W. Head (2000) *JGR* 105, 26695-26712. [7] Kreslavsky, M. A. and J. W. Head (2002) *JGL* 29, 1719, 10.1029/2002GL015392. [8] Kreslavsky, M. A. and J. W. Head (2003) *JGL* 30, 10.1029/2003GL017795 [9] Costard, F. et al. (2002) *Science* 295, 110-113. [10] Fishbaugh, K. E., and J. W. Head (2001) *Icarus* 154, 145-161. [11] Byrne, S. and B. C. Murray (2002) *JGR* 107, 10.1029/2001JE001615.

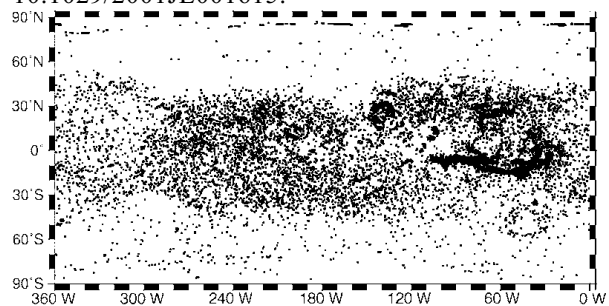


Fig. 2. Distribution of the steepest slopes on Mars. Each dot denotes a 300 m long segment of MOLA profile with slope steeper than 30° . In high-concentration areas the dots strongly overlap.

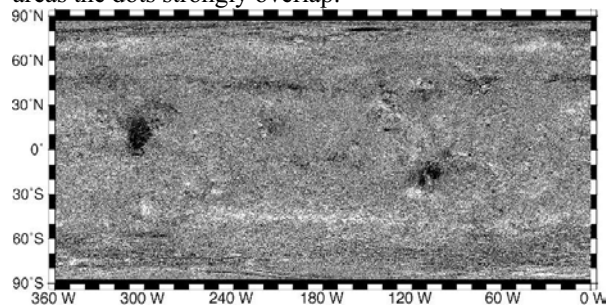


Fig. 3. Distribution of slope asymmetry parameter. Brighter (darker) shades mean that north- (south-) facing slopes are steeper.

DETERMINING STRUCTURAL AND MECHANICAL PROPERTIES OF SNOW WITH A HIGH-RESOLUTION PENETROMETER. K. Kronholm¹, J. B. Johnson² and M. Schneebeli¹, ¹WSL Swiss Federal Institute for Snow and Avalanche Research SLF, Flüelästrasse 11, CH-7260 Davos Dorf, Switzerland, kronholm@slf.ch, ²Cold Regions Research and Engineering Laboratory CRREL, Fairbanks, Alaska.

Introduction: On Earth, and possibly in extraterrestrial environments, the snow cover consists of individual snow layers that metamorphose over time. The stratigraphic record of snow layers is the result of erosional and depositional events. Adjacent layers differ in terms of their structural and mechanical properties. The structural properties of the upper snow layers are important for the chemical exchange between the atmosphere and the snow cover, snow hydrology, and the spectral properties of the snow cover. The mechanical properties are relevant for over-snow trafficability of vehicles and animals, and for avalanche release. Traditionally, snow is characterized by subjective measures of grain shape and size, and hardness [1]. Until recently, no fully automatic and objective methods to describe snow microstructure were available. The recent development of a snow micropenetrometer (SMP) now provides an objective way to measure the structural and mechanical properties of snow layers at different spatial scales [2, 3]. The SMP interpretation methods used for snow have also been used to objectively characterize soil [4].

Methods: With the SMP, we measured the penetration resistance of a seasonal snow cover. The force-distance signal had a sampling interval of 4 μm . The microstructural properties (microstructural element length and mean grain size) were derived from the signal by relating each force spike to a fracture of a microstructural element. The distance between fractures is directly related to the size of the microstructural elements [5]. Mechanical properties (compressive strength and elastic modulus) were derived using a mechanical theory developed for cohesive granular materials [5]. For comparison, a traditional stratigraphic profile with grain shape, size and hand hardness was done in addition to the SMP measurements. Snow samples were taken from individual layers. The spatial variation of structural and mechanical properties was analyzed for individual layers using geostatistics.

Results: The microstructural element length and the mean grain size derived from the penetrometer signal corresponded well with the results from the traditional methods. The derived compressive strength was within the previously reported ranges [Fig. 1]. The derived elastic modulus was a factor two lower than previously reported values. The mechanical properties of individual layers showed a large spatial variation on a single slope. The spatial variation in microstructure

was not as large. Large spatial variation in structural and mechanical properties of individual layers was mainly found in layers deposited during windy conditions.

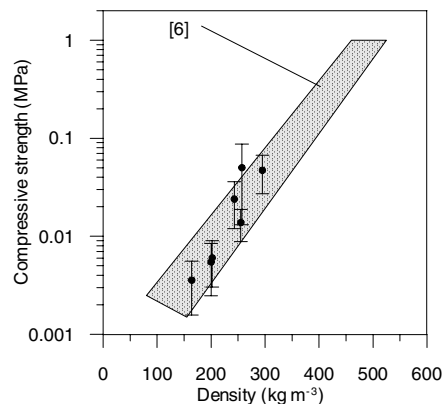


Fig. 1. Compressive strength of snow layers as a function of bulk density. Previously reported values are indicated by the grey area.

Discussion: The large spatial variation found in a terrestrial snow cover emphasizes the need to carry out multiple measurements to accurately characterize the three-dimensional variations of the snow cover properties. The representativity of a single measurement depends on the influence of wind in the snow stratigraphy. On Earth, a single measurement is usually not representative for a large area. The SMP can be used to derive important structural and mechanical properties of individual snow layers in a natural setting. An accurate description of the structural and mechanical properties of the upper snow layers and low density layered deposits on the polar areas of Mars could be obtained with a micropenetrometer mounted on a rover. Measurements could be done at certain intervals as the rover explores the Martian surface.

References: [1] Colbeck S. C. et al. (1990) *IAHS-ICSJ Publ.* [2] Johnson, J. B. and Schneebeli M. (1998). Snow strength penetrometer, United States Patent 5,831,161, U. S. Patent Office. [3] Schneebeli M. and Johnson J. B. (1998) *Ann. Glaciol.* 26, 107-111. [4] Johnson, J. B. (2000). *Transportation Research Record*, 1714, 83-88. [5] Johnson J. B. and Schneebeli M. (1999) *Cold Reg. Sci. Technol.* 30, 91-100. [6] Mellor M. (1975) *IAHS Publ.* 114, 251-291.

PRELIMINARY CHARACTERIZATION OF A MICROBIAL COMMUNITY OF ROCK VARNISH FROM DEATH VALLEY, CALIFORNIA. K. R. Kuhlman¹, M. T. La Duc¹, G. M. Kuhlman¹, R. C. Anderson¹, D. A. Newcombe^{1,2}, W. Fusco², T. Steucker², L. Allenbach², C. Ball², and R. L. Crawford², ¹Jet Propulsion Laboratory, California Institute of Technology, 4800 Oak Grove Dr., Pasadena, CA 91109, kkuhlman@jpl.nasa.gov; ²Environmental Research Institute, University of Idaho, Moscow, ID 83844, crawford@uidaho.edu.

Introduction: Rock varnish (also referred to as desert varnish in the literature because it is particularly noticeable in desert environments) is a dark, thin (typically 50-500 μ m thick), layered veneer composed of clay minerals cemented together by oxides and hydroxides of manganese and iron [1-4]. Some scientists suggest that varnish may provide a historical record of environmental processes such as global warming and long-term climate change. However, despite more than 30 years of study using modern microanalytical and microbial culturing techniques, the nucleation and growth mechanisms of rock varnish remain a mystery [4,5].

Rock varnish is of interest to the Mars science community because a varnish-like sheen has been reported on the rocks at the Viking Lander sites [6,7]. It therefore important for us to understand the formation mechanisms of terrestrial varnish – abiotic, biotic, or a combination of the two -- as this understanding may give us clues concerning the chemical and physical processes occurring on the surface of Mars. It is strongly believed by some in the biogeochemistry community that microbes have a role in forming rock varnish, and iron- and manganese-oxidation by microbes isolated from varnish has been extensively investigated [8,15-16]. Only two of these studies have investigated the microbial genetics of varnish [16,16]. These studies examined the morphological, physiological and molecular characteristics of microbes that had previously been cultured from various rock varnishes and identified the cultivars using 16S rDNA sequencing techniques. However, it is well known that most of organisms existing in nature are refractory to cultivation [17-20], so many important organisms would have been missed.

The currently described work investigates the genetics of rock varnish microbial community from a site in the Whipple Mtns., south of Death Valley, CA, near Parker, Arizona (Figure 1). We employed both cultural and molecular techniques to characterize the microorganisms found within the varnish and surrounding soil with the objectives of (a) identifying microorganisms potentially involved in varnish formation, and (b) discovering microorganisms that simply use the varnish as an extreme habitat.

Varnish collection: Since we are investigating the biocomplexity of the microbial communities of rock

varnishes, it was critical that the samples be collected aseptically as possible. The samples were approached from the downwind direction, photographed *in situ*, picked up at arm's length using sterile gloves, placed within sterile Whirl-paksTM and sealed. Loose dirt on the undersides of the varnished rocks has proven to be a contamination problem during storage and harvesting of the varnish in the laboratory. The samples were then wrapped in protective material to prevent damage. In future collections, glass containers will be used to prevent the deposition of polymers from the Whirl-paksTM on the surface of the varnish, thus contaminating the surface for microanalytical work [21].

The varnish was harvested from the host rock in a laminar flow bench. A Dremel tool with a coarse bit that had been flame sterilized was used to grind the varnish off the host rock and into a sterile container [22]. For use as controls we also collected soil samples adjacent to some of the varnished clasts.



Figure 1. Macro photograph of a varnished clast used in our study. The underlying grid has 10 divisions per inch.

Microbial Enumerations: Powdered rock varnish (0.1 gram) was added to 1 milliliter of sterile double-distilled H₂O. The samples were then stained with a stock DAPI (or Acridine Orange) (50mg/mL) solution. Samples were filtered onto 25mm Millipore Isopore 22 μ m pore size black polycarbonate filters with Whatman 25mm GF/F filters used for support. Fluorescing cells were counted on a Zeiss Research epifluorescence microscope equipped with an Osram

Xenon short arc photo optic lamp XBO 75W, and Chroma #31000 filter set for DAPI/Hoechst/AMCA.

The mean field (n) counted per sample was 57.16. The field standard deviation per sample was 7.48. The rock varnish had an average DAPI direct count of 9.0×10^7 cells gram^{-1} (standard deviation = 1.2×10^7). There was no determinable difference between DAPI and Acridine Orange direct counts.

Cultivable UV-resistant microorganisms: Five distinct colony types were purified from TSA plates after exposure to the UV irradiation treatment. These strains were examined microscopically using both a standard light and a transmission electron microscope (TEM). The 16S rDNA gene of each isolated was amplified by PCR, cloned and sequenced for comparison to the RDP phylogenetic database.

We examined each cultivated strain for its resistance to UV(C) irradiation. The strains were quite resistant, and still showed growth on TSA plates after exposure for five minutes at UV(C) intensities that readily killed *E. coli*. Affiliations were estimated for three of the strains to genus level only using a similarity level of >98%.

Strain RV1 (white colony). Multiple *Arthrobacter* strains were found in a white colony (*A. polychromogenes*, *A. ramosus*, *A. oxidans*, *A. globiformis*, and unspiciated *A. spp.* show 99% sequence similarity with this isolate). Eppard, et al. (1996) reported the culturing of three strains highly related to *Arthrobacter agilis* from rock varnish in the Mojave desert, but did not report UV resistance. [13].

Strain RV2 (orange colony). Various strains of *Curtobacterium flaccumfaciens* (e.g., AY273208.1) and an unidentified glacial ice bacterium (AF479342.1) show 98% sequence similarity to this isolate. Thus, this strain could be a candidate for survival in conditions such as those found in the polar regions of Mars.

Strain RV4 (black colony). This strain shows 16S rDNA sequence similarities of 98% (forward primers) and 99% (reverse primers) to a *Geodermatophilus obscura* originally isolated from soil samples from the Amargosa Desert of Nevada by Luedemann (1968) [20] and found in Negev desert soil and monuments by Eppard, et al., (1996) [13]. The strain's morphological and growth characteristics fit the description of *Geodermatophilus obscura* cluster I as described by Eppard, et al. (1996).

The uncultivable microbial community: We generated three rDNA libraries from the Death Valley rock varnish community DNA and two control libraries from soil adjacent to the varnished rock and lacking varnish. Varnish 16S rDNA libraries were prepared for Eubacteria and Archaea, and an 18S rDNA library

for Eukarya. The control soil libraries were prepared for Eubacteria and Archaea. An 18S rDNA control library for Eukarya was not obtained for the soil despite six attempts. Between 100-200 clones were prepared for each library.

The clones within each library have been arranged into related subgroups through examination of their RFLP patterns, and 16S rDNA PCR products of representative members of each subgroup were sequenced.

Acknowledgements: This work was sponsored by the Jet Propulsion Laboratory (JPL) Director's Research and Development Fund and carried out at JPL, California Institute of Technology, under a contract with the National Aeronautics and Space Administration.

References: [1] Potter, R.M. and G.R. Rossman (1977) *Science*, 196(4297), 1446-1448. [2] Potter, R.M. and G.R. Rossman (1979) *Chemical Geology*, **25**, 79-94. [3] Perry, R.S. and J.B. Adams (1978) *Nature*, **276**(5687) 489-491. [4] Broecker, W.S. and T.Z. Liu (2001) *Geology Today*, **11**(8) 4-10. [5] Dorn, R.I. (1998) *Rock Coatings. Developments in Earth Surface Processes*. Vol. 6, Amsterdam: Elsevier. [6] Guinness, E.A., R.E. Arvidson, et al. (1997) *Journal of Geophysical Research-Planets*, **102**(E12) 28687-28703. [7] Israel, E.J., R.E. Arvidson, et al. (1997) *Journal of Geophysical Research-Planets*, **102**(E12) 28705-28716. [8] Dorn, R.I. and T.M. Oberlander (1981) *Science*, **213**(4513) 1245-1247. [9] Krumbein, W.E. and K. Jens (1981) *Oecologia*, **50**(1) 25-38. [10] Staley, J.T., M.J. Jackson, et al. (1983) *Bmr Journal of Australian Geology & Geophysics*, **8**(1) 83-87. [11] Taylor-george, S., F. Palmer, et al. (1983) *Microbial Ecology*, **9**(3) 227-245. [12] Palmer, F.E., J.T. Staley, et al. (1986) *Geomicrobiology Journal*, **4**(4) 343-360. [13] Hungate, B., A. Danin, et al. (1987) *Canadian Journal of Microbiology*, **33**(10) 939-943. [14] Grote, G. and W.E. Krumbein (1992) *Geomicrobiology Journal*, **10**(1) 49-57. [15] Eppard, M., W.E. Krumbein, et al. (1996) *Archives of Microbiology*, **166**(1) 12-22. [16] Perry, R.S., J. Dodsworth, et al. (2003) *NASA Astrobiology Institute Annual Meeting*, NASA Ames Research Center, Moffet Field, CA. [17] Amann, R.I., W. Ludwig, and K.H. Schleifer (1995) *Microbiological Reviews*, **59**(1) 143-169. [18] Barns, S.M., R.E. Fundyga, et al. (1994) *Proceedings of the National Academy of Sciences of the United States of America*, **91**(5) 1609-1613. [19] Ward, D.M., R. Weller, and M.M. Bateson (1990) *Nature*, **345**(6270) 63-65. [20] Torsvik, V., J. Goksoyr, and F.L. Daae (1990) *Applied and Environmental Microbiology*, **56**(3) 782-787. [21] Perry, R.S., (2002) Personal communication. [22] Luedemann (1968) *Journal of Bacteriology*, **96**(5), 1848-1858.